VILNIUS GEDIMINAS TECHNICAL UNIVERSITY,
STATE RESEARCH INSTITUTE CENTER
FOR PHYSICAL SCIENCES AND TECHNOLOGY

Justas DILYS

RESEARCH INTO VARIABILITY OF PERMANENT MAGNET SYNCHRONOUS MOTOR PARAMETERS BY MAGNETIC FIELD MODELLING

DOCTORAL DISSERTATION

TECHNOLOGICAL SCIENCES,
ELECTRICAL AND ELECTRONIC ENGINEERING (T 001)

Vilnius, 2023

The doctoral dissertation was prepared at State Research Institute Center for Physical Sciences and in Technology 2017–2023.

Supervisors:

Prof. Dr Algirdas BAŠKYS (State Research Institute Center for Physical Sciences and Technology, Electrical and Electronic Engineering – T 001) 2017–2018,

Prof. Dr Voitech STANKEVIČ (State Research Institute Center for Physical Sciences and Technology, Electrical and Electronic Engineering – T 001) 2018–2023.

Consultant

Dr Habil. Marcin MORAWIEC (Gdansk University of Technology, Poland, Electrical and Electronic Engineering – T 001).

The Dissertation Defence Council of the Scientific Field of Electrical and Electronic Engineering of Vilnius Gediminas Technical University and State Research Institute Center for Physical Sciences and Technology:

Chairman

Prof. Dr Dalius NAVAKAUSKAS (Vilnius Gediminas Technical University, Electrical and Electronic Engineering – T 001).

Members:

Assoc. Prof. Dr Jonas GRADAUSKAS (State Research Institute Center for Physical Sciences and Technology, Physics – N 002),

Assoc. Prof. Dr Saulius GUDŽIUS (Kaunas University of Technology, Electrical and Electronic Engineering – T 001),

Prof. Dr Habil. Jaroslaw Andrzej GUZINSKI (Gdansk University of Technology, Poland, Electrical and Electronic Engineering – T 001),

Prof. Dr Jurij NOVICKIJ (Vilnius Gediminas Technical University, Electrical and Electronic Engineering – T 001).

The dissertation will be defended at the public meeting of the Dissertation Defence Council of the Scientific Field of Electrical and Electronic Engineering in the Senate Hall of Vilnius Gediminas Technical University at **2 p. m. on 15 June 2023**.
Address: Saulėtekio al. 11, LT-10223 Vilnius, Lithuania.
Tel. +370 5 274 4956; fax +370 5 270 0112; e-mail: doktor@vilniustech.lt

A notification on the intended defence of the dissertation was sent on 12 May 2023.

A copy of the doctoral dissertation is available or review at the Vilnius Gediminas Technical University repository http://dspace.vgtu.lt, the Library of Vilnius Gediminas Technical University (Saulėtekio al. 14, LT-10223 Vilnius, Lithuania and the Wroblewski Library of the Lithuanian Academy of Sciences (Žygimantų g. 1, LT-01102 Vilnius, Lithuania).

Vilnius Gediminas Technical University scientific book No. 2023-023-M
doi: 10.20334/2023-023-M

justas.dilys@ftmc.lt

VILNIAUS GEDIMINO TECHNIKOS UNIVERSITETAS,
VALSTYBINIS MOKSLINIŲ TYRIMŲ INSTITUTAS
FIZINIŲ IR TECHNOLOGIJOS MOKSLŲ CENTRAS

Justas DILYS

SINCHRONINIO VARIKLIO SU NUOLATINIAIS MAGNETAIS PARAMETRŲ KITIMO TYRIMAS MODELIUOJANT MAGNETINĮ LAUKĄ

DAKTARO DISERTACIJA

TECHNOLOGIJOS MOKSLAI,
ELEKTROS IR ELEKTRONIKOS INŽINERIJA (T 001)

Vilnius, 2023

Disertacija rengta 2017–2023 metais Valstybinio mokslinių tyrimų instituto Fizinių ir technologijos mokslų centre.

Vadovai:

prof. dr. Algirdas BAŠKYS (Valstybinis mokslinių tyrimų institutas Fizinių ir technologijos mokslų centras, elektros ir elektronikos inžinerija – T 001), 2017–2018,

prof. dr. Voitech STANKEVIČ (Valstybinis mokslinių tyrimų institutas Fizinių ir technologijos mokslų centras, elektros ir elektronikos inžinerija – T 001) 2018–2022.

Konsultantas

habil. dr. Marcin MORAWIEC (Gdansko technikos universitetas, Lenkija, elektros ir elektronikos inžinerija – T 001).

Vilniaus Gedimino technikos universiteto ir Valstybinio mokslinių tyrimų instituto Fizinių ir technologijos mokslų centro elektros ir elektronikos inžinerijos mokslo krypties disertacijos gynimo taryba:

Pirmininkas

prof. dr. Dalius NAVAKAUSKAS (Vilniaus Gedimino technikos universitetas, elektros ir elektronikos inžinerija – T 001).

Nariai:

doc. dr. Jonas GRADAUSKAS (Valstybinis mokslinių tyrimų institutas Fizinių ir technologijos mokslų centras, fizika – N 002),

doc. dr. Saulius GUDŽIUS (Kauno technologijos universitetas, elektros ir elektronikos inžinerija – T 001),

prof. habil. dr. Jaroslaw Andrzej GUZINSKI (Gdansko technikos universitetas, Lenkija, elektros ir elektronikos inžinerija – T 001),

prof. dr. Jurij NOVICKIJ (Vilniaus Gedimino technikos universitetas, elektros ir elektronikos inžinerija – T 001).

Disertacija bus ginama viešame Elektros ir elektronikos inžinerijos mokslo krypties disertacijos gynimo tarybos posėdyje **2023 m. birželio 15 d. 14 val.** Vilniaus Gedimino technikos universiteto senato posėdžių salėje.

Adresas: Saulėtekio al. 11, LT-10223 Vilnius, Lietuva.
Tel. +370 5 274 4956; fax +370 5 270 0112; el. paštas: doktor@vilniustech.lt

Pranešimai apie numatomą ginti disertaciją išsiųsti 2023 m. gegužės 12 d.
Disertaciją galima peržiūrėti Vilniaus Gedimino technikos universiteto talpykloje http://dspace.vgtu.lt, Vilniaus Gedimino technikos universiteto bibliotekoje (Saulėtekio al. 14, LT-10223 Vilnius, Lietuva) bei Lietuvos mokslų akademijos Vrublevskių bibliotekoje (Žygimantų g. 1, LT-01102 Vilnius, Lietuva).

Abstract

The dissertation deals with permanent magnet synchronous motors (PMSM) classical control theory and also by applying magnetic field theory approach. The purpose of the thesis is to create the mathematical model of the PMSM based on analytical equations of magnetic field accounting torque ripple, inductance distributions and back electromotive force, to develop the measurement systems for direct measurement of magnetic flux density and to propose PMSM parameter estimation method. In order to solve the stated problem and reach the goal following main tasks of the thesis are formulated: create PMSM model based on the analytical equations of magnetic flux density; develop vector control method of PMSM and investigate it experimentally; develop PMSM parameter estimation method; develop and implement a magnetic flux density measurement system; perform experimental measurement of magnetic flux density of PMSM using the developed system.

The dissertation consists of the introduction, three chapters, general conclusions, references, and the list of scientific publications of the author on the topic of the dissertation. The introduction discusses the research problem, the relevance of the dissertation, the object of the research, formulates the aim and tasks, describes the research methodology, the scientific novelty of the dissertation, defended statements and the practical value of the research findings. At the end of the introduction, the dissertation and the structure of the dissertation are provided. The first chapter reviews the PMSM design, rotor and stator types, magnetic field analytical solutions for predicting magnetic flux in the PMSM and magnetic field measurement systems. The second chapter presents an analysis of the following topics of PMSM's magnetic field distribution: the field created only by the rotor (open-circuit) and the field created only by the stator (armature reaction). Next, the effect of the stator slot on the magnetic field distribution is analysed. Finally, the enhanced PMSM model concept is stated based on magnetic field analysis. The third chapter presents the magnetic flux density measurement systems and compares the experimental results with the simulation results obtained using the proposed enhanced PMSM model.

The main results of the dissertation were published in seven scientific publications: four in the *Clarivate Analytics Web of Science* database with an impact factor and three in other databases. The results were presented at eight scientific conferences.

Reziumė

Disertacijoje nagrinėjamas sinchroninio variklio su nuolatiniais magnetais klasikinė valdymo teorija papildyta magnetinio lauko sprendiniais. Disertacijos tikslas – sukurti sinchroninio variklio su nuolatiniais magnetais analitinį matematinį modelį, gebantį įvertinti jo parametrų nepastovumą panaudojant analitinius magnetinius lauko sprendinius. Siekiant išspręsti iškeltą problemą ir pasiekti tikslą suformuluoti pagrindiniai disertacijos uždaviniai: sukurti sinchroninio variklio su nuolatiniais magnetais matematinį modelį, pagrįstą analitinėmis magnetinio lauko lygtimis; suprojektuoti magnetinio srauto tankio matavimo sistemą, naudojant B-skaliarinį jutiklį; sukurti sinchroninio variklio su nuolatiniais magnetais realių parametrų nustatymo metodus; suprojektuoti eksperimentinį stendą; ištirti magnetinio srauto tankio pereinamuosius procesus panaudojant sukurtą magnetinio lauko matavimo sistemą.

Disertaciją sudaro įvadas, trys skyriai, bendrosios išvados, literatūros sąrašas ir disertacijos autoriaus mokslinių publikacijų sąrašas disertacijos tema. Įvade apibrėžiama tyrimo problema, disertacijos aktualumas, tyrimo objektas, formuluojamas darbo tikslas ir užduotys, aprašoma tyrimo metodika, disertacijos mokslinis naujumas, nurodomi ginamieji teiginiai ir praktinė tyrimų išvadų vertė. Įžangos pabaigoje pateikiamos autoriaus publikacijos disertacijos tema ir apibūdinama disertacijos struktūra. Pirmajame skyriuje apžvelgiama sinchroninių variklių su nuolatiniais magnetais konstrukcija ir klasifikavimas, taip pat apžvelgiamas magnetinio lauko analitinis modelis ir magnetinio lauko matavimo sistemos. Antrajame skyriuje pateikiami analitiniai magnetinio lauko sprendiniai, kurie yra naudojami magnetinio srauto tankio skirto sinchroninio variklio su nuolatiniais magnetais oro tarpe ir apvijose skaičiavimui, taip pat pateikiamas sinchroninio variklio su nuolatiniais magnetais patobulintas modelis bei jo analizė. Trečiajame skyriuje pateikiami magnetinio srauto tankio matavimo rezultatai sinchroninio variklio su nuolatiniais magnetais oro tarpe ir gauti rezultatai palyginami su modeliavimo rezultatais.

Pagrindiniai disertacijos rezultatai paskelbti 7 mokslinėse publikacijose: 4 iš jų buvo išspausdintos recenzuojamuose mokslo žurnaluose, įtrauktuose į *Clarivate Analytics Web of Science* sąrašą ir turinčiuose citavimo rodiklį, 3 kitose duomenų bazėse. Rezultatai buvo pristatyti 8 mokslinėse konferencijose.

Notations

Symbols

A	– magnetic vector potential;
b_0	– slot opening;
B	– magnetic flux density;
B_r	– radial magnetic flux density component;
B_R	– permanent magnet remanence;
B_θ	– tangential magnetic flux density component;
f_e	– electrical frequency;
f_m	– mechanical frequency;
f_s	– switching frequency;
F_s	– magnetomotive force;
$e_\mathrm{a}, e_\mathrm{b}, e_\mathrm{c}$	– back EMFs in stator phases;
g	– effective air gap length;
$G(s)$	– transfer function;
h_w	– winding thickness;
H	– magnetic field intensity;
$i_\mathrm{a}, i_\mathrm{b}, i_\mathrm{c}$	– three-phase winding currents;
i_α, i_β	– currents in α- and β-axis frame;
$i_\mathrm{d}, i_\mathrm{q}$	– currents in d- and q-axis frame;
j	– complex number;
J	– moment of inertia;
$\mathbf{K}$	– Kalman gain matrix;
k_p	– a proportional gain of the PI controller;
k_i	– an integral gain of the PI controller;

L	– axial length;
$L_{\text{aa}}, L_{\text{bb}}, L_{\text{bb}}$	– phase winding self-inductances;
L_{α}, L_{β}	– inductances in α- and β-axis frame;
$L_{\text{d}}, L_{\text{q}}$	– inductances in d- and q-axis frame;
L_{sl}	– the leakage inductance;
$L_{\text{ab}}, L_{\text{ac}}, L_{\text{bc}}$	– the mutual inductance between two-phases;
L_{s0}	– the magnetising inductance;
L_{s2}	– inductance fluctuation;
N_{s}	– winding turns;
N_{h}	– number of harmonics;
p	– number of pole pairs;
$\mathbf{P}, \mathbf{Q}, \mathbf{R}$	– covariance matrices;
P_{m}	– motor mechanical power;
Q_{s}	– slot number;
R_{m}	– magnet radius;
R_{r}	– rotor radius;
R_s	– stator phase winding resistance;
R_{s}	– stator bore radius;
s	– Laplace operator
$S_{\text{a}}, S_{\text{b}}, S_{\text{c}}$	– inverter switching functions corresponding to phases a, b, and c;
t	– time;
t_{s}	– settling time;
T_{e}	– electromagnetic torque;
T_{f}	– friction torque;
T_{L}	– load torque;
T_{s}	– sampling time;
$\mathbf{u}$	– input vector;
$v_{\text{a}}, v_{\text{b}}, v_{\text{c}}$	– phase winding voltages;
v_{α}, v_{β}	– voltages in d- and q-axis frame;
$v_{\text{d}}, v_{\text{q}}$	– voltages in α- and β-axis frame;
V_{dc}	– inverter DC link voltage;
$\mathbf{v}_{\text{s}}$	– the magnitude of stator voltage space vector;
ζ	– damping factor;
η	– viscous friction coefficient;
θ	– electrical rotor position;
θ_{c}	– coil pitch angle;
θ_{m}	– mechanical rotor position;
$\lambda_{\text{a}}, \lambda_{\text{b}}, \lambda_{\text{c}}$	– phase winding flux linkages corresponding to phases a, b, and c;
λ_{c}	– span angle of the coil;
λ_{PM}	– flux linkage of the rotor magnet;
μ_{r}	– relative recoil permeability;
μ_0	– relative air permeability;
φ	– magnetic scalar potential;
ω_{e}	– electrical rotor speed;
ω_{m}	– mechanical rotor speed;
ω_{n}	– natural frequency.

Abbreviations

AC	– Alternating Current;
ADC	– Analogue to Digital Converter;
AES	– Advanced Encryption Standard;
AR	– Armature Reaction;
ARM	– Advanced RISC Machines;
CMR	– Colossal Magnetoresistance;
DC	– Direct Current;
EKF	– Extended Kalman Filter;
EMF	– Electromotive Force;
EEPROM	– Electrically Erasable Programmable Read Only Memory;
FBG	– Fibre Bragg Grating ;
FLASH	– Electronic Non-Volatile Computer Memory Storage Medium ;
FOC	– Field-Oriented Control;
I2C	– Inter-Integrated Circuit;
IPM	– Interior Permanent Magnet;
LCD	– Liquid-Crystal Display;
LP	– Low-Pass;
LPF	– Low-Pass Filter;
MOSFET	– Metal Oxide Semiconductor Field Effect Transistor;
MTPA	– Maximum Torque per Ampere;
MST	– Maxwell Stress Theory;
MMF	– Magnetomotive Force;
MR	– Magnetoresistance;
SD	– Secure Digital;
SNR	– Signal-to-noise Ratio;
PC	– Personal Computer;
PD	– Phase Detector ;
PI	– Proportional-Integral;
PM	– Permanent Magnet;
PMSM	– Permanent Magnet Synchronous Motor;
PWM	– Pulse Width Modulation;
PLL	– Phase Locked Loop;
RF	– Rotor Frame;
SVPWM	– Space Vector Pulse Width Modulation;
USART	– Universal Synchronous Asynchronous Receiver Transmitter;
USB	– Universal Serial Bus;
UKF	– Unscented Kalman Filter;
UT	– Unscented Transformation;
VCO	– Voltage Controlled Oscillator.

Contents

Introduction

Problem Formulation

Most studies of the existing permanent magnet synchronous motor (PMSM) models make ideal simplifications of the physical PMSM. Consequently, most PMSM models have low accuracies and cannot truly reflect the non-linear PMSM characteristics (Ge et al., 2022). These models did not account for torque ripple, inductance distributions, and back electromotive force waveforms. Generally, motor parameters like stator resistance and dq-axis armature inductances are considered constants in these PMSM models (Song et al., 2009). In practice, these parameters vary due to a variable operating point and electromagnetic factors. The accounting of the variability of PMSM parameters in the motor model is important because only such a model allows for an adequate evaluation of the stability, efficiency and dynamic response of the PMSM control system. Only a few studies have tried to establish an improved model of the account torque ripple, inductance distributions, and back electromotive force waveforms (Jabbar et al., 2003; Kim et al., 2018; Parasiliti et al., 2006). However, these models are based on using the finite element method to analyse a PMSM dynamic therefore, the simulation time using such models is unacceptably long (Djelloul-Khedda et al., 2017; Piña Ortega et al., 2016).

The main problem that the dissertation solves – is an ideal mathematical model of a PMSM. It does not consider such important motor phenomena as torque ripple, inductance and back electromotive force distributions.

The hypothesis states that the enhanced mathematical model of the PMSM created using analytical equations of magnetic flux density allows for improving the PMSM model's accuracy compared to the ideal PMSM model.

Relevance of the Dissertation

A PMSM has become extremely popular and the most obvious choice in many applications due to its inherent advantages like higher efficiency, higher torque to weight ratio, smaller size, etc. (Paitandi & Sengupta, 2020). PMSMs have been widely used in various applications, e.g., industry, public life, aerospace, domestic appliances, information and office equipment, electric vehicles and servo drives.

Creating mathematical models of synchronous motors with permanent magnet control systems plays an important role in the development of such systems. Therefore, developing new and more accurate mathematical models for synchronous motors with permanent magnets is relevant, as it allows for more reliable modelling results to be obtained.

An accurate PMSM model enables a simulation of the PMSM control system without a physical PMSM. Basically, a simulation speeds up the control method's development and is a more cost-effective development. Therefore, prior to designing a PMSM drive, a simulation study is always required to select the appropriate control algorithm for a given application.

The Object of the Research

The object of the research is a permanent magnet synchronous motor.

The Aim of the Dissertation

The dissertation aims to create the mathematical model of the PMSM based on analytical equations of magnetic field accounting torque ripple, inductance distributions and back electromotive force, to develop the measurement systems for direct measurement of magnetic flux density and to propose a PMSM parameter estimation method.

The Tasks of the Dissertation

To solve the stated problem and reach the dissertation's aim the, the following tasks were formulated:

1. To create a PMSM model based on the analytical equations of magnetic flux density.
2. To develop a vector control method of a PMSM and investigate it experimentally.
3. To develop a PMSM parameter estimation method.
4. To develop and implement a magnetic flux density measurement systems for measuring the magnetic flux density in the PMSM.
5. To perform experimental research of magnetic flux density measurement for a PMSM using the created systems.

Research Methodology

A theoretical analysis study has been performed to improve strategies aimed at finding a solution to the problem. A computer simulation was carried out using the Matlab software package. For the development and experimental investigation, three embedded systems devices are developed, including hardware, firmware and software. The first two devices for magnetic flux density measurement used the ARM microcontroller LPC54619. And the third device for the PMSM control used the ARM microcontroller LPC1549. For all devices, personal computer assistant software was created.

The Scientific Novelty of the Dissertation

1. A new enhanced PMSM model based on analytical magnetic flux density considers torque ripple, inductance distribution, and back electromotive force and allows to reduce the simulation time compared to models of the same purpose.

2. A modified extended Kalman filter is proposed to reduce the execution time, which can be used to estimate the rotor speed and position of the PMSM.

3. A new method for estimating stator resistance and inductance of PMSMs is proposed in standstill operation based on the application of three transient voltage pulses.

4. The developed new magnetic field measurement systems allows direct measuring of the magnetic flux density in the air gap of the motor and evaluates the accuracy of the enhanced PMSM model.

The Practical Value of the Research Findings

The proposed enhanced model of a PMSM accounting for the variability of motor parameters due to magnetic flux variation provides a more accurate simulation of the motor. Moreover, created magnetic field measurement systems can be used not only to measure magnetic field dynamics in motors but also in other fields of industry and science because they can measure the magnetic field independently of its direction in a wide range of magnetic fields and pulse duration.

The research results presented in this dissertation were also used for the implementation of a scientific project, i.e. “Fast magnetoresistive processes in nanostructured manganite film sensors used for monitoring of electromagnetic forming.”, Grant S-MIP-17-110 (2017 – 2020) of the Research Council of Lithuania.

Defended Statements

Defended statements of this doctoral dissertation are as follows:

1. The proposed enhanced PMSM model based on the analytical equations of magnetic flux density allows for relating such effects as cogging torque, back-EMF shape, flux linkage shape and dq-axis inductance parameters to geometrical parameters of the PMSM.
2. The modified extended Kalman filter for rotor speed and position estimation, based on the separation of the gain and covariance matrix calculation from prediction and update steps, provides the same accuracy with three times less execution time of the processor as compared to the classical extended Kalman filter.
3. The stator resistance and dq-axis inductance for PMSM at standstill operation can be estimated by applying three short-time (20 μs) voltage pulses and measuring phase current values.
4. The designed magnetic flux density measurement systems based on a CMR sensor can be used to measure magnetic flux density in the PMSM's air gap region independently in the direction of the magnetic field.

Approval of the Research Findings

The main dissertation results were published in seven scientific publications: four in the *Clarivate Analytics Web of Science* database with an impact factor and three in other databases. The results were presented at eight scientific conferences.

The research results on the dissertation's topic were presented at eight scientific conferences:

- International Conference on Automation and Control Engineering, 15 – 16 February 2022, London, United Kingdom.
- The 65th International Conference for Students of Physics and Natural sciences "Open Readings", 2022, Vilnius, Lithuania.
- 11th Conference of Doctoral Students and Young Researchers, "FizTech2021", 2021, Vilnius, Lithuania.
- 9th Conference of Doctoral Students and Young Researchers, "FizTech2019", 2019, Vilnius, Lithuania.
- International Conference "Open Conference of Electrical, Electronic and Information Science (eStream)", 2020, Vilnius, Lithuania.
- International Conference "Open Conference of Electrical, Electronic and Information Science (eStream)", 2017, Vilnius, Lithuania.
- 20th Conference for Lithuanian Junior Researchers "Science – the Future of Lithuania", 2017, Vilnius, Lithuania.
- 22th Conference for Lithuanian Junior Researchers "Science – the Future of Lithuania", 2019, Vilnius, Lithuania.

Structure of the Dissertation

The dissertation consists of an introduction, three chapters and general conclusions. The volume of the dissertation is 137 pages, with: 87 figures, 108 equations and 14 tables. Additionally, 140 references of reference are used in the dissertation.

Acknowledgements

I express the deepest gratitude to Prof. Dr Voitech Stankevič and Prof. Dr Algirdas Baškys for outstanding guidance, caring, patience, enthusiasm, and an excellent research atmosphere. Special thanks go to Dr Habil. Marcin Morawiec for supporting me in terminology and shared knowledge, and Prof. Dr Habil. Jarosław Guziński and his team for inviting me to the Gdansk University of Technology.

I also thank Prof. Dr Jurij Novickij and Prof. Dr Dalius Navakaukas for their review and numerous comments and suggestions, which have been extremely helpful in improving the quality of this work.

1

Review of Permanent Magnet Synchronous Motor Principle of Operation

A PMSM has become extremely popular and the most obvious choice in many applications due to its inherent advantages like higher efficiency, higher torque to weight ratio, smaller size, etc. (Paitandi & Sengupta, 2020). PMSMs with rare earth permanent magnets can correspond to the highest efficiency classes. PMSMs can meet or exceed the IE4 efficiency level (Klontz, 2017; Ustun et al., 2017). PMSMs have better overall performance in terms of power overload curves and efficiency at any load and any speed, provided that it is a highsaliency machine, maximized by proper design (Klontz, 2017).

In modern industry, the requirement for PMSM performance is increasing. The improvement can be achieved by optimising the motor design and the control of power electronic devices. Thus, in the chapter, a systematic literature review on PMSM models and control is presented. This chapter begins with reviews of PMSM construction, rotor and stator classification. A review of an ideal mathematical PMSM model is presented. Next, different speed and position estimators, including standstill operation for a PMSM, are discussed, followed by a two-dimensional magnetic field analytical model including the stator's and rotor's magnetic field distribution theory. Finally, a review presents techniques and sensors for magnetic flux measurement in electrical machines.

The research results are published in the author's publications (Dilys, 2017; Dilys, 2020; Dilys et al., 2021;). The results were announced at international scientific conferences, i.e., ICACE (London, 2022), Open Readings (Vilnius 2022), "eStream" (Vilnius 2017, 2022) and national conferences "Science – the Future of Lithuania" (Vilnius, 2017, 2019), "FizTech" (Vilnius 2019, 2021).

1.1. Permanent Magnet Materials

In electric machines, permanent magnet (PM) materials provide magnetic flux, a fundamental function. A suitable coercivity and the highest possible saturation magnetisation are required for this function. The value of the demagnetising field intensity that is required to bring the magnetic flux density to zero in a material that was previously magnetised is referred to as the coercive field strength, or coercivity H_c. The ability to resist demagnetisation, such as field demagnetisation from an electric or magnetic circuit and thermal demagnetisation from operating temperature, is known as coercivity for the permanent magnets. Coercivity is very important for motor applications because these two actions of demagnetisation happen all the time when motors are running (Gutfleisch et al., 2010). The second quadrant is where the B-H hysteresis loop is most important for permanent magnet materials. The generic B-H demagnetisation characteristics of these materials are shown in Fig. 1.1. A useful metric for evaluating the ability of permanent magnet material is known as the product of maximum energy $B \cdot H$. This corresponds to the largest magnitude of the B vs H product $(B \cdot H)_{\max}$ found in the second quadrant of that material's hysteresis loop, see Fig. 1.1.

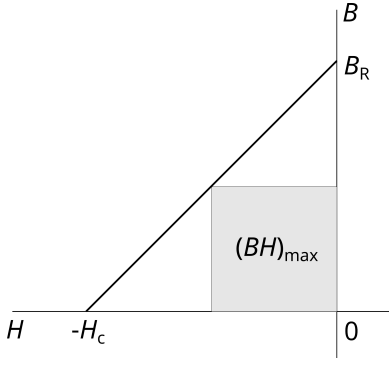

Fig. 1.1. Demagnetisation curve of a typical PM material

Four types of permanent magnet materials are used for PMSMs: neodymium iron boron (NdFeB), SmCo, hard ferrite, and alnico (see Table 1.1). SmCo magnets are alloys of cobalt and samarium produced by the powder metallurgy process. They are magnetised before pressing. The material has a linear demagnetisation characteristic with high remanence and coercivity, and therefore a high maximum energy product. The material is electrically conducting and magnetically anisotropic, and is magnetised along the thickness of pieces. SmCo magnets are mechanically hard and brittle; therefore, they must be handled with care. The material has a high Curie temperature of 700 – 800 °C, depending the grades, with a metallurgical change at 300 – 350 °C. The main deficiency of the material is the very high price, which restricts its use to a marginal market.

The magnetic properties of NdFeB magnets, which are now being produced in greater quantities than those of SmCo magnets, are superior to those of SmCo magnets, but, unfortunately, only at room temperature. Mechanically, NdFeB magnets are very strong and

Table 1.1. Properties of various PM manufacturers' commercially available materials for temperatures in the range of 20 °C to 30 °C (Eklund & Eriksson, 2019)

Material Family	B_R, T	H_c, kA/m	$(BH)_{max}$, kJ/m^3	μ_r
Alnico	0.55 – 1.37	38 – 151	10.7 – 83.6	1.3 – 6.2
Hard ferrite	0.20 – 0.46	140 – 405	6.4 – 41.8	1.05 – 1.2
NdFeB	1.08 – 1.49	876 – 2710	220 – 430	1.0 – 1.1
SmCo	0.87 – 1.19	1350 – 2400	143 – 251	1.0 – 1.1

not as brittle as SmCo magnets. The coercive force and demagnetisation curves, in particular, are strongly temperature dependent. The temperature coefficient of B_R is -0.09 to -0.15%/°C and the temperature coefficient of H_c is -0.40%/°C to -0.80%/°C. The maximum service temperature is 250 °C, and the Curie temperature is 350 °C). Corrosion is another danger to the NdFeB. NdFeB magnets have extraordinary potential for significantly working on the execution to cost proportion for some applications. As a result, they will have a significant impact on the future development and application of PM equipment (Gieras, 2009).

Ferrite magnets were created as sintered materials by the powder metallurgy process in the 1950s. They consist of compounds of ferric oxide and carbonate of barium or strontium. They feature a rather linear demagnetisation characteristic with low remanence and coercivity, resulting in a low maximum energy product. Therefore, they do not provide a compact motor design. Electrically, ferrite magnets are very good insulators and produce insignificant eddy current loss caused by external AC fields. The mechanical properties of the material are unique, being very hard and brittle. For this reason, they are known as ceramics. Due to their low prices and corrosion resistance, they are the most commonly used PM material in PMSMs.

Alnico, the last magnetic material mentioned here, is the oldest commercially available PM. The alloy consists of aluminium, nickel, cobalt, and iron plus other elements, and is available in both sintered and cast forms. The material has non-linear demagnetising characteristics with a very high remanence and a very low coercivity. As a result, alnico's energy product is low and can easily be demagnetised by external fields.

1.2. The Magnetisation of Permanent Magnets

A different PM magnetisation can produce different field distributions in the system as well as various motor performances. Initial investigation into the impact of achieve optimal motor performance, PM excitation to the PM synchronous motor's electromagnetic field system is necessary.

The majority of high-speed motors make extensive use of radial magnetisation, which is the most prevalent type of PM excitation. Parallel and sinusoidal magnetisation, on the other hand, are utilised for specific circumstances and applications.

In high-speed PMSMs, multipole radial magnetisation is frequently utilised. For this kind of magnetisation, non-linear isotropic magnetic materials like bonded NdFeB are frequently used. An isotropic sintered magnetic material with a stronger magnetic field than

isotropic materials are used for parallel magnetisation. The ideal Halbach magnetisation is used for sinusoidal magnetisation. PM magnetisation is one of the key factors to shape the back-EMF waveform, which is closely related to the production of electromagnetic torque and torque ripple for the motor (Phyu & Chao, 2012).

The radial magnetisation runs along the radius, whereas the parallel magnetisation runs parallel to the edges, as in the case of surface parallel magnets. The normal direction to the surface is denoted by the vector $\mathbf{n}$, and the magnetisation vector by $\mathbf{M}$. However, in situations involving alternative edge shapes, this need not necessarily be the case. The fact that the magnetisation direction is horizontal is crucial in that scenario.

1.3. Rotor Configuration

In recent years, PM brushless machines have replaced induction machines as the preferred means of propulsion for electric vehicles. The following are their primary advantages (Chau, 2015):

- For a given output power, the overall weight and volume can be significantly reduced, leading to higher power density. This is because high-energy PMs stimulate the magnetic field.
- They naturally offer higher efficiency due to the absence of rotor copper loss.
- Because most of the heat is produced in the stator, it can be dissipated more effectively into the surrounding environment, making cooling simpler.
- Higher reliability is inherent in the PM excitation because there is no risk of mechanical damage, overheating, or manufacturing defects.
- Because of the copper winding absence in the rotor, they possess a lower electromechanical time constant and, hence, a better dynamic response.

The PMSMs can be further divided into surface-mounted, surface-inset, interior radial, and interior circumferential topologies based on where the PMs are positioned in the rotor (Balčaitis, 2016) while the stator is the same as shown in Fig. 1.2. The surface-mounted magnet motor allows for radial magnetisation of the magnets (Fig. 1.2a) or parallel. Sometimes, a non-ferromagnetic external high-conductivity cylinder is used. It serves as a damper, provides an asynchronous starting torque, shields the PMs from the demagnetising effects of armature reaction and centrifugal forces, and protects them. Assuming interesting earth PMs are utilised, the simultaneous reactance in the d-axis and q-axis are essentially something similar.

In surface-inset type motors (Fig. 1.2b), PMs are embedded in shallow slots and radially magnetised. Additionally, the magnets are fully and mechanically embedded in the rotor, preventing them from flying out, making this arrangement significantly more mechanically robust than surface mount motors. In contrast, the magnets in surface mount motors protrude out of the rotor laminations. The rotor magnetic circuit can be overlaid or made of strong steel. In the first scenario, either an external non-ferromagnetic cylinder or a starting cage winding is required. The q-axis simultaneous reactance is more prominent

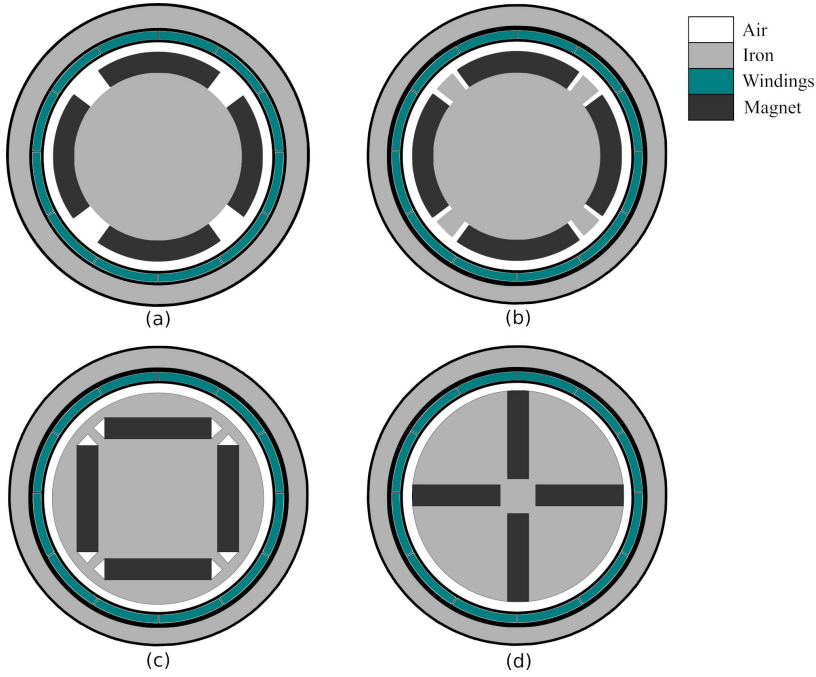

Fig. 1.2. PMs motor classification by the location of the PMSM rotor poles: (a) the surface-mounted magnet; (b) the surface-inset magnet; (c) the buried or interior magnet; and (d) the interior circumferential or spoke magnet

than that in the d-axis. As a rule, the back-EMF instigated by the PMs is lower than that in surface PMSM rotors.

Interior permanent magnet (IPM) synchronous motors (Fig. 1.2c) have unique elements for customizable speed activity, which recognize them from different classes of AC machines. They are robust machines with a high power density that can run at a high motor and inverter efficiency over a wide range of speeds, including significant ranges of constant power operation. The IPM design's low requirements for magnet weight reduce the cost of the motor. The rotor magnetic circuit saliency adds a reluctance torque term to the IPM motor's torque equation and preferentially increases the q-axis inductance. A way to achieve smooth, responsive torque control is to regulate the magnitude and phase angle of the sinusoidal phase currents in relation to the orientation of the rotor (Jahns et al., 1986). Circumferentially (parallel) magnetised PMs are embedded in deep slots on the spoke-type buried magnet rotor (Fig. 1.2d). Due to circumferential magnetisation the synchronous reactance of the q-axis is higher than that of the d-axis. Non-rare earth elements are used to construct the spoke-type permanent magnet synchronous motor, which has a low flux density. It has a flux-concentrated structure of permanent magnet arrangement to improve power density. Further, the torque in the spoke-type PMSM is composed of a magnetic torque component from the permanent magnets and a reluctance torque arising from the inductance difference between the d-axis and q-axis (Cho et al., 2017).

1.4. Mathematical Three-Phase Model

The three-phase stator voltage equations of permanent magnet synchronous motor can be expressed as (Pitrėnas, 2013)

$$\begin{bmatrix} v_{\mathrm{a}} \\ v_{\mathrm{b}} \\ v_{\mathrm{c}} \end{bmatrix} = \begin{bmatrix} R_{\mathrm{s}} & 0 & 0 \\ 0 & R_{\mathrm{s}} & 0 \\ 0 & 0 & R_{\mathrm{s}} \end{bmatrix} \begin{bmatrix} i_{\mathrm{a}} \\ i_{\mathrm{b}} \\ i_{\mathrm{c}} \end{bmatrix} + \begin{bmatrix} L_{\mathrm{aa}} & L_{\mathrm{ab}} & L_{\mathrm{ac}} \\ L_{\mathrm{ba}} & L_{\mathrm{bb}} & L_{\mathrm{bc}} \\ L_{\mathrm{ca}} & L_{\mathrm{cb}} & L_{\mathrm{cc}} \end{bmatrix} \begin{bmatrix} \frac{i_{\mathrm{a}}}{\mathrm{d}t} \\ \frac{i_{\mathrm{b}}}{\mathrm{d}t} \\ \frac{i_{\mathrm{c}}}{\mathrm{d}t} \end{bmatrix} + \begin{bmatrix} e_{\mathrm{a}} \\ e_{\mathrm{b}} \\ e_{\mathrm{c}} \end{bmatrix}, \quad (1.1)$$

where e_{a}, e_{b} and e_{c} are the back-EMF voltages, R_{s} is stator resistance (Pillay & Krishnan, 1988). The stator self-inductances are given

$$\begin{aligned} L_{\mathrm{aa}} &= L_{\mathrm{sl}} + L_{\mathrm{s0}} + L_{\mathrm{s2}} \cos(2\theta), \\ L_{\mathrm{bb}} &= L_{\mathrm{sl}} + L_{\mathrm{s0}} + L_{\mathrm{s2}} \cos(2\theta + 2\pi/3), \\ L_{\mathrm{cc}} &= L_{\mathrm{sl}} + L_{\mathrm{s0}} + L_{\mathrm{s2}} \cos(2\theta + 4\pi/3), \end{aligned} \quad (1.2)$$

and the stator mutual inductances are

$$\begin{aligned} L_{\mathrm{bc}} = L_{\mathrm{cb}} &= -\frac{L_{\mathrm{s0}}}{2} + L_{\mathrm{s2}} \cos(2\theta), \\ L_{\mathrm{ab}} = L_{\mathrm{ba}} &= -\frac{L_{\mathrm{s0}}}{2} + L_{\mathrm{s2}} \cos(2\theta - 2\pi/3), \\ L_{\mathrm{ac}} = L_{\mathrm{ca}} &= -\frac{L_{\mathrm{s0}}}{2} + L_{\mathrm{s2}} \cos(2\theta - 4\pi/3), \end{aligned} \quad (1.3)$$

where the stator self-inductances L_{bc}, L_{cb}, L_{ac}, L_{ca}, L_{ab}, L_{ba} are of three-phases (a, b and c) respectively; θ is the electrical angle of the rotor; L_{sl} is the leakage inductance of stator winding; L_{s0} is the magnetising inductance due to the air gap flux and L_{s2} is the amplitude of inductance fluctuation due to the rotor position (Bui et al., 2017; Vas, 1998).

1.4.1. Dynamic Model in Stationary Frame

The following system of differential equations represents a dynamic model of a surface-mounted permanent magnet synchronous motor and a sinusoidal flux distribution in a stationary reference frame (Dhaouadi et al., 1991)

$$\begin{aligned} \frac{\mathrm{d}i_{\alpha}}{\mathrm{d}t} &= -\frac{R_s}{L_{\mathrm{s}}} i_{\alpha} + \frac{\lambda_{\mathrm{PM}}}{L_{\mathrm{s}}} \omega_{\mathrm{e}} \sin\theta + \frac{v_{\alpha}}{L_{\mathrm{s}}}, \\ \frac{\mathrm{d}i_{\beta}}{\mathrm{d}t} &= -\frac{R_s}{L_{\mathrm{s}}} i_{\beta} - \frac{\lambda_{\mathrm{PM}}}{L_{\mathrm{s}}} \omega_{\mathrm{e}} \cos\theta + \frac{v_{\beta}}{L_{\mathrm{s}}}, \\ \frac{\mathrm{d}\omega_{\mathrm{e}}}{\mathrm{d}t} &= \frac{3}{2} p \frac{\lambda_{\mathrm{PM}}}{J} \left((i_{\beta} \cos\theta - i_{\alpha} \sin\theta) - \frac{\eta}{p} \omega_{\mathrm{e}} - T_{\mathrm{L}} \right), \\ \frac{\mathrm{d}\theta}{\mathrm{d}t} &= \omega_{\mathrm{e}}, \end{aligned} \quad (1.4)$$

where: i_α and v_α are the α-axis current and voltage; i_β and v_β are the β axis current and voltage; R_s is the stator resistance; $L_s = L_{sl} + \frac{3}{2}L_{s0}$ is the stator synchronous inductance; p is the number of the pole pairs; w_e and θ are the rotor electrical angular speed and position, respectively; J and η are the rotor inertia and viscous friction coefficients, respectively; T_L is load electrical torque. The voltages v_α, v_β and current i_α, i_β are obtained from the three-phase model by transformation

$$\begin{bmatrix} S_\alpha \\ S_\beta \end{bmatrix} = \frac{2}{3}\begin{bmatrix} 1 & -\frac{1}{2} & -\frac{1}{2} \\ 0 & \frac{\sqrt{3}}{2} & -\frac{\sqrt{3}}{2} \end{bmatrix}\begin{bmatrix} S_a \\ S_b \\ S_c \end{bmatrix}, \tag{1.5}$$

where S is phase voltage or current.

1.4.2. Dynamic Model in Rotating Reference Frame

All sinusoidally varying inductances in the abc frame are forced to remain constant in the dq frame as a result of the transformation of the synchronous machine equations from the abc frame variables to the dq frame variables (Pillay & Krishnan, 1988). The following describes the transition from a three-phase rotating dq frame to a three-phase stationary system abc frame (Bae et al., 2003)

$$\begin{bmatrix} S_d \\ S_q \end{bmatrix} = \frac{2}{3}\begin{bmatrix} \cos(\theta) & \cos\left(\theta - \frac{2\pi}{3}\right) & \cos\left(\theta + \frac{2\pi}{3}\right) \\ -\sin(\theta) & -\sin\left(\theta - \frac{2\pi}{3}\right) & -\sin\left(\theta + \frac{2\pi}{3}\right) \end{bmatrix}\begin{bmatrix} S_a \\ S_b \\ S_c \end{bmatrix}, \tag{1.6}$$

where S is the transformed variable. This transformation is often known as dq transformation. The flux-producing component of a motor current is aligned along the d-axis in the vector control for AC motors. The d-axis is regarded as the reference axis. The direction of the q variable, which is referred to as the q-axis, is defined as the 90 ° circumference in front of the d-axis (Kim, 2017).

An appropriate dynamic model of the system is utilised in the state space design. Therefore, a state space model of PMSMs in the rotor rotating reference frame is represented as (Vaez-Zadeh, 2018)

$$\begin{aligned} \frac{di_d}{dt} &= -\frac{R_s}{L_d}i_d + \omega_e\frac{L_q}{L_d}i_q + \frac{v_d}{L_d}, \\ \frac{di_q}{dt} &= -\frac{R_s}{L_q}i_q - \omega_e\frac{L_d}{L_q}i_d - \omega_e\frac{\lambda_{PM}}{L_q} + \frac{v_q}{L_q}, \\ \frac{d\omega_e}{dt} &= \frac{p}{J}(T_e - T_L - \frac{\eta}{p}\omega_e), \\ \frac{d\theta}{dt} &= \omega_e, \end{aligned} \tag{1.7}$$

where the voltages v_d, v_q and current i_d, i_q are obtained from the three-phase model by

Equation (1.6), d-axis inductance is $L_{\mathrm{d}} = L_{\mathrm{sl}} + \frac{3}{2}(L_{\mathrm{s0}} - L_{\mathrm{s2}})$ and q-axis inductance are $L_{\mathrm{q}} = L_{\mathrm{sl}} + \frac{3}{2}(L_{\mathrm{s0}} + L_{\mathrm{s2}})$, and the motor's electromagnetic torque is given by

$$T_{\mathrm{e}} = \frac{3}{2} p \left(\lambda_{\mathrm{PM}} i_{\mathrm{q}} + (L_{\mathrm{d}} - L_{\mathrm{q}}) i_{\mathrm{d}} i_{\mathrm{q}}\right). \tag{1.8}$$

1.5. Rotor Position Estimation Using Phase-Locked Loop

The phase-locked loop technique can be used for speed and position estimation (Burgos et al., 2006; Ilioudis, 2017; Jiang et al., 2019; Paitandi & Sengupta, 2017; Tao et al., 2017). In a stationary reference frame, the back-EMF voltage can be found as

$$\begin{aligned} e_{\alpha} &= v_{\alpha} - R_s i_{\alpha} - L_{\mathrm{s}} \frac{\mathrm{d}i_{\alpha}}{\mathrm{d}t}, \\ e_{\beta} &= v_{\beta} - R_s i_{\beta} - L_{\mathrm{s}} \frac{\mathrm{d}i_{\beta}}{\mathrm{d}t}, \end{aligned} \tag{1.9}$$

where inductance L_{s} is not constant in the stationary reference frame and depends on the position of the rotor if the air gap is not uniform. However, the surface-mounted PMSM synchronous inductance could be expressed as $L_{\mathrm{s}} = L_{\mathrm{d}} = L_{\mathrm{q}}$ and it is unrelated to the rotor position. If the saliency of a PMSM is low, the synchronous inductance L_{s} can still be expressed as

$$L_{\mathrm{s}} = \frac{L_{\mathrm{d}} + L_{\mathrm{q}}}{2}. \tag{1.10}$$

Back-EMF voltages contain information about the rotor's position as

$$e_{\alpha} = -\lambda_{\mathrm{PM}} \omega_{\mathrm{r}} \sin(\theta),\ e_{\beta} = \lambda_{\mathrm{PM}} \omega_{\mathrm{r}} \cos(\theta). \tag{1.11}$$

To compute back-EMF voltages by Equation (1.9), only voltages and phase currents were required. Knowing e_{α} and e_{β} values allows for extracting the rotor position θ. For computing θ from e_{α} and e_{β} voltages, the PLL approach was used. PLL is a well-liked method because it not only cleans sinusoidal data but also tracks it (Lascu & Andreescu, 2020; Tan et al., 2018). Additionally, it can be used at low signal-to-noise ratios (SNR) conditions. There are three main parts to PLL: a voltage-controlled oscillator (VCO), a phase detector (PD), and a low-pass (LP) filter. Where PD is performed with transformation Equation (1.5), LP with proportional-integral (PI) controller and VCO is the integrator and sin and cos generator Fig. 1.3. The PI transfer function is

$$G_{\mathrm{o}}(s) = \frac{k_{\mathrm{p}} + k_{\mathrm{i}} s}{s}. \tag{1.12}$$

And the closed-loop transfer function can be expressed as (Wang et al., 2018)

$$G_{\mathrm{c}}(s) = \frac{k_{\mathrm{p}} s + k_{\mathrm{i}}}{s^2 + k_{\mathrm{p}} s + k_{\mathrm{i}}}, \tag{1.13}$$

where k_p and k_i are PI controller proportional and integral coefficients to select. Comparing the transfer function of a PLL to the transfer function of the second-order, as defined below

$$G_\mathrm{c}(s) = \frac{\omega_\mathrm{n}^2}{s^2 + 2\zeta\omega_\mathrm{n}s + \omega_\mathrm{n}^2}, \tag{1.14}$$

expressions allow us to obtain the values of the PI controller $k_\mathrm{i} = \omega_\mathrm{n}^2$, $k_\mathrm{p} = 2\zeta\omega_\mathrm{n}$. The second-order closed-loop transfer's dynamic behaviour function can be described in terms of two (Ji et al., 2019) parameters: damping factor ζ and natural frequency ω_n. If $0 < \zeta < 1$, poles are complex conjugates and lie in the left half plane, and the system is stable. The natural frequency ω_n could be gotten for desired settling time t_s with equality $\omega_\mathrm{n} = \frac{4}{\zeta t_\mathrm{s}}$.

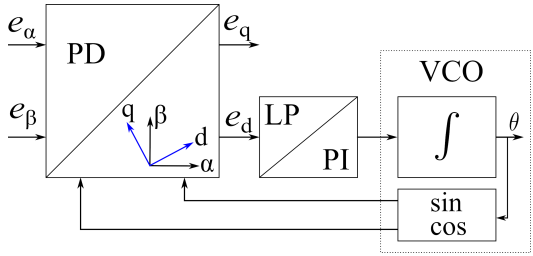

Fig. 1.3. Block diagram of phase-locked loop estimator

1.6. Extended Kalman Filter for Rotor Position and Speed Estimation

The Kalman filter is a mathematical model that estimates the states of linear systems and operates in parallel with the actual system (Auger et al., 2013). It constantly corrects the model using the error signal and provides feedback in the form of the difference between the measured output and the input. The feedback gain is calculated so that the estimate of the state is optimal.

The stationary PMSM model is used to derive the state-space model for the Kalman filter implementation, with the assumption that the speed w_e is the same throughout the switching period (Qiu et al., 2004; Tian et al., 2018) is

$$\begin{aligned}
\frac{\mathrm{d}i_\alpha}{\mathrm{d}t} &= -\frac{R_s}{L_\mathrm{s}}i_\alpha + \frac{\lambda_\mathrm{PM}}{L_\mathrm{s}}\omega_\mathrm{e}\sin\theta + \frac{v_\alpha}{L_\mathrm{s}},\\
\frac{\mathrm{d}i_\beta}{\mathrm{d}t} &= -\frac{R_s}{L_\mathrm{s}}i_\beta - \frac{\lambda_\mathrm{PM}}{L_\mathrm{s}}\omega_\mathrm{e}\cos\theta + \frac{v_\beta}{L_\mathrm{s}},\\
\frac{\mathrm{d}\omega_\mathrm{e}}{\mathrm{d}t} &= 0,\\
\frac{\mathrm{d}\theta}{\mathrm{d}t} &= \omega_\mathrm{e}.
\end{aligned} \tag{1.15}$$

The $\alpha\beta$-axes stator currents i_α, i_β, the angular electrical rotor speed ω_e and the position θ are treated as system states. The voltages v_α, v_β are the input variables. A non-linear dynamic model that takes into account the state change $\mathbf{w}$, as well as measurement noise $\mathbf{v}$ can be expressed generally as

$$\begin{aligned} \dot{\mathbf{x}} &= \mathbf{f}(\mathbf{x}) + \mathbf{B_c}\mathbf{u} + \mathbf{w}, \\ \mathbf{y} &= \mathbf{H}\mathbf{x} + \mathbf{v}. \end{aligned} \tag{1.16}$$

The Gaussian noises $\mathbf{w}$ and $\mathbf{v}$ are white, have a zero-mean, have no correlation and are known to have covariance matrices $\mathbf{Q}$ and $\mathbf{R}$, respectively. The selection of the covariance matrices is critical to good EKF performance $\mathbf{P}$, $\mathbf{Q}$ and $\mathbf{R}$ is crucial. The covariance matrices $\mathbf{P}$, $\mathbf{Q}$ and $\mathbf{R}$ are positive-defined symmetric matrices. The statistical description of the model error is provided by covariance matrices. Matrix $\mathbf{Q}$ addresses the factual portrayal of the model, matrix $\mathbf{R}$ indicates the magnitude of measurement noise, and matrix $\mathbf{P_0}$ contains information about variances under the initial conditions and has a major impact on the transient condition's EKF convergence rate (Bian et al., 2021). Since these are typically unknown, the EKF matrices are typically designed and adjusted through trial-and-error methods (Bolognani et al., 2003).

The model's matrices are expressed as follows

$$\mathbf{f}(\mathbf{x}) = \begin{bmatrix} f_1 \\ f_2 \\ f_3 \\ f_4 \end{bmatrix} = \begin{bmatrix} -\frac{R_s}{L_s} i_\alpha + \frac{\lambda_{PM}}{L_s} \omega_e \sin\theta \\ -\frac{R_s}{L_s} i_\beta - \frac{\lambda_{PM}}{L_s} \omega_e \cos\theta \\ 0 \\ \omega_e \end{bmatrix}, \tag{1.17}$$

$$\mathbf{B}_c = \begin{bmatrix} \frac{1}{L_s} & 0 \\ 0 & \frac{1}{L_s} \\ 0 & 0 \\ 0 & 0 \end{bmatrix}, \quad \mathbf{H} = \begin{bmatrix} 1 & 0 & 0 & 0 \\ 0 & 1 & 0 & 0 \end{bmatrix}, \quad \mathbf{B} \approx T\mathbf{B}_c = \begin{bmatrix} \frac{T}{L_s} & 0 \\ 0 & \frac{T}{L_s} \\ 0 & 0 \\ 0 & 0 \end{bmatrix}, \tag{1.18}$$

where T is the sampling time. The symbol for the state vector $\mathbf{x}$ is denoted as, $\mathbf{u}$ is the input vector and $\mathbf{y}$ is the vector of output

$$\mathbf{x} = \begin{bmatrix} i_\alpha & i_\beta & \omega_e & \theta \end{bmatrix}^T, \quad \mathbf{u} = \begin{bmatrix} v_\alpha & v_\beta \end{bmatrix}^T, \quad \mathbf{y} = \begin{bmatrix} i_\alpha & i_\beta \end{bmatrix}^T. \tag{1.19}$$

The PMSM model portrayed in Equation (1.17) is non-linear, as the results of factors are involved. The non-linear function $\mathbf{f}(\mathbf{x})$ is roughly represented by a linear set. The Jacobian matrix for continuous time can be expressed as

$$\mathbf{F}_c = \begin{bmatrix} -\frac{R_s}{L_s} & 0 & \frac{\lambda_{PM}}{L_s}\sin\theta & \frac{\lambda_{PM}}{L_s}\omega_e\cos\theta \\ 0 & -\frac{R_s}{L_s} & -\frac{\lambda_{PM}}{L_s}\cos\theta & \frac{\lambda_{PM}}{L_s}\omega_e\sin\theta \\ 0 & 0 & 0 & 0 \\ 0 & 0 & 1 & 0 \end{bmatrix}, \tag{1.20}$$

where the previous estimate of $\mathbf{x}$ is used for discretisation around this point. For advanced execution, the system model Equation (1.16) has to be discretised. The following is how the discrete non-linear dynamic model is expressed

$$\begin{aligned} \dot{\mathbf{x}}_k &= \mathbf{F}_{k-1}\mathbf{x}_{k-1} + \mathbf{B}\mathbf{u}_{k-1} + \mathbf{w}_{k-1}, \\ \mathbf{y} &= \mathbf{H}\mathbf{x}_k + \mathbf{v}_k, \end{aligned} \tag{1.21}$$

where in Equation (1.22) the matrices $\mathbf{x}_k$, $\mathbf{F}_{k-1}$ and $\mathbf{u}_{k-1}$ are discrete matrices of $\mathbf{x}$, $\mathbf{F_c}$ and $\mathbf{u}$, respectively, and the matrices $\mathbf{w}_{k-1}$ and $\mathbf{v}_k$ are discrete matrices of $\mathbf{w}$ and $\mathbf{v}$, respectively, autonomous of the system state. Based on Equation (1.20), after the discretisation of $\mathbf{F}_\mathrm{c}$, the Jacobian matrix is

$$\mathbf{F}_k = \begin{bmatrix} 1 - T\frac{R_s}{L_\mathrm{s}} & 0 & T\frac{\lambda_\mathrm{PM}}{L_\mathrm{s}}\sin\theta & T\frac{\lambda_\mathrm{PM}}{L_\mathrm{s}}\omega_\mathrm{e}\cos\theta \\ 0 & 1 - T\frac{R_s}{L_\mathrm{s}} & -T\frac{\lambda_\mathrm{PM}}{L_\mathrm{s}}\cos\theta & T\frac{\lambda_\mathrm{PM}}{L_\mathrm{s}}\omega_\mathrm{e}\sin\theta \\ 0 & 0 & 1 & 0 \\ 0 & 0 & T & 1 \end{bmatrix}, \tag{1.22}$$

where the matrix $\mathbf{F}$ in Equation (1.22) is a discrete, linearised Jacobian matrix. The steps that are listed below can be used to create the extended Kalman filter. The initial step is a time update of the state vector and the error covariance matrix, in which an expectation based on the previous evaluations $\hat{\mathbf{x}}_{k-1}$ is performed

$$\mathbf{F}_{k-1} = \mathbf{F}(\mathbf{x} = \hat{\mathbf{x}}_{k-1}), \tag{1.23}$$

$$\hat{\mathbf{x}}_k^- = \hat{\mathbf{x}}_{k-1} + T\mathbf{f}(\hat{\mathbf{x}}_{k-1}) + \mathbf{B}\mathbf{u}_{k-1}, \tag{1.24}$$

$$\mathbf{P}_k^- = \mathbf{P}_{k-1}\mathbf{F}_{k-1}{\mathbf{P}_{k-1}}^T + \mathbf{Q}, \tag{1.25}$$

where the Jacobian matrix Equation (1.23) is computed too. It is essential to keep in mind that the state prediction is carried out by integrating Equation (1.24) with Runge-Kutta or another approach that is similar. A measurement update step that corrects the predicted state estimate is the second step. Its error covariance $\mathbf{P}_k^-$ matrix by adjusting the feedback

$$\mathbf{P}_k = (\mathbf{I} - \mathbf{K}_k\mathbf{H})\mathbf{P}_k^-, \tag{1.26}$$

$$\hat{\mathbf{x}}_k = \hat{\mathbf{x}}_k^- + \mathbf{K}_k(\mathbf{y}_k - \mathbf{H}\hat{\mathbf{x}}_k^-), \tag{1.27}$$

where the extended Kalman filter gain matrix $\mathbf{K}_k$ is

$$\mathbf{K}_k = \mathbf{P}_k^-\mathbf{H}^T(\mathbf{H}\mathbf{P}_k^-\mathbf{H}^T + \mathbf{R})^{-1}. \tag{1.28}$$

The Kalman gain matrix Equation (1.29)

$$\mathbf{K} = \begin{bmatrix} K_{11} & K_{12} \\ K_{21} & K_{22} \\ K_{31} & K_{32} \\ K_{41} & K_{42} \end{bmatrix}, \tag{1.29}$$

is utilised as weighting in the estimation update process.

Additionally, the estimated rotor position correction Equation (1.30) to restrict the angle to a 2π is added

$$\hat{\mathbf{x}}_k(4) = \hat{\mathbf{x}}_k(4) - 2\pi k, \quad k = \lfloor \hat{\mathbf{x}}_k(4)/2\pi \rfloor. \tag{1.30}$$

The estimation error covariance matrix $\mathbf{P}$ denotes the state vector's error $\hat{x}$ Equation (1.31).

$$\mathbf{P} = E[(\mathbf{x} - \hat{\mathbf{x}})(\mathbf{x} - \hat{\mathbf{x}})^T] = \begin{bmatrix} P_{11} & P_{12} & P_{13} & P_{14} \\ P_{21} & P_{22} & P_{23} & P_{24} \\ P_{31} & P_{32} & P_{33} & P_{34} \\ P_{41} & P_{42} & P_{43} & P_{44} \end{bmatrix}, \tag{1.31}$$

where $E[\cdot]$ is an operator for calculating the mean of the variable in the brackets. The error covariance matrix $\mathbf{P}$ is the degree of accuracy of the estimate. The estimate's error is large if $\mathbf{P}$ is large, while the estimate's error is small if $\mathbf{P}$ is small. The element P_{44} is the variance of the rotor position, Additionally, it might be a sign of how accurately the extended Kalman filter estimates the rotor's position.

The state is corrected using the measurement update Equation (1.27), which can be expressed as

$$\begin{aligned} \hat{i_{\alpha k}} &= \hat{i_{\alpha k}^-} + K_{11}(i_{\alpha k} - \hat{i_{\alpha k}^-}) + K_{12}(i_{\beta k} - \hat{i_{\beta k}^-}), \\ \hat{i_{\beta k}} &= \hat{i_{\beta k}^-} + K_{21}(i_{\alpha k} - \hat{i_{\alpha k}^-}) + K_{22}(i_{\beta k} - \hat{i_{\beta k}^-}), \\ \hat{\omega}_{e k} &= \hat{\omega}_{e k}^- + K_{31}(i_{\alpha k} - \hat{i_{\alpha k}^-}) + K_{32}(i_{\beta k} - \hat{i_{\beta k}^-}), \\ \hat{\theta}_k &= \hat{\theta}_k^- + K_{41}(i_{\alpha k} - \hat{i_{\alpha k}^-}) + K_{42}(i_{\beta k} - \hat{i_{\beta k}^-}). \end{aligned} \tag{1.32}$$

Position correction gains are represented by the elements K_{41} and K_{42} in the Equation (1.32). The rotor position and velocity are primarily estimated in measurement update steps due to the fact that only the stator winding currents can be measured.

1.7. The Unscented Kalman Filter for Position and Speed Estimation

A method for calculating the statistics of a random variable that goes through a non-linear transformation is called the unscented transformation (UT) (Julier & Uhlmann, 2004; Turner & Rasmussen, 2010; Wan & Van Der Merwe, 2000).

The unscented transformation is the primary foundation of the unscented Kalman filter. The idea behind the unscented transformation is similar to the Monte Carlo simulation, which selects samples at random, but this method requires careful weighting selections for each sample. Compared to the Monte Carlo simulation, the number of required samples is significantly reduced by this (Kim & Huh, 2010).

The approach is illustrated in Fig. 1.4. The set of points (sigma points) are selected with their mean and covariance are $\overline{\mathbf{x}}$ and $\mathbf{P}_{\mathrm{x}}$. A cloud of transformed points is produced when the non-linear function is applied individually to each point. The non-linearly transformed mean and covariance can then be estimated by calculating the statistics of the

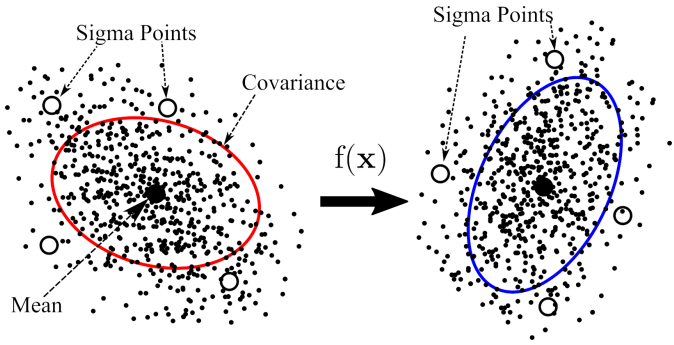

Fig. 1.4. Mean and covariance propagation through a non-linear system

transformed points. When propagated through the non-linear system, these sample points completely capture the true mean and covariance of the Gaussian random variable (Wan & Van Der Merwe, 2000).

The fact that the linearisation of the state and covariances is no longer required is the UKF's primary benefit. The UKF uses a deterministic sampling strategy to capture the mean and covariance estimates with a minimal set of sample points rather than linearising with Jacobian matrices (Borsje et al., 2005).

The complete UKF algorithm for position and speed estimation is

$$[\chi, \mathbf{W}] = \text{SigmaPoints}(\hat{\mathbf{x}}_{k-1}, \hat{\mathbf{P}}_{k-1}, \kappa), \tag{1.33}$$

$$\mathbf{f}\chi = \text{StatePrediction}(\chi, \mathbf{u}), \tag{1.34}$$

$$[\hat{\mathbf{x}}_k^-, \mathbf{P}_k^-] = \text{UT}(\mathbf{f}\chi, \mathbf{W}, \mathbf{Q}), \tag{1.35}$$

$$\mathbf{h}\chi = \mathbf{H}\mathbf{f}\chi, \tag{1.36}$$

$$[\hat{\mathbf{y}}_k, \mathbf{P}_\text{y}] = \text{UT}(\mathbf{h}\chi, \mathbf{W}, \mathbf{R}), \tag{1.37}$$

$$\mathbf{P}_{xy} = \sum_{i=1}^{2n+1} W_i \{\mathbf{f}\chi_i - \hat{\mathbf{x}}_k^-\}\{\mathbf{h}\chi_i - \hat{\mathbf{y}}_k\}^T, \tag{1.38}$$

$$\mathbf{K}_k = \mathbf{P}_{xy}\mathbf{P}_y^{-1}, \tag{1.39}$$

$$\hat{\mathbf{x}}_k = \hat{\mathbf{x}}_k^- + \mathbf{K}_k(\mathbf{y}_k - \hat{\mathbf{y}}_k), \tag{1.40}$$

$$\mathbf{P}_k = \mathbf{P}_k^- - \mathbf{K}_k\mathbf{P}_y\mathbf{K}_k^T, \tag{1.41}$$

there matrix $\mathbf{H}$ is same as in EKF 1.18.

The following is a list of the additional algorithms used in the UKF implementation. Where, Algorithm 1 computes the sigma points and weights. Algorithm 2 is an implementation of the unscented transformation. Algorithm 3 is a time update of the current state.

Algorithm 1 Sigma points and weights

function SigmaPoints($\overline{\mathbf{x}}, \mathbf{P}_{\mathrm{x}}, \kappa$)
  $n \leftarrow$ length($\overline{\mathbf{x}}$)
  $\mathbf{U}^T\mathbf{U} \leftarrow \mathbf{P}_x(n+\kappa)$
  $\chi_1 \leftarrow \overline{\mathbf{x}}$
  for $i \leftarrow 1, n$ **do**
    $\chi_{i+1} \leftarrow \overline{\mathbf{x}} + \mathbf{U}_i$
    $\chi_{n+i+1} \leftarrow \overline{\mathbf{x}} - \mathbf{U}_i$
  $W_1 \leftarrow \frac{\kappa}{n+\kappa}$
  for $i \leftarrow 1, n$ **do**
    $W_{i+1} \leftarrow \frac{\kappa}{2(n+\kappa)}$
    $W_{n+i+1} \leftarrow \frac{\kappa}{2(n+\kappa)}$
  return $[\chi, \mathbf{W}]$

Algorithm 2 Unscented transformation

function UT($\chi, \mathbf{W}, \mathbf{Q}$)
  $[n, m] \leftarrow$ size(χ)
  $\mathbf{x} \leftarrow 0$
  $\mathbf{P} \leftarrow 0$
  for $i \leftarrow 1, m$ **do**
    $\mathbf{x} \leftarrow \mathbf{x} + W_i\chi_i$
  for $i \leftarrow 1, m$ **do**
    $\mathbf{P} \leftarrow \mathbf{P} + W_i\{\chi_i - \mathbf{x}\}\{\chi_i - \mathbf{x}\}^T$
  $\mathbf{P} \leftarrow \mathbf{P} + \mathbf{Q}$
  return $[\mathbf{x}, \mathbf{P}]$

Algorithm 3 State prediction

function StatePrediction($\chi, \mathbf{u}$)
  $[n, m] \leftarrow$ size(χ)
  $\mathbf{f}\chi_i \leftarrow 0$
  for $i \leftarrow 1, m$ **do**
    $\mathbf{f}\chi_i \leftarrow \chi_i + T\mathbf{f}(\chi_\mathbf{i}, \mathbf{u})$
  return $\mathbf{f}\chi_i$

Similar to the EKF, the UKF lacks analytical methods for selecting model covariances appropriately. Picking the boundaries is in many cases an experimentation cycle.

1.8. Space Vector Pulse Width Modulation

One important and effective method for modulating the voltage references – the control algorithm's outputs – into the witching sequence is called space vector pulse width modulation (SVPWM) (Xu et al., 2022). For the three-phase VSI, SVPWM is a superior computational PWM method due to its lower output voltage distortion and higher AC output voltage (Chethan & Kodeeswara Kumaran, 2019). shows the switching state in each of the six sectors as a two-level VSI space vector diagram. There are six active vectors ($v_1 - v_6$) when voltage is distributed throughout the load, and two zero vectors, v_0, and v_7 when the motor terminals are shorted through the upper or lower switches, respectively. Every active vector ($v_1 - v_6$) has the magnitude of $2/3V_{\text{dc}}$, is aligned in one of six possible positions, and is shifted at a $\pi/3$ angle apart from each other, as shown in Fig. 1.5. The zero vectors, v_0, v_7, are shown in the centre. Fig. 1.5

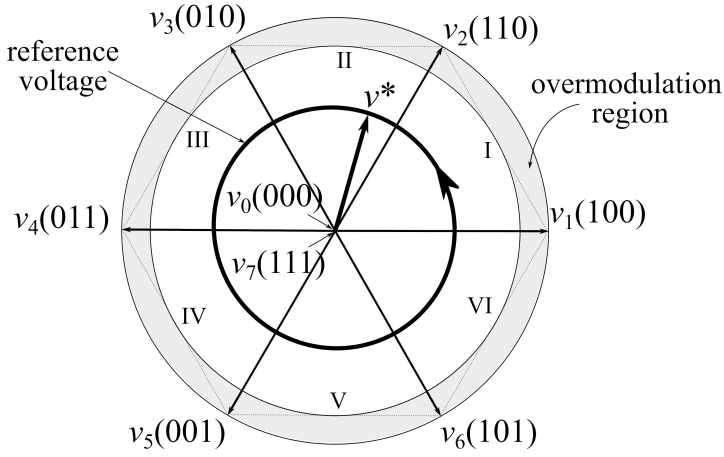

Fig. 1.5. Space vectors in three-phase voltage source inverter

1.9. Initial Rotor Position Estimation

At a standstill operation, the motor voltages and currents are zero; the system of rotor position estimation using the EKF algorithm gives no information for the initial position. To ensure a stable start, a different method for estimating the rotor's position at a standstill must be developed. Due to the PMSM's saliencies, the only information available is the phase inductance, which is a function of rotor position (Boussak, 2005).

Admittance is also expressed as $Y_0 + Y_2 \cos(2\theta)$ due to the salient-pole PMSM inductance's $L_0 + L_2 \cos(2\theta)$ form. In other words, the following equations describe how, when the motor is subjected to a fixed excitation AC voltage rather than a constant DC source, the amplitude of the line current is also a function of the rotor position (Matsui &

Takeshita, 1994)

$$
\begin{aligned}
i_{\mathrm{a}}^{\mathrm{peak}} &= i_0 + \Delta i_{\mathrm{a}} = i_0 + \Delta i_0 \cos(2\theta), \\
i_{\mathrm{b}}^{\mathrm{peak}} &= i_0 + \Delta i_{\mathrm{b}} = i_0 + \Delta i_0 \cos\left(2\theta + \frac{2\pi}{3}\right), \\
i_{\mathrm{c}}^{\mathrm{peak}} &= i_0 + \Delta i_{\mathrm{c}} = i_0 + \Delta i_0 \cos\left(2\theta - \frac{2\pi}{3}\right),
\end{aligned}
\tag{1.42}
$$

where currents are phase peak values obtained by properly connecting PMSM windings to supply voltages, as, for example, for $i_{\mathrm{a}}^{\mathrm{peak}}$ current measurement SVPWM vector $V_1(100)$ is used and is shown in Fig. 1.6. The above relation Equation (1.42) is valid under the relatively small current; that is, the machine is not magnetically saturated.

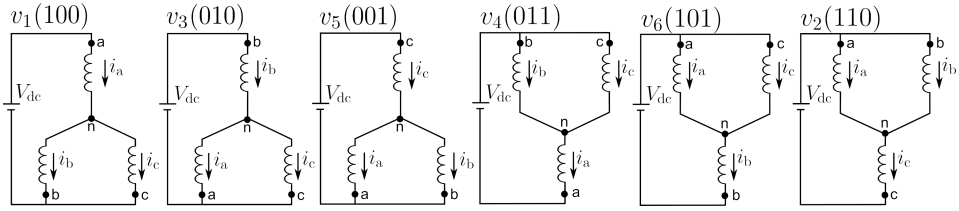

Fig. 1.6. Connection of PMSM at a standstill for $i_{\mathrm{a}}^{\mathrm{peak}}, i_{\mathrm{b}}^{\mathrm{peak}}, i_{\mathrm{c}}^{\mathrm{peak}}$ determination

Two types of suitable sequence DC voltage rectangular pulses are applied at a standstill from the inverter to the stator windings of the motor, and the current peak is measured in order to estimate the initial rotor position. One voltage pulse has a short duration and the other has a long duration.

The Equation (1.42) can be used to determine the ideal situation in which the current amplitude distribution is a sinusoidal function of the rotor position (Matsui & Takeshita, 1994)

$$
i_0 = \frac{1}{3}(i_{\mathrm{a}}^{\mathrm{peak}} + i_{\mathrm{b}}^{\mathrm{peak}} + i_{\mathrm{c}}^{\mathrm{peak}}),
\tag{1.43}
$$

where currents are phase peak values, i_0 is the DC component of the current, and Δi_0 is the fluctuated component's amplitude, which can be determined by connecting PMSM windings to supply voltages correctly. The signs of $\Delta i_{\mathrm{a}}, \Delta i_{\mathrm{b}}, \Delta i_{\mathrm{c}}$ are obtained from Equation (1.42)

The measurement of $i_{\mathrm{a}}^{\mathrm{peak}}$ the inverter's a-phase current is connected to a DC supply, while the b-phase and c-phase currents are zero as is shown in Fig. 1.6. In other words, the $v_1(100)$ space vector pulse width modulation (SVPWM) vector is used for $i_{\mathrm{b}}^{\mathrm{peak}}$ - $v_3(010)$ and for $i_{\mathrm{c}}^{\mathrm{peak}}$ - $v_5(001)$ as shown in Fig. 1.6.

After signs of $\Delta i_{\mathrm{a}}, \Delta i_{\mathrm{b}}, \Delta i_{\mathrm{c}}$ are determined the relation between the rotor position and the combination of signs can be summed up in Table 1.2. The precise position of the rotor can be determined after the $theta$ region has been identified. Using trigonometric identities, the aforementioned expressions can be combined to produce an expression for

the rotor position in Equation (1.42) and isolating the angle terms for θ given as

$$\tan(2\theta) = \sqrt{3}\frac{\Delta i_{\mathrm{c}} - \Delta i_{\mathrm{b}}}{2\Delta i_{\mathrm{a}} - \Delta i_{\mathrm{b}} - \Delta i_{\mathrm{c}}}, \tag{1.44}$$

from Equation (1.44), and with an approximation for small angles. then $\theta \in -\frac{\pi}{12}; \frac{\pi}{12}$ the initial rotor position at standstill is (Boussak, 2005; Matsui, 1996)

$$\theta \approx \frac{1}{2}\tan(2\theta) = \frac{\sqrt{3}}{2}\frac{\Delta i_{\mathrm{c}} - \Delta i_{\mathrm{b}}}{2\Delta i_{\mathrm{a}} - \Delta i_{\mathrm{b}} - \Delta i_{\mathrm{c}}}, \tag{1.45}$$

other regions' rotor positions are given in Table 1.2.

Table 1.2. Relationship between current signs and rotor position

$\theta \in$	Δi_{a}	Δi_{b}	Δi_{c}	θ
$-\frac{\pi}{12}; \frac{\pi}{12}$	$+$	$-$	$-$	$\frac{\sqrt{3}}{2}\frac{\Delta i_{\mathrm{c}}-\Delta i_{\mathrm{b}}}{2\Delta i_{\mathrm{a}}-\Delta i_{\mathrm{b}}-\Delta i_{\mathrm{c}}}$
$\frac{\pi}{12}; \frac{3\pi}{12}$	$+$	$-$	$+$	$\frac{\pi}{6} + \frac{\sqrt{3}}{2}\frac{\Delta i_{\mathrm{a}}-\Delta i_{\mathrm{c}}}{2\Delta i_{\mathrm{b}}-\Delta i_{\mathrm{a}}-\Delta i_{\mathrm{c}}}$
$\frac{3\pi}{12}; \frac{5\pi}{12}$	$-$	$-$	$+$	$\frac{2\pi}{6} + \frac{\sqrt{3}}{2}\frac{\Delta i_{\mathrm{b}}-\Delta i_{\mathrm{a}}}{2\Delta i_{\mathrm{c}}-\Delta i_{\mathrm{a}}-\Delta i_{\mathrm{b}}}$
$\frac{5\pi}{12}; \frac{7\pi}{12}$	$-$	$+$	$+$	$\frac{3\pi}{6} + \frac{\sqrt{3}}{2}\frac{\Delta i_{\mathrm{c}}-\Delta i_{\mathrm{b}}}{2\Delta i_{\mathrm{a}}-\Delta i_{\mathrm{b}}-\Delta i_{\mathrm{c}}}$
$\frac{7\pi}{12}; \frac{9\pi}{12}$	$-$	$+$	$-$	$\frac{4\pi}{6} + \frac{\sqrt{3}}{2}\frac{\Delta i_{\mathrm{a}}-\Delta i_{\mathrm{c}}}{2\Delta i_{\mathrm{b}}-\Delta i_{\mathrm{a}}-\Delta i_{\mathrm{c}}}$
$\frac{9\pi}{12}; \frac{11\pi}{12}$	$+$	$+$	$-$	$\frac{5\pi}{6} + \frac{\sqrt{3}}{2}\frac{\Delta i_{\mathrm{b}}-\Delta i_{\mathrm{a}}}{2\Delta i_{\mathrm{c}}-\Delta i_{\mathrm{a}}-\Delta i_{\mathrm{b}}}$

In point of fact, the PMSM flux vector λ_{PM} can be aligned along the direction, but not the orientation, of the rotor d-axis using the proposed method. By injecting a DC current, the rotor can be initially placed in a known position to eliminate this uncertainty. However, this method can only be used online in situations where initial uncontrolled shaft movement is permitted. According to (Consoli et al., 2001), an offline procedure is required in all other instances.

To distinguish the north magnetic pole between θ and $\theta + \pi$, the magnetic saturation can be accounted for magnetic saturation mainly emerged by applying long-time voltage pulses because of increased currents.

The magnetic saturation effect can be modelled as induction variation due to current. The dq-axis inductances L_{d} and L_{q} can be denoted as a simplified linear function of the dq-axis currents described by (Feng et al., 2016)

$$\begin{aligned} L_{\mathrm{d}} &= \mathrm{f}_{\mathrm{d}}(i_{\mathrm{d}}, i_{\mathrm{q}}) = L_{\mathrm{d0}} - \beta_{\mathrm{d}} i_{\mathrm{d}} - \alpha_{\mathrm{q}} i_{\mathrm{q}}, \\ L_{\mathrm{q}} &= \mathrm{f}_{\mathrm{q}}(i_{\mathrm{d}}, i_{\mathrm{q}}) = L_{\mathrm{q0}} - \beta_{\mathrm{q}} i_{\mathrm{d}} - \alpha_{\mathrm{q}} i_{\mathrm{q}}, \end{aligned} \tag{1.46}$$

where $\alpha_{\mathrm{d}}, \alpha_{\mathrm{q}}, \beta_{\mathrm{d}}, \beta_{\mathrm{q}}$ are the cross-saturation and self-saturation constants respectively. The dq-axis inductances will change roughly linearly with respect to the dq-axis currents when the current variation is small. Because of the small change in dq-axis currents, the q-axis current dominates the variation of q-axis inductance, and the d-axis current simi-

larly dominates the variation of d-axis inductance. To make parameter estimation easier, the cross-saturation constants are assumed to be zero ($\alpha_{\mathrm{d}} = \alpha_{\mathrm{q}} = 0$) because the cross-saturation effect is much smaller than the self-saturation effect (Feng et al., 2016).

If i_{d} is negative, it means that the PM field is in opposition to the armature flux, and if it is positive, it means that the PM and armature fields add up. Therefore, positive and negative i_{q} represents motoring and generating modes, separately. The inductance L_{q} is independent of the i_{q}. Then again, because of the demagnetising impact, L_{d} is higher at negative i_{d}. With positive i_{d}, the magnetic circuit is saturated because of the additive effects of PM and armature flux, causing reduced L_{d} (Rallabandi et al., 2019).

1.10. Analytical Model for Analysing the Electromagnetic Field in the Electrical Machines Overview

In conventional electrically excited machines, such as induction, electrically excited synchronous, and variable reluctance machines, the one-dimensional (1-d) analytical model for analyzing the electromagnetic field is very popular. This model predicts the air gap flux density by multiplying the magneto-motive force and air gap permeance distributions (Zhu et al., 2010). However, when compared to conventional electrically excited machines, the effective air gap width of surface-mounted permanent magnet motors is rather larger, due to ferrite's relative recoil permeability and rare earth magnets are in the range of 1.02 – 1.2 (Zhu et al., 1994). The inter-pole leakage is more serious; the simplification of the 1-d field and the neglect of tangential flux density distribution can result in a relatively large error. Therefore, broad exploration has been led on the two-dimensional (2-d) field analytical model to improve prediction accuracy (Zhu et al., 2010).

The solution of Maxwell's equations is the objective of the Fourier-based modelling strategy. In their differential structure, these major laws of electromagnetism are composed as

$$\nabla \times \mathbf{E} = -\frac{\partial \mathbf{B}}{\partial t},\ \nabla \times \mathbf{H} = \mathbf{B},\ \nabla \cdot \mathbf{B} = 0, \tag{1.47}$$

where vectors B, H, E, and J are the magnetic flux density, the magnetic field strength, the electric field strength and the current density, respectively. The governing equation can be solved in a number of ways, but the most common method is Fourier-based (FB) modelling. However, this description is not appropriate for modelling electrical machines because it is difficult to solve analytically. As a result, the issue is reformulated with the help of a magnetic potential. During research on electric machines, there are two commonly used magnetic potentials, namely, the magnetic vector potential A and the magnetic scalar potential φ (Hannon et al., 2019). By definition, the magnetic scalar potential is a scalar quantity. It is defined through its gradient

$$-\nabla\varphi = \mathbf{H}. \tag{1.48}$$

Laplace's equation governs a differential equation for the magnetic scalar potential in an air gap, and Poisson's equation describes it in the magnet region, based on this definition

and Maxwell's equations

$$\nabla^2\varphi = \frac{\partial^2\varphi}{\partial r^2} + \frac{1}{r}\frac{\partial\varphi}{\partial r} + \frac{1}{r^2}\frac{\partial^2\varphi}{\partial\theta^2} = \begin{cases} 0, & \text{in the airspace;} \\ \frac{\nabla\cdot\mathbf{M}}{\mu}, & \text{in the magnets,} \end{cases} \tag{1.49}$$

where r, θ are the coordinates in 2-d polar system, and M is the magnetisation vector for the magnet and is given in polar coordinates (Kim & Lieu, 1998; Wang et al., 2003)

$$\mathbf{M} = M_{\mathrm{r}}\mathbf{r} + M_{\theta}\boldsymbol{\theta}. \tag{1.50}$$

The magnetic scalar potential is connected to the strength of by

$$H_{\mathrm{r}} = -\frac{\partial\varphi}{\partial r},\ H_{\theta} = -\frac{1}{r}\frac{\partial\varphi}{\partial\theta}. \tag{1.51}$$

The overall solution for the scalar magnetic potential in both airspace and in the magnets has the structure (Zhu et al., 1993)

$$\begin{aligned}\varphi(r,\theta) = &\sum_{n=1}^{\infty}(A_n r^n + B_n R^{-n})\left(C_n\cos(n\theta) + D_n\sin(n\theta)\right) + \\ &+ (A_0\ln\ r + B_0)(C_0\theta + D_0).\end{aligned} \tag{1.52}$$

Curl defines the magnetic vector potential, which is a vector quantity

$$\mathbf{B} = \left(\frac{\partial A_{\mathrm{z}}}{\partial y} - \frac{\partial A_{\mathrm{y}}}{\partial z}\right)\hat{\mathbf{x}} + \left(\frac{\partial A_{\mathrm{x}}}{\partial z} - \frac{\partial A_{\mathrm{z}}}{\partial x}\right)\hat{\mathbf{y}} + \left(\frac{\partial A_{\mathrm{y}}}{\partial x} - \frac{\partial A_{\mathrm{x}}}{\partial y}\right)\hat{\mathbf{z}}. \tag{1.53}$$

Since magnetic motion thickness is in 2-d it follows that $A_{\mathrm{x}} = A_{\mathrm{y}} = 0$ and $A = A_{\mathrm{z}}$.

The general magnetic vector potential A_z solution in the polar coordinate system can be obtained by solving Poisson's equation for a subdomain (i.e., stator slots and PM rotor slots) with sources or Laplace's equation for a subdomain (i.e., air gap, slot openings) without a source, as follows (Zhang et al., 2021)

$$\frac{\partial^2 A_{\mathrm{z}}}{\partial r^2} + \frac{1}{r}\frac{\partial A_{\mathrm{z}}}{\partial r} + \frac{1}{r^2}\frac{\partial^2 A_{\mathrm{z}}}{\partial\theta^2} = \begin{cases} -\mu_0\left(M_{\theta} - \frac{1}{r}\frac{\partial M_{\mathrm{r}}}{\partial\theta}\right), & \text{in the magnets;} \\ -\mu_{0\mathrm{j}}, & \text{in armature windings;} \\ 0, & \text{in the airspace.} \end{cases} \tag{1.54}$$

The general solutions of 1.54 can be obtained through variable separation and written as (Cheng et al., 2015)

$$\begin{aligned}A_{\mathrm{z}} = &(E_0\ln r + F_0)(C_0 + D_0) + \\ &+ \sum_{n=1}^{\infty}(E_n r^n + F_n r^{-n})(C_n\sin(n\theta) + D_n\cos(n\theta)),\end{aligned} \tag{1.55}$$

where C_0, D_0, E_0 and F_0 are coefficients to be determined. Owing to the symmetry, the general solution 1.55 can be reduced to

$$A_z = E_0 + \sum_{n=1}^{\infty}(E_n r^n + F_n r^{-n}), \tag{1.56}$$

$$B_r = \frac{1}{r}\frac{\partial A_z}{\partial \theta},\ B_\theta = -\frac{\partial A_z}{\partial r}, \tag{1.57}$$

and E_n, F_n and E_0 can be determined by boundary conditions. Using 1.53, the components of magnetic flux density are as described by (Djelloul-Khedda et al., 2018).

Neglecting the magnetic saturation in the PMSM, the resultant air gap flux density caused by a PM can be equivalent to the product of the air gap flux density produced by the PM in the smooth air gap and the relative air gap permeance (Tian et al., 2017).

1.10.1. Armature Reaction Magnetic Flux Density

The dipole nature of the magnetic field produced by the current in the coil is shown by the flux lines in Fig. 1.7. The magnetic field produced by a winding consists of a single N-turn coil. It is accurate enough for our purposes to assume that the air gap contains all of the magnetic circuit's resistance because the armature and field iron has a much greater permeability than air. Around any of the closed paths shown by the flux lines in Fig. 1.7 the magnetomotive force is product $N \cdot i$.

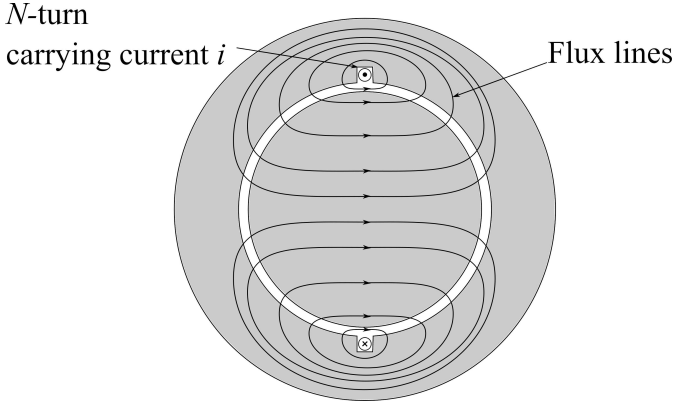

Fig. 1.7. Magnetic flux produced by a winding

Because it was assumed that the reluctance of the magnetic circuit was predominantly that of the air gap, the magnetomotive force's drop in the iron could be neglected, and all the magnetomotive force drop would appear across the air gap. We argued, by symmetry, that the magnetic field intensity H_{ag} in the air gap region on different sides of the rotor are equal in magnitude but different in direction. It follows that the magnetomotive force of the air gap should be similarly distributed; since every flux line crosses the air gap two

time, the magnetomotive force drop across the air gap must be equal to half of the total or $N \cdot i/2$ (Fitzgerald, 2022).

1.10.2. Three-Phase Rotating Magnetic Field

To understand the theory and operation of armature reaction, it is necessary to study the nature of the magnetomotive force wave produced by the windings. As a result, a three-phase motor's winding function can be transformed into the Fourier series as (Li et al., 2013; Liang et al., 2016)

$$\begin{aligned} N_{\mathrm{a}}(\theta_{\mathrm{h}}) &= \sum_{h=1,3,5}^{\infty} N_h \cos\left(h\theta_{\mathrm{h}}\right), \\ N_{\mathrm{b}}(\theta_{\mathrm{h}}) &= \sum_{h=1,3,5}^{\infty} N_h \cos\left(h\theta_{\mathrm{h}} - h\frac{2}{3}\pi\right), \\ N_{\mathrm{c}}(\theta_{\mathrm{h}}) &= \sum_{h=1,3,5}^{\infty} N_h \cos\left(h\theta_{\mathrm{h}} - h\frac{4}{3}\pi\right), \end{aligned} \tag{1.58}$$

Assuming the three-phase winding current is given by

$$i_{\mathrm{a}}(\omega t) = i_1 \cos\left(\omega t\right),\ i_{\mathrm{b}}(\omega t) = i_1 \cos\left(\omega t - \frac{2}{3}\pi\right),\ i_{\mathrm{c}}(\omega t) = i_1 \cos\left(\omega t - \frac{4}{3}\pi\right), \tag{1.59}$$

the stator magnetomotive force is given by

$$F_{\mathrm{s}} = N_{\mathrm{a}} i_{\mathrm{a}} + N_{\mathrm{b}} i_{\mathrm{b}} + N_{\mathrm{c}} i_{\mathrm{c}} = \frac{3}{2} \sum_{h=1,3,5}^{\infty} F_h \cos\left(h\theta_{\mathrm{h}} + \omega t\right). \tag{1.60}$$

Thus, from Equation (1.60) neglecting higher order harmonics, the result of the three windings by $2\pi/3$ in the space phase and causing winding currents to be displaced by $2\pi/3$ in the time phase is a created single positive travelling magneto motiveforce wave.

The air gap magneto motiveforce distribution of Fig. 1.7 is equal to the line integral of H_{ag} across the air gap. For this case of constant radial magnetic flux intensity H_{ag}, this integral is simply equal to the product of air gap radial magnetic field H_{ag} times the air gap length g, and thus H_{ag} can be found simply by dividing the air gap F_{s} by the air gap length g and magnetic flux density is $B_{\mathrm{ag}} = \mu_0 \mu_{\mathrm{r}} H_{\mathrm{ag}} = \mu_0 \mu_{\mathrm{r}} \frac{F_{\mathrm{s}}}{g}$, where μ_{r} is the relative permeability of the air gap.

1.10.3. Stator Slot Influence on Flux Distribution

The distribution of flux in the air gap and the magnets is influenced by the motor's slots. Slotting influences the magnetic field in two ways. First, reduces the total flux per pole and affects the flux distribution in both the air gap and magnets. Open-circuit field distribution is determined from the result of the field generated by the magnets when stator slot open-

ings are neglected and the relative permeance function of the slotted air gap region (Zhu & Howe, 1993b). Additionally, forces are generated when the magnetic field interacts with the sides of the tooth which creates a cogging torque. So far the magnetic field distribution for the slotless PMSM is known. After that, the product of the flux density produced by the magnets in a slotless rotor and the relative air gap permeance is used to calculate the actual open-circuit flux density

$$\tilde{B}_{\mathrm{PM}}(\alpha, \theta, r) = B_{\mathrm{PM}}(\alpha, \theta, t)\tilde{\lambda}(\theta, r), \tag{1.61}$$

where α rotor position angle and θ is the spatial angle with respect to the stator fixed frame. There are many different modelling techniques to obtain relative permeance: harmonic modelling (HM), relative permeance (RP), complex relative permeance (CP), conformal mapping (CM), Schwarz-Christoffel toolbox (SC) and finite element method (FEM). But with different accuracy and computational complexity (Ramakrishnan et al., 2016).

1.10.4. Maxwell's Stress Tensor in the Definition of Torque

According to the Maxwell stress theory (MST), the instantaneous electromagnetic torque equation in the integral form can then be written as (Filho et al., 2020; Gómez et al., 2016; Zhou & Xue, 2021)

$$T^{\mathrm{MST}} = \frac{Lr^2}{\mu_0} \int_0^{2\pi} B_{\mathrm{r}} B_\theta \, \mathrm{d}\theta, \tag{1.62}$$

where r is the radius in the air gap of the integration surface, B_{r} and B_θ are radial and tangential flux density at radius r, respectively, and L is the active axial length of the electrical machine. The magnetic flux densities, B_{r} and B_θ, are the sum of rotor PMs and armature reaction magnetic field and are given as

$$B_{\mathrm{r}} = B_{\mathrm{r}}^{\mathrm{PM}} + B_{\mathrm{r}}^{\mathrm{AR}}, B_{\theta} = B_{\theta}^{\mathrm{PM}} + B_{\theta}^{\mathrm{AR}}, \tag{1.63}$$

where $B_{\mathrm{r}}^{\mathrm{PM}}$ and B_{θ}^{PM} are radial and tangential components of the flux density due to PMs in the air gap and $B_{\mathrm{r}}^{\mathrm{AR}}$ and B_{θ}^{AR} are radial and tangential components of the flux density due to armature reaction in the air gap. Applying Equation (1.63) in Equation (1.62) results as follows

$$T^{\mathrm{MST}} = \frac{Lr^2}{\mu_0} \int_0^{2\pi} (B_{\mathrm{r}}^{\mathrm{PM}} + B_{\mathrm{r}}^{\mathrm{AR}})(B_{\theta}^{\mathrm{PM}} + B_{\theta}^{\mathrm{AR}}) \, \mathrm{d}\theta. \tag{1.64}$$

The instantaneous electromagnetic torque in Equation (1.64) can be summarised in three major components: the cogging torque ($_{\mathrm{cog}}^{\mathrm{MST}}$); the reluctance torque ($T_{\mathrm{rel}}^{\mathrm{MST}}$) and the electrical torque ($T_{\mathrm{e}}^{\mathrm{MST}}$). The torque component

$$T_{\mathrm{cog}}^{\mathrm{MST}} = \frac{Lr^2}{\mu_0} \int_0^{2\pi} B_{\mathrm{r}}^{\mathrm{PM}} B_{\theta}^{\mathrm{PM}} \, \mathrm{d}\theta, \tag{1.65}$$

is known as the cogging torque and is due to existing PMs and stator slots interaction between the magnetic poles and the stator teeth (Liu et al., 2017) and for slotless PMSM is almost zero. The cogging torque is the reluctance torque when the permanent magnet is drawing nearer or leaving the stator teeth, and it is independent of the stator current (Xia et al., 2015). Very often, the cogging torque period is given by a simple expression (Guziński et al., 2019; Min & Sarlioglu, 2017; Simón-Sempere et al., 2017)

$$\theta_{\text{cog}} = \frac{2\pi}{\text{lcm}(2p, Q_{\text{s}})}, \tag{1.66}$$

where function lcm is for finding the lowest common multiple numbers. The torque component

$$T_{\text{rel}}^{\text{MST}} = \frac{Lr^2}{\mu_0} \int_0^{2\pi} B_{\text{r}}^{\text{AR}} B_{\theta}^{\text{AR}} \, \text{d}\theta, \tag{1.67}$$

is known as the reluctance torque and is due to just the AR flux (from the stator current) density. For salient PMSMs ($L_{\text{d}} = L_{\text{q}}$) the reluctance torque is zero. The mutual torque component

$$T_{\text{e}}^{\text{MST}} = \frac{Lr^2}{\mu_0} \int_0^{2\pi} (B_{\text{r}}^{\text{PM}} B_{\theta}^{\text{AR}} + B_{\text{r}}^{\text{AR}} B_{\theta}^{\text{PM}}) \, \text{d}\theta. \tag{1.68}$$

or electromagnetic torque refers to the interaction between PM flux and armature flux in the air gap – also known as the interaction between back-EMF and armature current.

Both the rotor permanent magnetisation and the stator armature currents determine the resulting total rotating field under load. It has a fundamental space component that travels at synchronous speed and is responsible for the production of the average torque. The average torque contribution of the open-circuit flux density high-order space harmonics produced by the rotor magnetisation is zero because their polarity differs from that of the fundamental space harmonic of the armature MMF, which is the only stator harmonic that travels at a synchronous speed. Limiting only the first electrical harmonic allows for a reasonable estimation of the average torque component. The average torque may be evaluated with the dq formulation (Popescu, 2006; Vyšniauskas, 2021)

$$T_{\text{e}}^{\text{dq}} = \frac{3}{2} p \left(\lambda_{\text{d}} i_{\text{q}} - \lambda_{\text{q}} i_{\text{d}} \right) = \frac{3}{2} p \left(\lambda_{\text{PM}} i_{\text{q}} + (L_{\text{d}} - L_{\text{q}}) i_{\text{q}} i_{\text{d}} \right), \tag{1.69}$$

where λ_{d} and λ_{q} are flux linkages for the d-axis and the q-axis, respectively.

1.10.5. Inductance Calculation

Self-inductance and mutual inductance are both functions of rotor position in brushless machines with surface-inset magnets because of the saliency of the rotor. The flux linkage per coil to the winding of k-phase due to the magnetic flux produced by the winding of

j-phase can be expressed as (Rahideh et al., 2013)

$$\lambda_{j,k} = pN_{\mathrm{s}}Lr \int_{-\frac{\theta_{\mathrm{c}}}{2p}+\frac{2\pi(k-1)}{3p}}^{\frac{\theta_{\mathrm{c}}}{2p}+\frac{2\pi(k-1)}{3p}} B_{\mathrm{r}}^{\mathrm{AR}}\,\mathrm{d}\theta, \tag{1.70}$$

for $k = 1, 2, 3$ and $j = 1, 2, 3$, and B_{r} is the flux density distribution's radial component, as produced by j-phase in the winding region, θ_{c} is the coil pitch angle, and r is the radius in the middle of the winding region. The mutual inductance between two-phases is expressed as (Ponomarev et al., 2014; Rahideh et al., 2013) $L_{j,k} = \frac{\lambda_{j,k}}{i_j}$ there i_j is the current of j-phase. The inductances ($L_{j,k}$) calculated are the stator self-inductance or mutual inductances and can be written as

$$\begin{bmatrix} L_{11} & L_{12} & L_{13} \\ L_{21} & L_{22} & L_{23} \\ L_{31} & L_{32} & L_{33} \end{bmatrix} = \begin{bmatrix} L_{\mathrm{aa}} & L_{\mathrm{ab}} & L_{\mathrm{ac}} \\ L_{\mathrm{ba}} & L_{\mathrm{bb}} & L_{\mathrm{bc}} \\ L_{\mathrm{ca}} & L_{\mathrm{cb}} & L_{\mathrm{cc}} \end{bmatrix}, \tag{1.71}$$

where inductances are given in Equation (1.2). Then the synchronous inductances (L_{d} and L_{q}) can be calculated from Equation (1.2) with the following calculation. The leakage inductance L_{sl} can be found by

$$\begin{aligned} L_0 &= L_{\mathrm{sl}} + L_{\mathrm{s0}} = \frac{1}{3}\left(L_{\mathrm{aa}} + L_{\mathrm{bb}} + L_{\mathrm{cc}}\right), \\ M_0 &= -\frac{1}{2}L_{\mathrm{s0}} = \frac{1}{3}\left(L_{\mathrm{ab}} + L_{\mathrm{bc}} + L_{\mathrm{ca}}\right), \\ L_{\mathrm{sl}} &= L_0 + 2M_0. \end{aligned} \tag{1.72}$$

And the magnetising inductance L_{s0} due to the fundamental air gap flux is $L_{\mathrm{s0}} = -2M_0$. The inductance fluctuation L_{s2} due to the rotor position-dependent flux can be found by

$$\begin{aligned} L_{\mathrm{s2}}\cos(2\theta) &= L_{\mathrm{aa}} - L_0, \\ L_{\mathrm{s2}}\cos(2\theta + 2\pi/3) &= L_{\mathrm{bb}} - L_0, \\ L_{\mathrm{s2}}\cos(2\theta + 4\pi/3) &= L_{\mathrm{cc}} - L_0, \end{aligned} \tag{1.73}$$

and then transforming the three-phase system into a two-phase system by

$$\begin{bmatrix} L_{\mathrm{s2},\alpha} \\ L_{\mathrm{s2},\beta} \end{bmatrix} = \frac{2}{3}\begin{bmatrix} 1 & -\frac{1}{2} & -\frac{1}{2} \\ 0 & \frac{\sqrt{3}}{2} & -\frac{\sqrt{3}}{2} \end{bmatrix}\begin{bmatrix} L_{\mathrm{s2}}\cos(2\theta) \\ L_{\mathrm{s2}}\cos(2\theta + 2\pi/3) \\ L_{\mathrm{s2}}\cos(2\theta + 4\pi/3) \end{bmatrix}, \tag{1.74}$$

and then

$$L_{\mathrm{s2}} = \sqrt{L_{\mathrm{s2},\alpha}^2 + L_{\mathrm{s2},\beta}^2}. \tag{1.75}$$

And finally the synchronous inductances (L_d and L_q) are obtained as

$$L_\mathrm{d} = L_\mathrm{sl} + \frac{3}{2}(L_\mathrm{s0} - L_\mathrm{s2}), L_\mathrm{q} = L_\mathrm{sl} + \frac{3}{2}(L_\mathrm{s0} + L_\mathrm{s2}). \tag{1.76}$$

1.10.6. Back Electromotive Force and Magnet Flux Linkage Calculation

The magnetic flux by the jth phase can be expressed as (Rahideh & Korakianitis, 2012; Rahideh et al., 2013)

$$\phi_j(\alpha) = Lr \int_{-\frac{\theta_\mathrm{e}}{2p}+\frac{2\pi(j-1)}{3p}}^{\frac{\theta_\mathrm{e}}{2p}+\frac{2\pi(j-1)}{3p}} B_\mathrm{r}^\mathrm{PM}(r, \alpha, \theta)\,\mathrm{d}\theta, \tag{1.77}$$

where r is the average winding region radius and α is the angle of the rotor's position relative to the stator's fixed reference axis. The total back-EMF induced in the phase can be analytically found using Faraday's law

$$e_j(\alpha) = -N_\mathrm{s}\omega_\mathrm{e}\frac{\mathrm{d}\phi_j(\alpha)}{\mathrm{d}\alpha}. \tag{1.78}$$

The magnet flux linkage constant λ_PM can be calculated from Equation (1.77) for each phase $j = 1, 2, 3$ calculating flux and transforming into two-phase system

$$\begin{bmatrix} \phi_\alpha \\ \phi_\beta \end{bmatrix} = \frac{2}{3}\begin{bmatrix} 1 & -\frac{1}{2} & -\frac{1}{2} \\ 0 & \frac{\sqrt{3}}{2} & -\frac{\sqrt{3}}{2} \end{bmatrix}\begin{bmatrix} \phi_1 \\ \phi_2 \\ \phi_3 \end{bmatrix}, \tag{1.79}$$

and then

$$\lambda_\mathrm{PM} = pN_\mathrm{s}\sqrt{\phi_\alpha^2 + \phi_\beta^2}. \tag{1.80}$$

The magnet flux linkage λ_PM is used most of the time, it is treated as a known constant. However, demagnetisation or magnet flux ripple, which has a direct impact on the machine's performance, can be caused by a high operating temperature or a stator winding current impulse (Xiao et al., 2010).

1.11. Techniques and Sensors for Magnetic Flux Measurement in Rotating Electrical Machines

Permanent magnets are among the most basic parts in PM motors, which might get harmed through an irreversible demagnetisation process due to different causes. In addition to overload, increased vibrations, and rotor faults, magnet demagnetisation frequently results

in a reduced or unbalanced rotor flux (Choi et al., 2018). It is known that some permanent magnets (NdFeB) corrode, which leads to disintegration. Manufacturing-induced cracks have the potential to accelerate disintegration as well. Furthermore, flux disruptions may result from the magnets being demagnetised (Le Roux et al., 2003). The magnets may also be damaged by direct impact with the motor, causing partial demagnetisation. Additionally, there are times when, the magnets could be exposed to a variety of contaminants, including dust pollution, salt and cooling lubricants among others, which also may lead to disintegration (Urresty et al., 2013). Therefore, for online detection of motor faults, it is of high advantage to take measurements of the magnetic flux density.

Power loss in motors must be visualised using some methods in order to design high-efficiency electrical motors. In operating motors, the magnetic properties of the core, consist of electrical steel sheets that change by the rotating magnetic field and applied stress. Therefore, to construct an appropriate technique, accurate measurement of the magnetic properties of the core modelling must be obtained to express them accurately (Maeda et al., 2018).

Also, controlling permanent magnet synchronous motors requires rotor position estimation or measurement, as well as magnet polarity detection for the startup of the motor. Since reducing the complexity of the system can increase its reliability and reduce the cost associated with the measurements, the use of magnetic flux density measurement for estimation of the PM position and polarity for control of PMSMs drives can be beneficial.

1.11.1. Search Coil-Based Sensing Technology

The shapes of coil-based sensors are typically circular, and they use wire windings with or without a ferromagnetic core and a small number of turns, commonly between 10 and 3000, depending on the application (air gap or stray flux measurement) and dimensions (Lee et al., 2021; Pusca et al., 2010; Ramirez-Nunez et al., 2018). Coil-based sensors' straightforward construction makes them simple to fabricate, which is a significant benefit (Zamudio-Ramirez et al., 2022). However, this technique presents two significant inadequacies. Because of its high magnetic resistance, this hole prevents the flow of magnetic flux. The air gap, because of the search coil thickness, comes into existence between the laminated steel sheets (Solli, 2014). A magnetic flux measurement in synchronous generator using the method of an inserted coil that is inserted into the stator core tooth was presented by (Elez et al., 2008). The same method for PMSM was presented by (Saadoun & Amirat, 2014).

A. External Stray Flux Sensing Technology

The stray flux is the magnetic flux that radiates outside the frame of the machine induced by the stator and rotor currents (Bellini et al., 2006; Zamudio-Ramírez et al., 2020). These currents (and, hence, the stray flux) are impacted when the electric motor works under an fault condition. The two magnetic components of the stray flux can be examined: radial stray flux and axial. The radial field is known to be in a plane that is perpendicular to the motor axis, whereas the axial field is known to be generated by currents in the stator end windings or rotor cage end ring (Romary et al., 2009; Zamudio-Ramírez et al., 2020). It is possible to separately capture the axial and radial stray flux components and even the combination of both by installing suitable sensors on the frame of the motor at specific

positions (Zamudio-Ramírez et al., 2020).

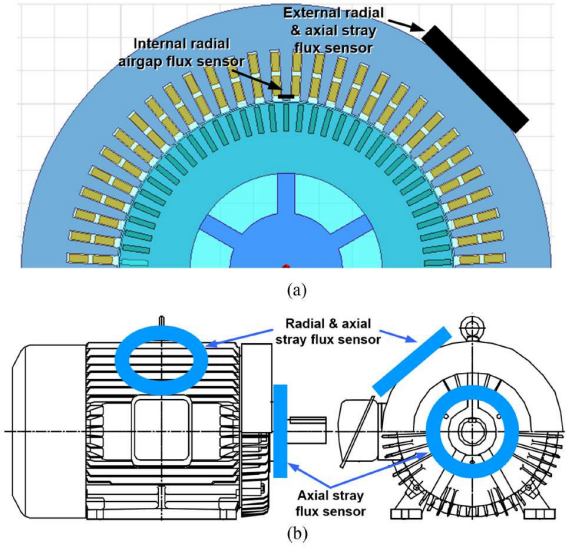

Fig. 1.8. Flux measurements are used to monitor motor condition: (a) measurement of the internal radial air gap flux; and (b) measurement of the external axial stray flux (Park et al., 2020a)

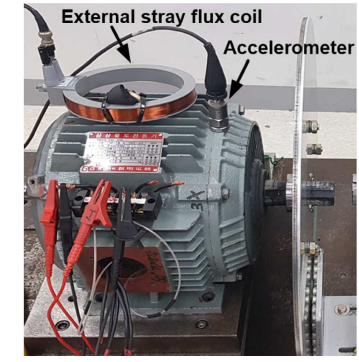

Fig. 1.9. Experimental setup based on the external search coil with 320 turns (Park et al., 2020a)

The external search coil can be put on the radial or axial surface of the motor frame, as shown in Fig. 1.8 (Park et al., 2020a). Fig. 1.9 shows the experimental setup based on the search coil detection method (Park et al., 2020a). Modelling the sources of the electromagnetic field and the attenuation effects caused by the various ferromagnetic components

of the electrical machine that are flown by the field are necessary for the analysis of the external magnetic field. It has been demonstrated that specific parts of the frequency spectrum provide information about the machine's health. In addition, the external magnetic field can give information about where the fault is located (Romary et al., 2009).

B. Internal Air Gap Flux Sensing Technology

This method calls for the inspection of a search coil-induced voltage as a time function or in the frequency domain function. First, consider the voltage induced in an internal stator tooth tip coil for a machine with no rotor faults. The motor excitation frequency will serve as the dominant and fundamental frequency. Higher frequency components will result from the periodicity of rotor bars. The non-sinusoidal stator MMF distribution, i.e., space harmonics, may also induce time harmonic voltages (Elkasabgy et al., 1992).

The relatively small air gap makes it difficult to install flux sensors on the stator tooth surface, despite the advantages of the air gap flux signal in terms of sensitivity (Park et al., 2020b).

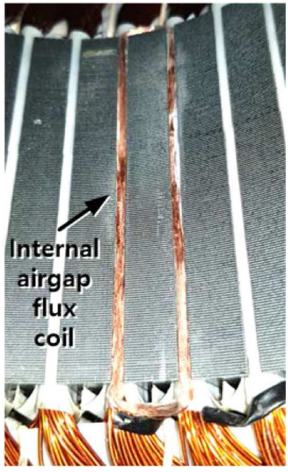

Fig. 1.10. Internal air gap flux search coil location in the stator (Park et al., 2020b)

An experimental setup for measuring the air gap flux inside a synchronous motor is shown in Fig. 1.10, where, a five-turn search coil was placed around the tooth of one slot and placed on the wedges and the end winding, as shown in Fig. 1.10.

1.11.2. Hall Sensors

The flux density in a rotating machine's air gap during transient starting and loading conditions is measured using the Hall effect in a semiconductor. There are several advantages this method has over the traditional exploring coil generator (Ley & Charmatz, 1955).

Many PMSM systems include Hall sensors for determining the rotor's position be-

cause PMSM control relies on the rotor's absolute position. For PMSMs regulated by incremental encoders, Hall sensors are required for obtaining the rotor's initial position. The signals provided as output by Hall sensors are made digital in many PMSM drives for simplifying hardware and for noise immunity (Park et al., 2019b). Recently, it has been demonstrated that making use of signals from analogue hall sensors like improved control performance (Reigosa et al., 2018; Shi et al., 2005; Song et al., 2016), monitoring of PM temperature (Park et al., 2019a) and even torque estimation (Alonso et al., 2021).

Magnetic flux density measurement in an Axial Field Motor using the Hall effect probe was presented by (Lee, 1992). Magnetic flux measurement in a synchronous generator using a Hall sensor installed in the stator core tooth was presented by (Elez et al., 2008). A typical location of three Hall sensors is shown in Fig. 1.11 (Alonso et al., 2019)

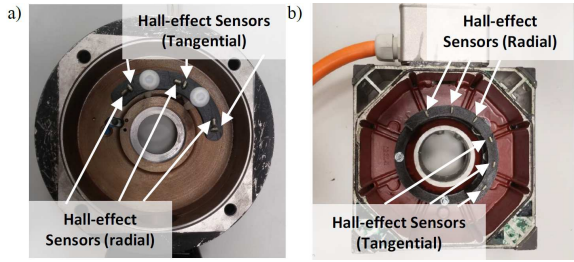

Fig. 1.11. IPMSM end shield with Hall effect sensors (Alonso et al., 2019)

1.11.3. Fibre Bragg Grating Sensing Technology

As a promising alternative for the condition monitoring of electric machines, fibre optic sensing has emerged: its use in machine thermal and mechanical monitoring (Fabian et al., 2018; Mohammed & Djurovic, 2019; Mohammed & Djurović, 2018; Mohammed et al., 2019; Sousa et al., 2016), is attracting increased interest. With its advanced features like small size, immunity to electromagnetic interference, multiplexing, and multi physical sensing, the Fibre Bragg Grating (FBG) sensing technology is a promising option for enabling targeted in situ monitoring of machine multi-physical operating conditions(Mohammed et al., 2020). A typical FBG sensor is shown in Fig. 1.12 (Fracarolli et al., 2016). This sensor uses an FBG structure attached to a magnetostrictive material composed of the rare earth alloy Terfenol-D.

1.11.4. Colossal Magnetoresistance Magnetic Field Density Sensing Technology

Hole-doped manganites are extensively studied because of colossal magnetoresistance (CMR). CMR in these materials refers to the suppression of the resistivity upon application of a magnetic field. They are therefore appealing candidates for employment in magnetic field sensing and magnetic recording devices. They have a common chemical formula $Re_{1-x}A_xMnO_3$ (where Re is a rare earth element and A is a divalent element like

Fig. 1.12. Photograph of an FBG sensor. The dark spot on the right extremity is the Terfenol-D tube (Fracarolli et al., 2016)

Sr, Ca, Ba, Pb, etc.) (Kar et al., 2006). A typical CMR effect-based sensor is shown in Fig. 1.13 (Schneider et al., 2007). Due to remarkable magnetic and transport properties and applications to magnetic fields, the CMR effect has received a lot of attention. This material undergoes a ferromagnetic paramagnetic phase transition accompanied usually with a metal-insulator transition (Hu et al., 2011). The CMR B-scalar sensor works by altering electrical conductivity in response to external magnetic fields of thin polycrystalline $LaSrMnO_3$ films. The primary prerequisites for such movies are low anisotropy of the colossal magnetoresistance, no saturation at high fields, and little changes of electrical conductivity with temperature (Žurauskienė et al., 2010,0).

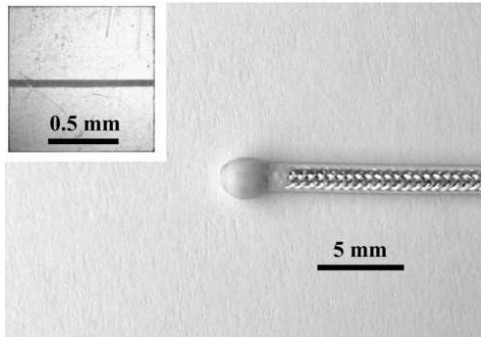

Fig. 1.13. A CMR B-scalar sensor image equipped with a cable (Schneider et al., 2007)

A useful alternative is the utilisation of thin manganite films with a CMR effect. In thin polycrystalline manganite films, it was demonstrated that the CMR phenomenon could be successfully utilised in the creation of CMR B-scalar sensors, which are capable of measuring the magnitude of high pulsed magnetic fields in a tiny volume ($\approx 10^{-2}$ mm^3) (Balevičius et al., 2013).

Based on literature research, a CMR-based sensor currently has not been used for motor air gap magnetic flux density measurement. Moreover, this measurement system was designed for measuring pulsed magnetic fields because they were not able to consider the change in temperature during the measurement of the field.

1.12. Conclusions of the First Chapter and Formulation of the Dissertation Tasks

1. Estimation of PMSM parameters, like stator resistance, stator inductance, rotor speed and position, is critical for improving motor control performance and operational reliability.
2. The PMSM models that account for torque ripple, inductance distributions and back electromotive force waveforms are based on the finite element method, therefore, the computation time using such models is long. The calculation time could be reduced by using PMSM dynamic models based on analytical equations.
3. The analytical equations of magnetic field distribution in PMSM can be obtained using Fourier theory, which allows for deriving the magnetic field equations in the case of two-dimensional problems.
4. By utilising the concepts of relative permeance function, the analytical PMSM models can be extended to account for the impact of stator slot openings on the magnetic field distribution.
5. Magnetic field sensors are needed to directly measure the magnetic field in motors and to check the validity of the modelling. However, the sensors known so far do not completely satisfy such needs.

Based on the performed literature survey, the following dissertation tasks are formulated:

1. To create a PMSM model based on the analytical equations of magnetic flux density.
2. To develop a vector control method of a PMSM and investigate it experimentally.
3. To develop a PMSM parameter estimation method.
4. To develop and implement a magnetic flux density measurement systems for measuring the magnetic flux density in the PMSM.
5. To perform experimental research of magnetic flux density measurement for a PMSM using the created systems.

2

Modelling and Simulation of Permanent Magnet Synchronous Motors Using Analytical Solutions

The analytical literature review on the PMSM control confirmed the need for and importance of developing an enhanced PMSM model. This chapter is dedicated to the development of a PMSM model based on analytical equations. The following cases of PMSM magnetic field distribution were analysed: field created only by the rotor (open-circuit) and field created only by the stator (armature reaction). The stator slot's impact on the distribution of the magnetic field was also examined. Next, based on the magnetic field analysis, the enhanced PMSM model concept is stated. Then, by utilising an enhanced PMSM model the field-oriented control simulation for different PMSM types of the PMSM model is analysed. Finally, with the help of an enhanced PMSM model, the speed and position estimator's modelling results are provided.

The research results were published in author publications (Dilys, 2020; Dilys et al., 2021;). The results are announced in international ICACE (London, 2022), Open Readings (Vilnius, 2022), "eStream" (Vilnius 2017, 2022) and national "Science – the Future of Lithuania" (Vilnius, 2017, 2019) and "FizTech" (Vilnius 2019, 2021) scientific conferences.

2.1. Modelling Open-Circuit Magnetic Field

The open-circuit flux density is then determined from the product of the flux density produced only by the magnets in a slotless rotor and with zero armature current. The magnetic field density distribution with different PMSM rotor configurations is analysed as suitors for the enhanced PMSM model.

2.1.1. Surface-Mounted Magnets

A general method of analysis predicts the magnetic field distribution in PMSMs equipped with surface-mounted magnets (Zhu et al., 2002). Using this method of analysis, the simulation of magnetic field distribution in the air gap region was presented. The strategy is based on two-dimensional models in polar coordinates. It takes into account the effects of both permanent magnets and the geometry of the stator windings. The PMSM geometrical model with surface-mounted permanent magnets is shown in Fig. 2.1. In polar coordinates, the residual magnetisation vector $\vec{M} = M_\mathrm{r}\vec{r} + M_\Theta\vec{\theta}$ is given by (Zhu et al., 2002).

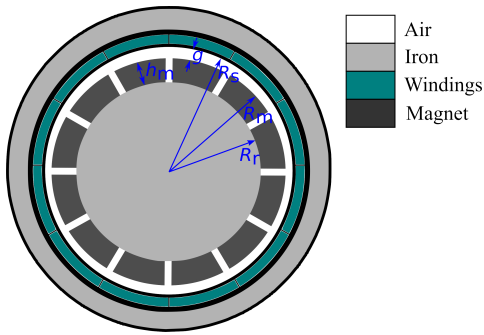

Fig. 2.1. Surface-mounted PMSM model view

The magnetisation components generally are

$$\begin{aligned} M_\mathrm{r} &= \sum_{n=1,3,5,\ldots}^{\infty} M_{\mathrm{rn}} \cos(np\theta), \\ M_\Theta &= \sum_{n=1,3,5,\ldots}^{\infty} M_{\Theta\mathrm{n}} \sin(np\theta), \end{aligned} \tag{2.1}$$

where for radial magnetisation

$$\begin{aligned} M_{\mathrm{rn}}^{\mathrm{rad}} &= 2\frac{B_\mathrm{r}}{\mu_0}\alpha_\mathrm{p}\frac{\sin(n\pi\alpha_\mathrm{p}/2)}{n\pi\alpha_\mathrm{p}/2}, \\ M_{\Theta\mathrm{n}}^{\mathrm{rad}} &= 0, \end{aligned} \tag{2.2}$$

and for the parallel magnetisation

$$\begin{aligned} M_{\mathrm{rn}}^{\mathrm{par}} &= \frac{B_\mathrm{r}}{\mu_0}\alpha_\mathrm{p}(A_{1n} + A_{2\mathrm{n}}), \\ M_{\Theta\mathrm{n}}^{\mathrm{par}} &= \frac{B_\mathrm{r}}{\mu_0}\alpha_\mathrm{p}(A_{1n} - A_{2n}), \end{aligned} \tag{2.3}$$

where

$$A_{1n} = \frac{\sin[(np+1)\alpha_{\mathrm{p}}\frac{\pi}{2p}]}{(np+1)\alpha_{\mathrm{p}}\frac{\pi}{2p}},$$

$$A_{2n} = \begin{cases} 1, & \text{for } np = 1; \\ \frac{\sin[(np-1)\alpha_{\mathrm{p}}\frac{\pi}{2p}]}{(np-1)\alpha_{\mathrm{p}}\frac{\pi}{2p}}, & \text{for } np \neq 1, \end{cases} \tag{2.4}$$

$$A_{3n}^{\mathrm{rad}} = \begin{cases} \left(np - \frac{1}{np}\right)\frac{M_{\mathrm{m}}}{M_{\mathrm{n}}} + \frac{1}{np}, & \text{for parallel magnetisation;} \\ np, & \text{for radial magnetisation,} \end{cases}$$

It is possible to derive the complete solution for the components of the magnetic field in the air gap and magnet regions from the general solution of Laplacian or Poisson equations (Zhu et al., 2002). The full solution is provided in Annex A.

Table 2.1. Simulation parameters of PMSM with surface-mounted magnets

Parameter name	Symbol	Value
Pole pair number	p	8
Slot number	Q_{s}	12
Air gap length	g	0.5 mm
Slot opening	b_0	1.75 mm
Winding pitch	α_{y}	1.0472 rad
Stator bore radius	R_{s}	42 mm
Magnet radial thickness	h_{m}	4 mm
Remanence	B_{R}	1.12 T
Relative recoil permeability	μ_{r}	1.05
Magnet pole-arc/pole-pitch ratio	α_{p}	0.85
Winding turns	N_{s}	50

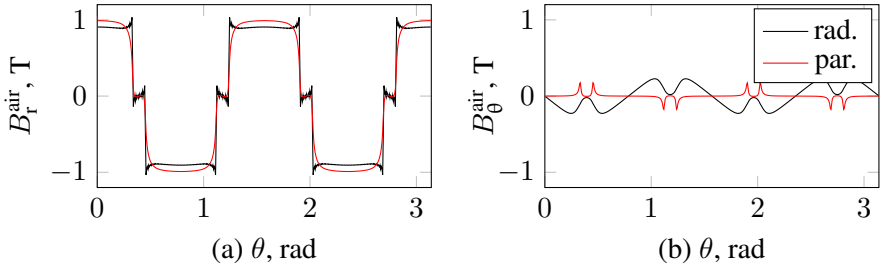

Fig. 2.2. Magnetic field distributions for radial and parallel magnetisation in the middle of the air gap with surface-mounted magnets: (a) the radial component; and (b) the tangential component

The simulation parameters of the motor with surface-mounted magnets for simulation are listed in Table 2.1. From the computer simulation, the obtained results for radial and

tangential components and with two different (radial and parallel) magnetisation simulation results are shown in Fig. 2.2. Fig. 2.2a shows that the shape of radial components for different magnetisation is very similar. However, the tangential components are very different (Fig. 2.2b).

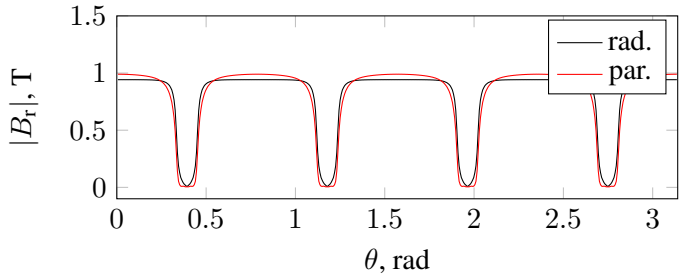

Fig. 2.3. Magnetic field magnitude distributions for radial and parallel magnetisation at the middle of the air gap

The magnetic field magnitude at the middle of the air gap for different magnetisation is shown in Fig. 2.3. The data presented in Fig. 2.3 was obtained from Fig. 2.2.

Based on Fig. 2.3, the magnitude for radial and parallel magnetisation is very similar despite the large difference between tangential components. The tangential component influence of magnitude is small compared to the radial because the tangential component magnitude is much smaller compared to the radial.

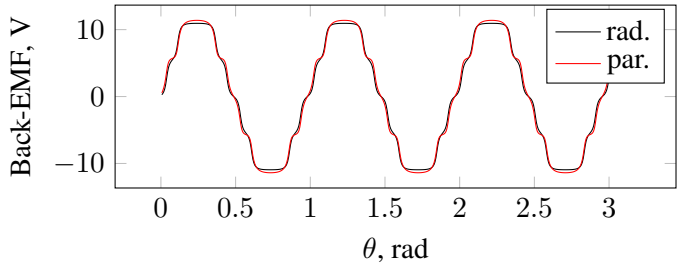

Fig. 2.4. Back-EMF of single phase induced voltages at rotor speed $w_r = 100$ with different magnetisation (radial, parallel)

Fig. 2.4 allows for the conclusion that for radial and parallel PM's magnetisation, the a-phase back-EMF is depicted in Fig. 2.4. trend of the phase back-EMF in each magnetisation pattern is similar to its corresponding radial flux density. Thus, magnetic flux density distribution has a direct influence on the back-EMF shape.

2.1.2. Inset Permanent Magnets Analysis

An analytical solution of the open-circuit magnetic field distribution for slotless brushless machines with inset PMs is described by (Rahideh & Korakianitis, 2011). The following assumptions are applied to the analytical model:

- the motor has infinite axial length;
- the problem is simplified to a two-dimensional case due to the motor symmetry along its shaft;
- the magnetic field quantities have only radial and tangential components;
- PMs have a linear demagnetisation characteristic;
- stator and rotor back-iron has infinite permeability;
- slotless stator structure;
- the air between the PMs and inter-poles has the same permeability as the PMs but with zero magnetisation;
- the electrical conductivities for all regions are zero.

The surface-inset PM topology can be used in three different magnetisation patterns. Fig. 2.5 shows the geometric parameters of internal PM motors with the surface-inset PM topology. The full solution is provided in Annex A. For simulation the parameters of the

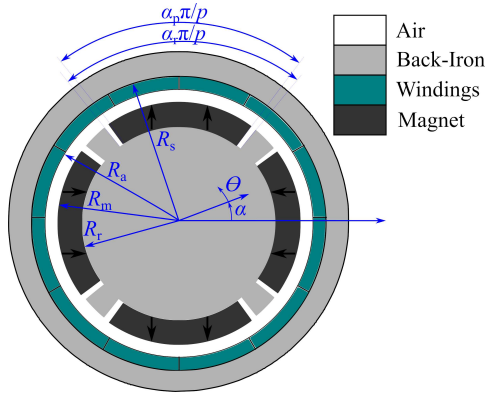

Fig. 2.5. Illustration of geometric parameters of a slotless PM motor with surface-inset PMs

PMSM with surface-inset PMs are listed in Table 2.2. To illustrate the amount of radial and tangential open-circuit flux density in the air gap region, the corresponding simulation results are presented in Fig. 2.6. There are three distinct magnetisation patterns, each of which reveals a significant distinction between the Halbach magnetisation pattern and the parallel and radial magnetisation patterns. The flux density maximum radial component at the air gap region is slightly higher in the parallel magnetisation compared to that of the

Table 2.2. Simulation parameters for a motor with surface-inset PMs

Parameter name	Symbol	Value
Pole pair number	p	8
Slot number	Q_s	12
Axial length	L	30.6 mm
Stator bore radius	R_s	46 mm
Air gap radius	R_a	42 mm
Magnet radius	R_m	41.5 mm
Rotor back-iron radius	R_r	37.5 mm
Magnet pole-arc/pole-pitch ratio	α_p	0.85
Rotor back-iron groove arc to pole pitch ratio	α_r	1
Relative recoil permeability of magnets	μ_r	1.05
PM remanence	B_R	1.12 T
Winding turns	N_s	50

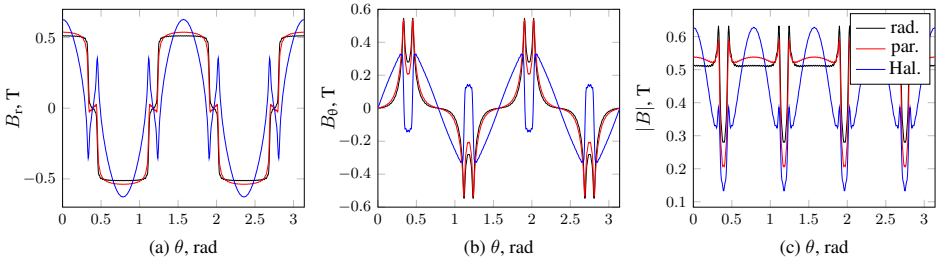

Fig. 2.6. Waveforms with different magnetisation patterns (radial, parallel, and Halbach) for permanent magnet motor with inset magnets in the air gap centre region $r = R_\mathrm{a} - g/2$: (a) radial magnetisation components; (b) tangential magnetisation components; and (c) the magnetic field density magnitude

radial one. However, the Halbach radial component of the flux is the highest (Fig. 2.6a). Even though the Halbach magnetisation has a greater maximum radial component of the flux density than the other two magnetisation patterns, its width is somewhat smaller.

The tangential component of radial and parallel magnetisation is also very similar (Fig. 2.6b). There, the Halbach tangential magnetisation is very different in shape and changes polarity twice at the edge of the magnet.

The absolute values of radial and parallel magnetisation (Fig. 2.6c) are similar; however, the parallel magnetisation shows some arc shape at the middle of the pole. There, the Halbach magnitude (Fig. 2.6c) is very different compared to the radial and parallel magnetisation.

2.1.3. Mixed Magnets

The rotor pole could be formed to reduce the flux density and back electromotive force, harmonics and torque ripple in permanent magnet synchronous machines. This requires making the magnetic flux density distribution as close to a sinusoidal shape as possible. PM materials can be mixed together on the rotor to achieve the desired air gap flux density distribution (Isfahani et al., 2008). Additionally, the mixed material technique, a different pattern of magnetisation is able to change the harmonic components in the air gap, the magnet's magnetic flux density by intentional demagnetisation (Imamura et al., 2019).

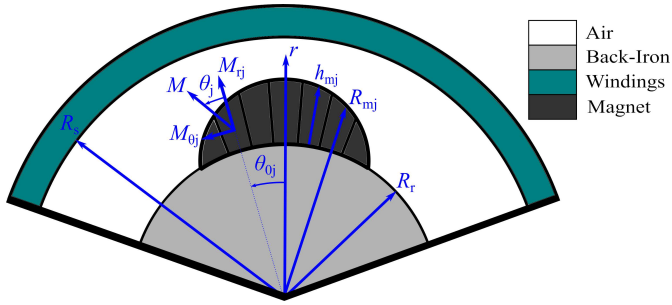

Fig. 2.7. Schematic view of the magnet pole segmenting magnets

Predicting the air gap flux density distribution and back-EMF waveform of surface-mounted PMSMs accounts for magnet shaping and material properties. The analytical model is based on the assumptions: infinite permeable stator and rotor lamination material; negligible eddy current in the stator and rotor laminations; negligible end effect; and negligible eddy current reaction, that is, resistance limited (Wu & Zhu, 2014). Magnets segmented into pieces are shown in Fig. 2.7. Every piece of magnet segment can be viewed as the typical radial sided arc shaped magnet with a pole-arc to pole-pitch ratio $\alpha_{\mathrm{pj}} = \alpha_{\mathrm{p}}/n$, where n is the segment count, a magnet thickness $h_{\mathrm{m}j}$, a magnetisation direction θ_j with respect to its radial direction, a magnet remanence $B_{\mathrm{R}j}$, and positioned at θ_{0j} mechanical degrees, as shown in Fig. 2.7.

The air gap magnetic flux density due to the segmentation can be obtained (Wu & Zhu, 2014) as

$$\begin{aligned} B_{\mathrm{r}} &= \sum_{k=p,3p,\ldots}^{N_{\mathrm{h}}} A_{4k}\big\{[\gamma M_{\mathrm{rc}kj} + \zeta M_{\theta \mathrm{c}kj}]\mathrm{f}_{\mathrm{Br}}\cos(k\theta) + \\ &\quad + [\gamma M_{\mathrm{rc}kj} + \zeta M_{\theta \mathrm{c}kj}]\mathrm{f}_{\mathrm{Br}}\sin(k\theta)\big\}, \\ B_{\theta} &= \sum_{k=p,3p,\ldots}^{N_{\mathrm{h}}} A_{4k}\big\{[-\gamma M_{\mathrm{rs}kj} + \zeta M_{\theta \mathrm{c}kj}]\mathrm{f}_{\mathrm{B}\alpha}\cos(k\theta) + \\ &\quad + [\gamma M_{\mathrm{rc}kj} + \zeta M_{\theta \mathrm{s}kj}]\mathrm{f}_{\mathrm{B}\alpha}\sin(k\theta)\big\}, \end{aligned} \tag{2.5}$$

where, for the internal rotor machine

$$\mathrm{f_{Br}} = \left(\frac{r}{R_\mathrm{s}}\right)^{k-1}\left(\frac{R_{\mathrm{m}j}}{R_\mathrm{s}}\right)^{k+1} + \left(\frac{R_{\mathrm{m}j}}{r}\right)^{k+1}, \tag{2.6}$$

$$\mathrm{f_{B\alpha}} = -\left(\frac{r}{R_\mathrm{s}}\right)^{k-1}\left(\frac{R_{\mathrm{m}j}}{R_\mathrm{s}}\right)^{k+1} + \left(\frac{R_{\mathrm{m}j}}{r}\right)^{k+1}, \tag{2.7}$$

$$A_{4k} = -\mu_0 k/2, \tag{2.8}$$

$$\gamma = \frac{2}{k^2-1}\frac{1}{\rho}\left[(1-k) - 2\left(\frac{R_\mathrm{r}}{R_{\mathrm{m}j}}\right)^{k+1}\right], \tag{2.9}$$

$$\zeta = \frac{2}{k^2-1}\frac{1}{\rho}\left[(k-1) - 2\left(\frac{R_\mathrm{r}}{R_{\mathrm{m}j}}\right)^{k+1}\right], \tag{2.10}$$

$$\rho = (\mu_\mathrm{r}+1)\left[1-\left(\frac{R_\mathrm{r}}{R_\mathrm{s}}\right)^{2k}\right] - (\mu_\mathrm{r}-1)\left[\left(\frac{R_{\mathrm{m}j}}{R_\mathrm{s}}\right)^{2k} - \left(\frac{R_\mathrm{r}}{R_{\mathrm{m}j}}\right)^{2k}\right], \tag{2.11}$$

the magnitudes of the kth spatial order circumferential and radial harmonics of the jth magnet segment

$$\begin{aligned}
M_{\mathrm{rc}kj} &= M_{\mathrm{r}kj}\cos(\theta_j)\cos(k\theta_{0j}) + M_{\theta kj}\sin(\theta_j)\sin(k\theta_{0j}),\\
M_{\mathrm{rs}kj} &= M_{\mathrm{r}kj}\cos(\theta_j)\sin(k\theta_{0j}) - M_{\theta kj}\sin(\theta_j)\cos(k\theta_{0j}),\\
M_{\mathrm{\theta s}kj} &= M_{\mathrm{\theta}kj}\cos(\theta_j)\cos(k\theta_{0j}) + M_{\mathrm{r}kj}\sin(\theta_j)\sin(k\theta_{0j}),\\
M_{\mathrm{\theta c}kj} &= -M_{\mathrm{\theta}kj}\cos(\theta_j)\sin(k\theta_{0j}) + M_{\mathrm{r}kj}\sin(\theta_j)\cos(k\theta_{0j}),
\end{aligned} \tag{2.12}$$

for the radial magnetisation

$$\begin{aligned}
M^{\mathrm{rad}}_{\mathrm{rkj}} &= \frac{4pB_\mathrm{rj}}{k\pi\mu_0}\sin(\frac{k\pi\alpha_\mathrm{pj}}{2p}),\\
M^{\mathrm{rad}}_{\mathrm{\theta kj}} &= 0,
\end{aligned} \tag{2.13}$$

and for the parallel magnetisation

$$\begin{aligned}
M^{\mathrm{par}}_{\mathrm{rkj}} &= \frac{B_\mathrm{rj}\alpha_\mathrm{pj}}{\mu_0}\left\{\frac{\sin((k+1)\alpha_\mathrm{pj}\pi/(2p))}{(k+1)\alpha_\mathrm{pj}\pi/(2p)} + \frac{\sin((k-1)\alpha_\mathrm{pj}\pi/(2p))}{(k-1)\alpha_\mathrm{pj}\pi/(2p)}\right\},\\
M^{\mathrm{par}}_{\mathrm{\theta kj}} &= \frac{B_{rj}\alpha_\mathrm{pj}}{\mu_0}\left\{\frac{\sin((k+1)\alpha_\mathrm{pj}\pi/(2p))}{(k+1)\alpha_\mathrm{pj}\pi/(2p)} - \frac{\sin((k-1)\alpha_\mathrm{pj}\pi/(2p))}{(k-1)\alpha_\mathrm{pj}\pi/(2p)}\right\}.
\end{aligned} \tag{2.14}$$

The back-EMF can be calculated by

$$e = \sum_{k=p,3p,\ldots}^{N_\mathrm{h}} (E_{k\mathrm{s}}\sin(k\omega_\mathrm{r}t) + E_{k\mathrm{c}}\cos(k\omega_\mathrm{r}t)), \tag{2.15}$$

where unknown elements are

$$E_{ks} = 2\omega_r B_{\text{Brck}} L N_s K_{dk} K_{pk} K_{sok},\ E_{kc} = -2\omega_r B_{\text{Brsk}} L N_s K_{dk} K_{pk} K_{sok}, \tag{2.16}$$

$$K_{dk} = \begin{cases} \frac{\sin(\frac{k\pi}{6p})}{q_0 \sin(\frac{k\pi}{3pq_0})}, & q_0 \text{ is even;} \\ \frac{\sin(\frac{k\pi}{6p})}{q_0 \sin(\frac{k\pi}{3pq_0})}, & q_0 \text{ is odd,} \end{cases} \tag{2.17}$$

the winding pitch factor $K_{pk} = \sin(k\alpha_y/2)$, the slot opening factor K_{sok} and The factor q_0 is found by

$$K_{sok} = \frac{\sin(\frac{kb_0}{2R_s})}{\frac{kb_0}{2R_s}},\ q_0 = \frac{N_s}{3\text{gcd}(p, N_s)}, \tag{2.18}$$

where, the function gcd stands for the finding greatest common divisor.

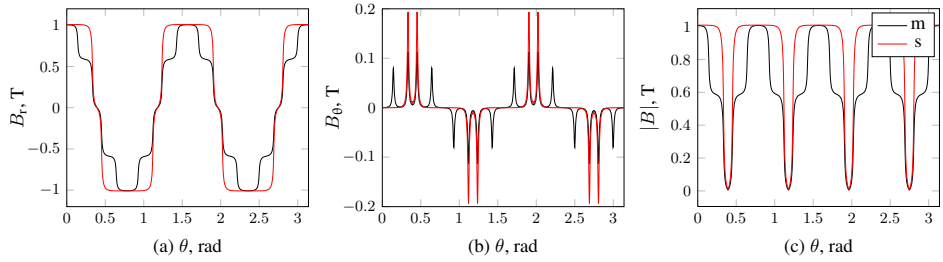

Fig. 2.8. The magnetic flux density distribution with mixed magnets: (a) the radial competent; (b) the tangential competent; and (c) the magnitude

For simulation, the parameters of the PSMM accounting for magnet geometrical shaping are listed in Table 2.3. The magnetic flux density distribution is simulated for two different rotor configurations with different magnet magnetisation patterns. The simulation results of the magnetic flux density distribution in the air gap account for magnet geometrical shaping, as shown in Fig. 2.8. For both rotors, the configuration of the permanent magnets is divided into the same seven segments with the same size and same magnetisation direction, but with different magnet remanence. In the first one (rotor) configuration for all segments, the remanence is the same(s) and can be expressed by $\text{B}^{\text{s}}_{\text{r}j}$, while in another one, mixed(m) magnetic materials are used, and the segment remanence is $\text{B}^{\text{m}}_{\text{r}j}$ (Table 2.3). In Fig. 2.8, the magnetic flux density distribution created by two rotors is shown. The frequency spectrum of the magnetic flux density for both rotors is shown in Fig. 2.9, where the 3$^{\text{rd}}$ harmonic for the rotor with mixed magnets is almost gone compared with the rotor configuration; the same remanence segments are used. The magnetic flux density is closer to the sine shape of the rotor with the mixed material compared with the rotor having the same magnetisation. The armature flux density of one phase can be modelled as a summation of the field densities created by each coil of that phase. The model accounts for the effect of stator winding distribution and the current waveform, and

the large effective air gap (Zhu & Howe, 1993a). The current sheet is divided in so that the current density is uniform along an arc with a length of the slot opening b_0 (Fig. 2.10).

Table 2.3. Simulation parameters for accounting magnet shaping properties

Parameter name	Symbol	Value
Pole pair number	p	8
Stator bore radius	R_s	42 mm
Relative recoil permeability	μ_r	1.05
Magnet pole-arc/pole-pitch ratio	α_p	0.85
Winding turns	N_s	50
Segments count	n	7
Magnets direction vector	θ_j	[0, 0, 0, 0, 0, 0, 0] rad
Mixed magnets remanence vector	$\mathbf{B}^\mathrm{m}_{\mathrm{R}j}$	[0.7, 0.7, 1.2, 1.2, 1.2, 0.7, 0.7] T
Same magnets remanence vector	$\mathbf{B}^\mathrm{s}_{\mathrm{R}j}$	[1.2, 1.2, 1.2, 1.2, 1.2, 1.2, 1.2] T
Magnets thick vector	$\mathbf{h}^\mathrm{r}_{\mathrm{m}j}$	[4, 4, 4, 4, 4, 4, 4] mm
Number of harmonics	N_h	101

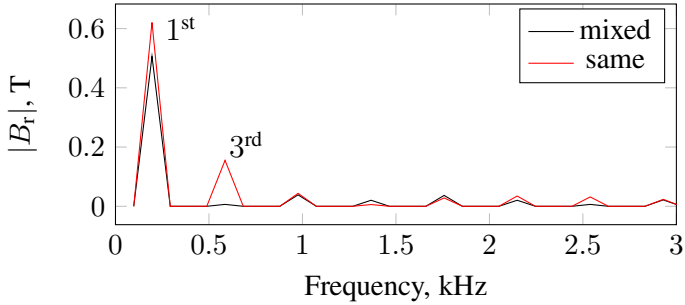

Fig. 2.9. Spectrum analysis of the magnetic flux density with mixed and same magnetisation rotors

2.2. Armature Reaction Magnetic Field

Windings are represented by a current sheet of infinitesimal radial thickness. The current density distribution is given by

$$J = \begin{cases} \frac{i(t)}{b_0}, & -\frac{b_0}{2R_\mathrm{s}} \leq \alpha \leq \frac{b_0}{2R_\mathrm{s}}; \\ 0, & \text{elsewhere.} \end{cases} \tag{2.19}$$

The current density J can be expended by the Fourier series, and by solving the Laplacian equation, the radial component of the magnetic flux density for the distributed current

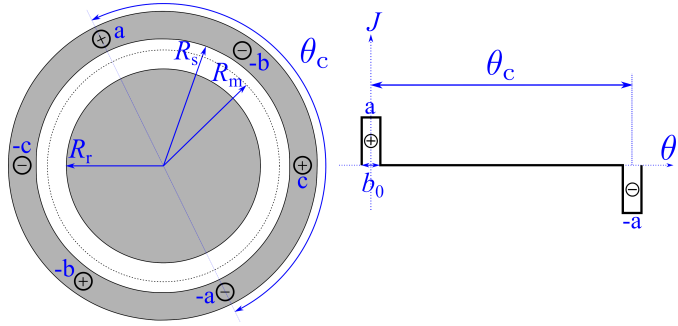

Fig. 2.10. Schematic view of the stator with distributed windings

sheet model of the single coil is derived as (Proca et al., 2003)

$$B(\theta,r)=\frac{2\mu_0}{\pi}\frac{i(t)}{r}\sum_{n=1,2,\ldots}^{N_h}\left\{\frac{\sin\left(n\frac{b_0}{2R_s}\right)}{n\frac{b_0}{2R_s}}\right\}\left(\frac{r}{R_s}\right)^n\frac{1+\left(\frac{R_r}{r}\right)^{2n}}{1-\left(\frac{R_r}{R_s}\right)^{2n}}\cdot \\ \cdot\sin\left(\frac{n\theta_c}{2}\right)\cos\left(n\left(\theta-\frac{\theta_c}{2}\right)\right), \tag{2.20}$$

where $i(t)$ is the phase current at the time moment t and r is the radius in the air gap region.

Table 2.4. Simulation parameters for armature reaction field

Parameter name	Symbol	Value
Slot opening	b_0	6 mm
Stator bore radius	R_s	42 mm
Magnet radius	R_m	41.5 mm
Rotor radius	R_r	37.5 mm
Coil pitch angle	θ_c	π rad
Turns per phase	N_s	50
Fourier harmonic count	N_h	99

The simulation results with motor parameters given in Table 2.4 are shown in Fig. 2.11 when the a-phase current is $i_a = 10$ A, the b-phase current is $i_b = 10$ A and the c-phase current is i_c =-20 A. Fig. 2.11a shows magnetic flux densities for each phases separately. Where the total magnetic flux density as a product for all phases is shown in Fig. 2.11b. The waveform in Fig. 2.11b is similar to a sine wave but with high distortion. It is important to note that the magnetic flux density distribution in Fig. 2.11 is at the time moment then the phase currents are fixed.

The two-dimensional analytical model for predicting the armature reaction field of slotless permanent motors with surface-mounted magnets is given by (Atallah et al., 1998).

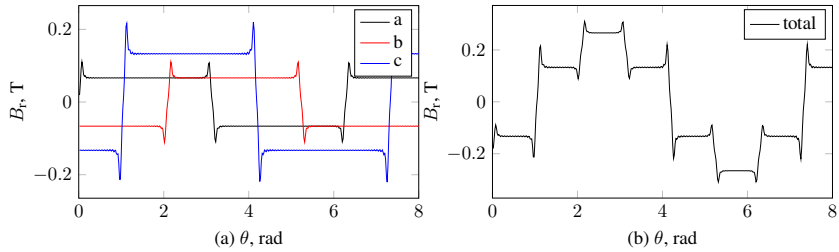

Fig. 2.11. Magnetic flux density waveforms generated by armature: (a) each phase; and (b) the total sum for all phases

In this model, windings are represented by a current sheet accounting for radial thickness. Also, it is assumed that the stator and rotor iron is infinitely permeable. The armature current density J is distributed in the winding region and can be represented by the Fourier series expansion

$$J(\theta) = \sum_{n=1,2,\ldots}^{N_\mathrm{h}} \frac{4N_{sip}}{\pi|R_\mathrm{c}^2 - R_\mathrm{s}^2|} K_{\mathrm{w}n} \sin(np\theta) = \sum_{n=1,2,\ldots}^{N_\mathrm{h}} J_\mathrm{n} \sin(np\theta), \tag{2.21}$$

where N_s, i, p, $K_{\mathrm{w}n}$ are the number of conductors per pole/phase, the phase current, the number of pole pairs, and the winding factor for the n^{th} harmonic, respectively. The winding factor accounting for coil pitch and coil span angles is

$$K_{\mathrm{w}n} = \sin\left(n\frac{\theta_\mathrm{c}}{2}\right) \frac{\sin\left(n\frac{\lambda_\mathrm{c}}{2}\right)}{n\frac{\lambda_\mathrm{c}}{2}}. \tag{2.22}$$

Fig. 2.12 shows the model geometry used to derive the analytical expressions for the magnetic vector potential distribution. Also, the stator and rotor iron is assumed as infinitely permeable. The solution of the magnetic flux density in the air gap region and also in the winding region was derived by (Atallah et al., 1998). Because their motor model is two-dimensional, only the A_z component is not zero. The full solution is provided in Annex A.

Table 2.5. Simulation parameters for the armature reaction field

Parameter name	Symbol	Value
Winding outer radius	R_c	42 mm
Rotor radius	R_r	37.5 mm
Winding thickness	h_w	12 or 3 mm
Coil pitch angle	θ_c	3.14 rad
Span angle of the coil	λ_c	0.1429 rad
Turns per phase	N_s	50
Fourier harmonic count	N_h	99

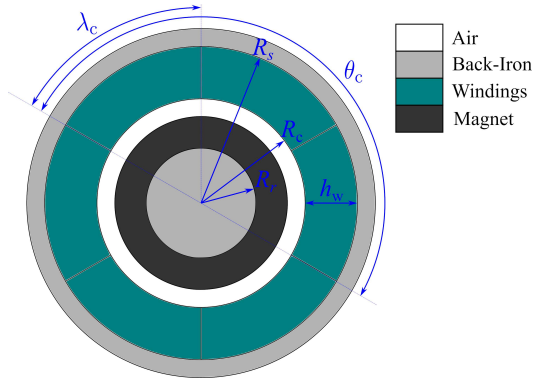

Fig. 2.12. Schematic view of the stator with slotless windings

Simulation results with motor parameters given in Table 2.5 are shown in Fig. 2.13 when the a-phase current is $i_a = 10$ A, the phase-b current is $i_b = 10$ A and the c-phase current is $i_c =$ -20 A in the middle of the air gap. The radial magnetic flux density components are shown in Fig. 2.13a, and in Fig. 2.13b, the tangential components at different winding thicknesses are given. Fig. 2.13 shows that the magnitude of the magnetic flux density is smaller with a longer windings thickness.

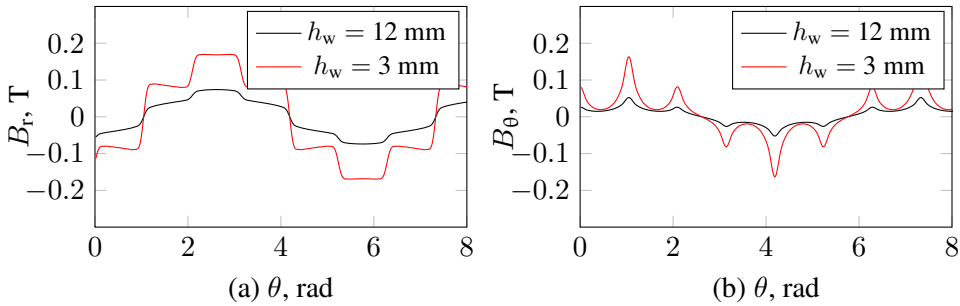

Fig. 2.13. Slotless stator total magnetic flux density generated by armature in the air gap region with different winding thickness h_w in the middle of the air gap: (a) the radial component; and (b) the tangential component

2.3. Stator Slot Influence on Magnetic Field Shaping

Based on conformal mapping, the complex air gap permeance has been analysed of the slot geometry and utilised for precise calculation of the radial and tangential components of the flux density in the air gap with the slots. The method presented by (Zarko et al., 2006) provides a complete analytical field solution in the air gap with a slotted stator.

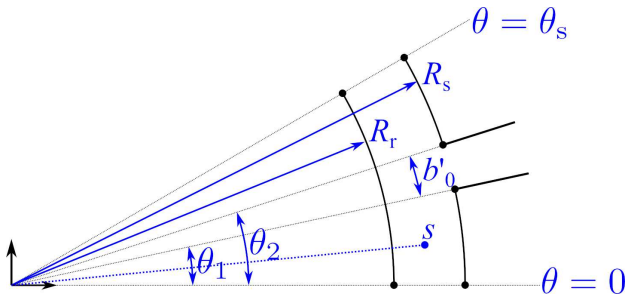

Fig. 2.14. Model of a permanent magnet motor stator slot for calculating the complex relative permeance

The strategy described by (Zarko et al., 2006) is based on conformal mapping – derived knowledge of the flux density distribution along the slot side and is mathematically rigorous. It uses the complex number theory of the conformal transformation and gives a complex number for the relative air gap permeance. Four conformal transformations are required to convert a slotted air gap into a slotless air gap. The slot geometry is shown in Fig. 2.14 and is called the S plane. Logarithmic conformal transformation $z = \ln(s)$ (Rabinovici, 1996), where $s = re^{\mathrm{j}\theta}$ is the known coordinate in the actual geometry with the radius r and angle θ (Fig. 2.14). The second transformation is Schwarz–Christoffel transformation (Gibbs, 1958)

$$\frac{\mathrm{d}z}{\mathrm{d}w} = \mathrm{j}\frac{g'}{\pi}\,\frac{(w-a)^{\frac{1}{2}}(w-b)^{\frac{1}{2}}}{(w-1)w}, \tag{2.23}$$

where w is a new variable in the new transformed map, $g' = \ln(R_\mathrm{s}/R_\mathrm{r})$, and two coefficients are defined

$$b = \left[\frac{b'_0}{2g'} + \sqrt{\left(\frac{b'_0}{2g'}\right)^2 + 1}\right], a = \frac{1}{b}. \tag{2.24}$$

Another transformation is defined

$$t = \mathrm{j}\frac{g'}{\pi}\ln(w) + \ln(R_\mathrm{s}) + \mathrm{j}\frac{\theta_\mathrm{s}}{2}, \tag{2.25}$$

(Zarko et al., 2006). The last is the exponential transformation, defined as $k = e^t$. The field solution can be solved in the slotless air gap and then mapped back to its original S plane. The solution consists of integrating Equation (2.23) and considering the given coordinate $s = re^{\mathrm{j}\theta}$. There, the integral of Equation (2.23) is (Zarko et al., 2006)

$$z = \mathrm{j}\frac{g'}{\pi}\left[\ln\left(\frac{1+\sqrt{\frac{w-b}{w-a}}}{1-\sqrt{\frac{w-b}{w-a}}}\right) - \ln\left(\frac{b+\sqrt{\frac{w-b}{w-a}}}{b-\sqrt{\frac{w-b}{w-a}}}\right) - 2\frac{b-1}{\sqrt{b}}\tan^{-1}\frac{p}{\sqrt{b}}\right] + \tag{2.26}$$
$$+ \ln R_\mathrm{s} + \mathrm{j}\theta_2,$$

where the variable z is the function of w or $z = z(w)$. To find the value of w, which satisfies equation $\ln(s) - z(w) = 0$ is required. For this purpose, a non-linear complex function $\mathrm{f}(w) = \ln(s) - z(w)$ is created and can be solved numerically; for example, the MATLAB function lsqnonlin can be used. After finding the value w, the complex relative permeance can be calculated by (Zarko et al., 2006)

$$\lambda^* = \frac{R_\mathrm{s}}{s} \mathrm{e}^{\mathrm{j}\left(\frac{g'}{\pi}\right)\ln(w)+\frac{\theta_\mathrm{s}}{2}} \frac{w-1}{(w-a)^{\frac{1}{2}}\,(w-b)^{\frac{1}{2}}}, \tag{2.27}$$

the variable λ^* is a complex number and consists of real and imaginary parts. Taking real and imaginary parts, the relative permeance can be calculated for radial and tangential components. The slotted air gap's flux density's radial and tangential components are given

$$\begin{aligned} \tilde{B}_\mathrm{r} &= \mathrm{Re}(B^*\lambda^*) \quad = B_\mathrm{r}\,\mathrm{Re}(\lambda^*) + B_\theta \mathrm{imag}(\lambda^*), \\ \tilde{B}_\theta &= \mathrm{Im}(B^*\lambda^*) \quad = B_\theta \mathrm{real}(\lambda^*) - B_\mathrm{r}\,\mathrm{Im}(\lambda^*), \end{aligned} \tag{2.28}$$

where $B^* = B_\mathrm{r} + \mathrm{j}B_\theta$ is a magnetic flux density written in a complex form.

Table 2.6. Simulation parameters for the relative permeance calculation

Parameter name	Symbol	Value
Air gap length	g	0.5 mm
Slot opening	b_0	1.75 mm
Stator bore radius	R_s	42 mm
Magnet radial thickness	h_m	4 mm
Permanent magnet remanence	B_R	1.12 T

The simulation results of the numerical solution of the complex permeance for the motor model are given in Table 2.6 and Fig. 2.15. Fig. 2.15b shows the imaginary part of the relative permeance, which was not calculated by the previous method. Also, Equation (2.28) shows that the radial magnetic flux component requires both real and imaginary parts of the relative permeance, and the same is for the tangential magnetic flux.

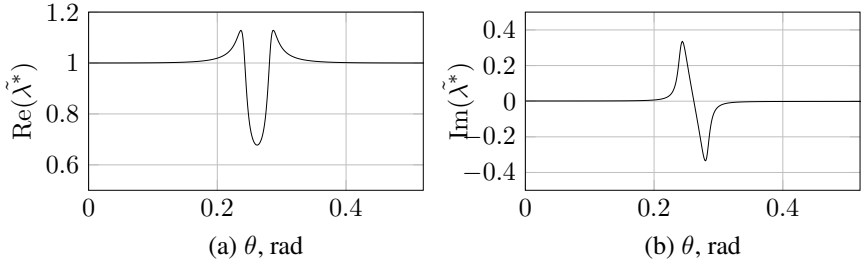

Fig. 2.15. Relative complex air gap permeance per one slot pitch in the middle of the air gap: (a) the real part; and (b) the imaginary part

2.4. Enhanced Motor Model and Its Control Simulation

The enhanced PMSM model is an extension of the ideal PMSM model by embodying additional PMSM parameter update technique based on the analytical solution of the magnetic field. In the enhanced PMSM model, the calculations did not depend on a concrete analytical solution and general magnetic field concepts were introduced instead. The separation principle is shown in Fig. 2.16, where the arrows show the direction of the data flow and how it is related. Because of the separation principle, each analytical solution is isolated and can be easily replaced with another analytical solution without any side effects. Additionally, the enhanced PMSM model considers the torque ripple, inductance distributions and back electromotive force independent of the magnetic field solution type.

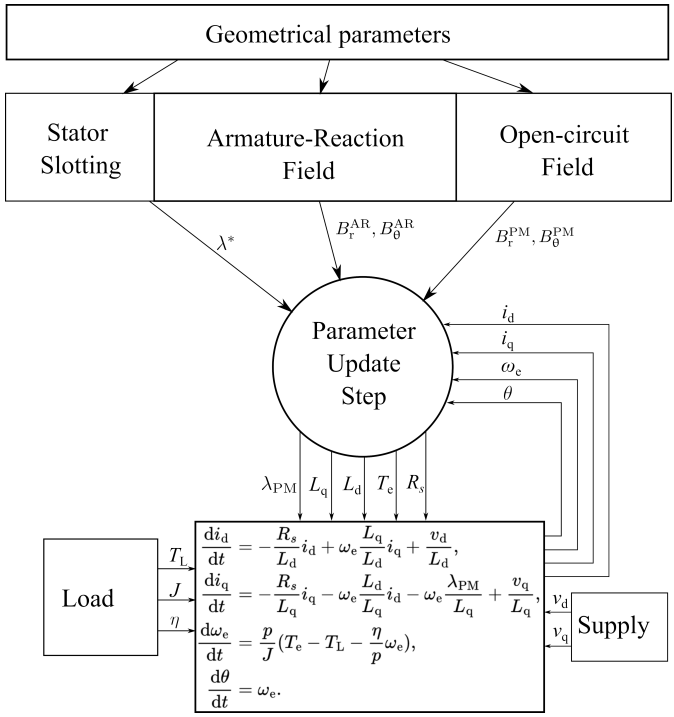

Fig. 2.16. Parameter flow diagram of the enhanced PMSM model

The field-oriented control scheme with the help of the enhanced PMSM model augment can be simulated. An analytical method for predicting the instantaneous magnetic field distribution in the air gap region of various PMSM typologies under any specified load condition and implicitly accounting for the stator winding current waveform and the effect of the stator slot openings is used to develop speed and position control in this model.

This control model is very similar to the standard field-oriented control model, but for the motor parameters, like electromagnetic torque, reluctance torque, cogging torque, synchronous inductances, and back-EMF, the flux linkage is calculated by using an enhanced PMSM model in real-time. Consequently, this enables the simulation to be more realistic because in classical control, these parameters are constant values, while in real-life cases, they change in time.

2.4.1. Control Simulation Using Enhanced Model

The model parameters for field-oriented control with magnetic field distribution in permanent magnet machines equipped with different rotor configurations are given in Table 2.7.

Table 2.7. Enhanced PMSM model parameters for the control simulation

Parameter name	Symbol	Value
Pole pair number	p	4
Slot number	Q_s	6
Magnet surface radius	R_m	59.5 mm
Stator bore inner radius	R_s	60.5 mm
Rotor surface radius	R_r	46.5 mm
Axial length	L	75.6 mm
Winding pitch	α_y	1.0472 rad
Remanence	B_R	1.0 T
Relative recoil permeability	μ_r	1.05
Magnet pole-arc/pole-pitch ratio	α_p	0.85
Winding turns	N_s	15
Slot opening	b_0	2 mm
Winding thickness	h_w	3.5 mm
Coil pitch angle	θ_c	3.14 rad
Span angle of the coil	λ_c	0.2094 rad
Load torque	T_L	20 Nm
Friction coefficient	η	0.005 rad
Moment of inertia	J	0.01 kgm^2

The enhanced PMSM parameters are recalculated every moment as the rotor rotates and differential equations are updated with these parameters. The field-oriented control method is used for controlling motor behaviour. For position estimation extended Kalman filter is used. Speed and current PI controllers are used for controlling the speed and motor currents, respectively. Moreover, the space vector pulse width modulation technique is modelled as well. The motor model is made more realistic using the space vector pulse width modulation technique.

A. Simulation of Control System with Surface-mounted Magnets

The armature reaction field is modelled as slotless permanent magnet brushless machines. Then, the stator slotting is accounted for using a complex relative air gap permeance calculation method. The simulation results are shown in Figs. 2.17, 2.18, 2.19 and 2.20, where the reference speed $w_e^* = 200$ rad/s is set.

Because the model accounts for stator slots, the cogging torque has to be not zero.

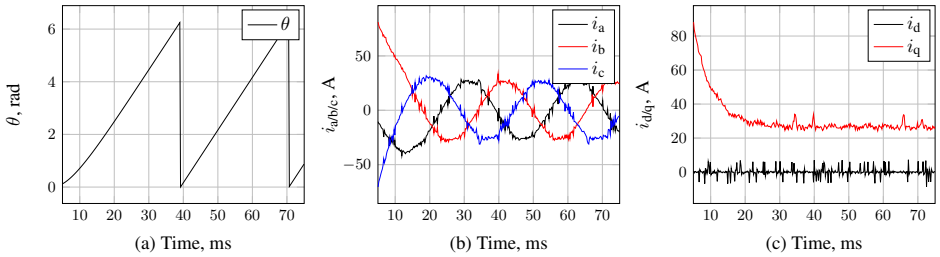

Fig. 2.17. PMSM simulation results with surface-mounted magnets: (a) the rotor position; (b) the phase currents; and (c) the dq-axis currents

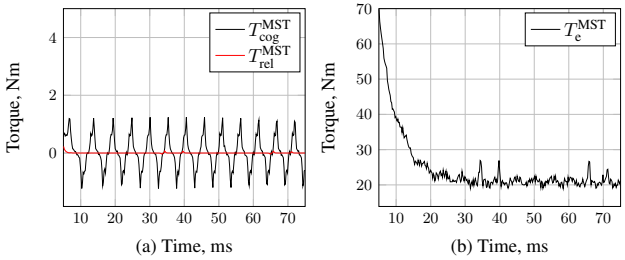

Fig. 2.18. Calculated torque components with surface-mounted magnets: (a) the cogging and reluctance torque; and (b) the electrical torque

Fig. 2.18a shows the cogging torque is not zero, and the cogging torque peak value did not depend on electromagnetic torque. This confirms the theory that the cogging torque did not depend on the stator current and is an effect of motor geometrical parameters. Additionally, Figs. 2.18a and 2.17a allow for a conclusion that the cogging torque oscillates six times per one electrical rotor cycle and confirms the theory of the cogging torque period $\theta_{\text{cog}} = \frac{2\pi}{\text{lcm}(2p,Q_s)}$.

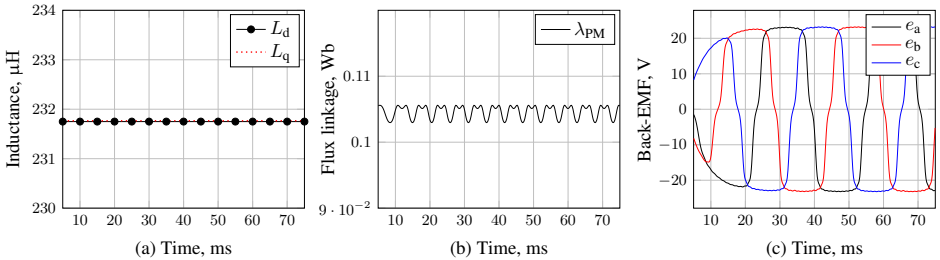

Fig. 2.19. Calculated parameters with surface-mounted magnets: (a) the dq-axis inductances; (b) the flux linkage; and (c) the back-EMF

Fig. 2.19a shows $L_d \approx L_q$ and no produced saliency. Because $L_d = L_q$, the reluctance

torque has to be close to zero, which can be seen in Fig. 2.18a. Fig. 2.19b shows the flux linkage constant (λ_{PM}) value, which is not a constant value and an additional small fluctuation occurs. Fig. 2.19c shows the three-phase back-EMF waveform, having a trapezoidal waveform.

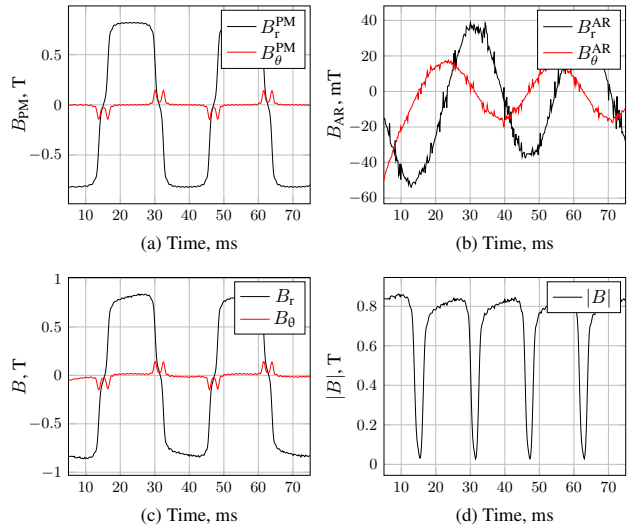

Fig. 2.20. Flux density with surface-mounted magnets: (a) open-circuit; (b) armature reaction; (c) the superposition of the open-circuit and the armature reaction field; and (d) magnetic field magnitude

B. Simulation of a Control System with Mixed Magnets

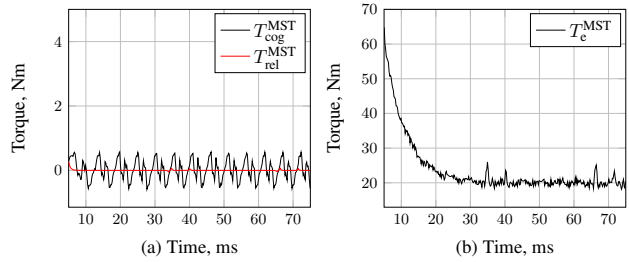

Fig. 2.21. Calculated torque components with surface-mounted segmented magnets: (a) the cogging and reluctance torque; and (b) the electrical torque

For a visual effect, additionally, magnetic field densities for open-circuit and armature reactions are added to Fig. 2.20. The magnetic flux density depends on the rotor position (θ) and sample point (α, r) For simplicity, the sample point of the magnetic field view

in the middle of the air gap and $\theta = 0$ are selected. The magnetic flux density shown in Fig. 2.20 only dependents on the rotor position θ. Figs. 2.20a and 2.20b show open-circuit and armature reaction magnetic flux densities, respectively. The sum of both fields is shown in Fig. 2.20c, where the total magnetic flux density is similar to the open-circuit magnetic field because the armature reaction magnetic field is much weaker, and even a large armature current is flowing via stator windings. Also, Figs. 2.20a and 2.20b show the armature reaction magnetic field is ahead by about $\pi/2$ rad angle to respect the open-circuit magnetic field. It is the field-oriented control job to keep that angle to $\pi/2$ for optimal control. The magnitude $|B| = \sqrt{B_r^2 + B_\theta^2}$ is shown in Fig. 2.20d.

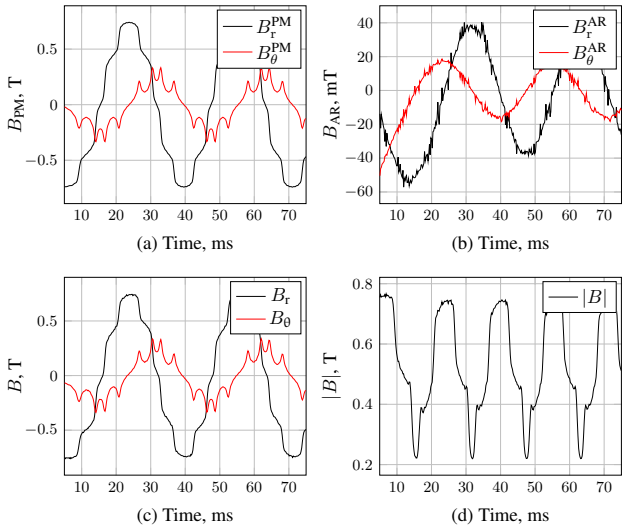

Fig. 2.22. Flux density with surface-mounted segmented magnets: (a) open-circuit; (b) armature reaction; (c) the superposition of the open-circuit and armature reaction field; and (d) the magnetic field magnitude

The same field-oriented control setup with the same stator configuration but a different rotor with mixed magnets are shown in Figs. 2.21, 2.23 and 2.22. The rotor with the same geometric parameters is selected but, the magnetisation is different and permanent magnets are replaced by mixed magnets. The mixed magnets with the remanence distribution: $\mathbf{B}_{\mathrm{R}j}^{\mathrm{m}} = [0.7, 0.7, 1.2, 1.2, 1.2, 0.7, 0.7]$ T for a single magnet is taken.

The simulation results are shown in Fig. 2.23. The synchronous inductance is mostly the same because the stator model is the same, shown in Figs. 2.23a and 2.19a. Also, the armature reaction field is very similar in Figs. 2.22b and 2.20b. Because of different magnet magnetisation, the shape or the rotor magnetic field is changed, and the back-EMF changed too, shown in Figs. 2.23c and Fig. 2.22a. Meanwhile, the cogging torque peak value is reduced by half, and also the double frequency component occurs, as shown in Fig. 2.21a. The magnet flux linkage has some variation but is a little bit reduced with the segmented rotor configuration, as shown in Fig. 2.23b.

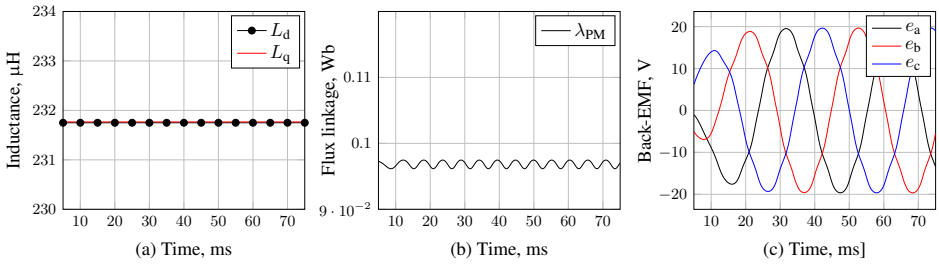

Fig. 2.23. Calculated parameters with surface-mounted segmented magnets: (a) the dq-axis inductances; (b) the flux linkage; and (c) the back-EMF

C. Simulation of Control System with Inset Permanent Magnets

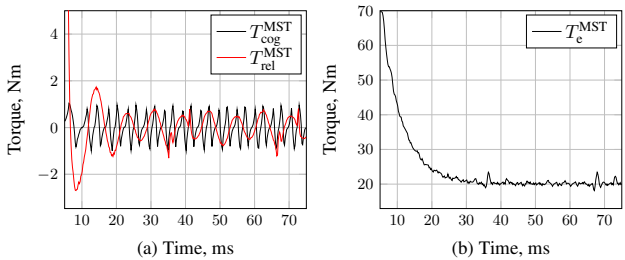

Fig. 2.24. Calculated torque components with inset permanent magnets: (a) the cogging and reluctance torque; and (b) the electrical torque

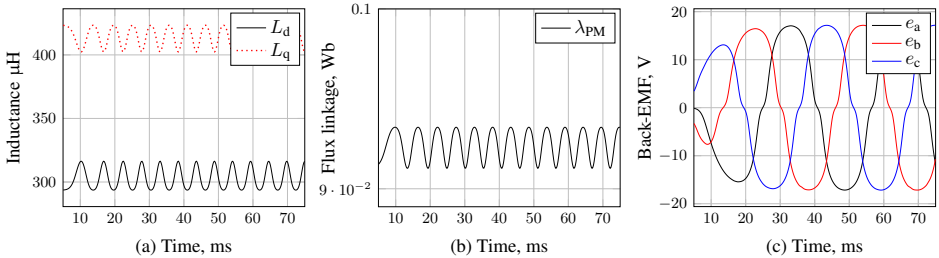

Fig. 2.25. Calculated parameters with inset permanent magnets: (a) the dq-axis inductances; (b) the flux linkage; and (c) the back-EMF

The simulation for PMSM with inset permanent magnets with the same field-oriented control setup is shown in Figs. 2.24, 2.25 and 2.26. The main geometrical parameters are the same as given in Table 2.7 as for previous configurations. The stator magnetic model is different and accounts for the rotor geometry as well. Fig. 2.25b shows synchronous

inductances are not equal, and also some fluctuations of magnitude can be seen as well. Because synchronous inductances are not equal, the reluctance torque is generated, as shown in Fig. 2.24a. The cogging torque frequency is also two times larger, while the peak reaches about 1 Nm. The magnet flux linkage also has additional harmonics, as can be seen in Fig. 2.25b.

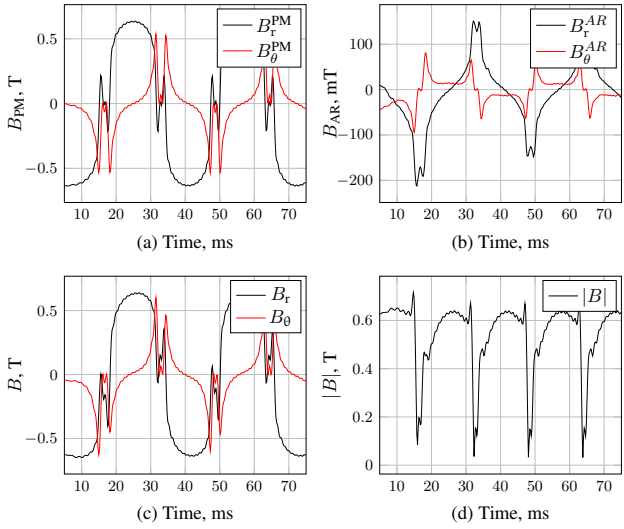

Fig. 2.26. Simulation results of the magnetic flux density with inset permanent magnets using the enhanced PMSM model: (a) the magnetic flux density of open-circuit; (b) the flux density of armature reaction; (c) the superposition of the open-circuit and armature reaction field; (d) the magnetic field magnitude

2.4.2. Simulation of Modified Extended Kalman Filter for Speed and Position Estimation

The programming language Matlab has been used to carry out simulations. The overall field-oriented control system and space vector pulse width modulation were simulated in order to make the simulation model compatible with additional experimental verification. The simulation was carried out for a variety of set point speed values in order to confirm the efficacy of the EKF algorithm. The simulation is used to examine how sensorless control performs at various motor speeds. The performance of the EKF is shown in Fig. 2.27, where the reference speed from $\omega_{\mathrm{e}}^{*} = 200$ rad/s to $\omega_{\mathrm{e}}^{*} = 400$ rad/s is set. Fig. 2.27a shows real and estimated rotor positions. The position error of EKF in radians is shown in Fig. 2.27c and is less than 2%. Fig. 2.27b shows the angular speed estimation performance under the step response. The angular speed error oscillates around zero, as shown in Fig. 2.27b.

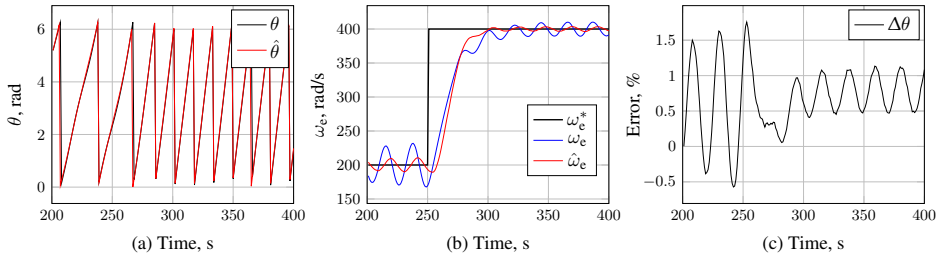

Fig. 2.27. EKF estimator performance test under the step response command from $\omega_e = 200$ rad/s to $\omega_e = 400$ rad/s: (a) the real and estimated rotor positions; (b) the angular speed; and (c) the estimated position error

2.4.3. Simulation of Phase-Locked Loop

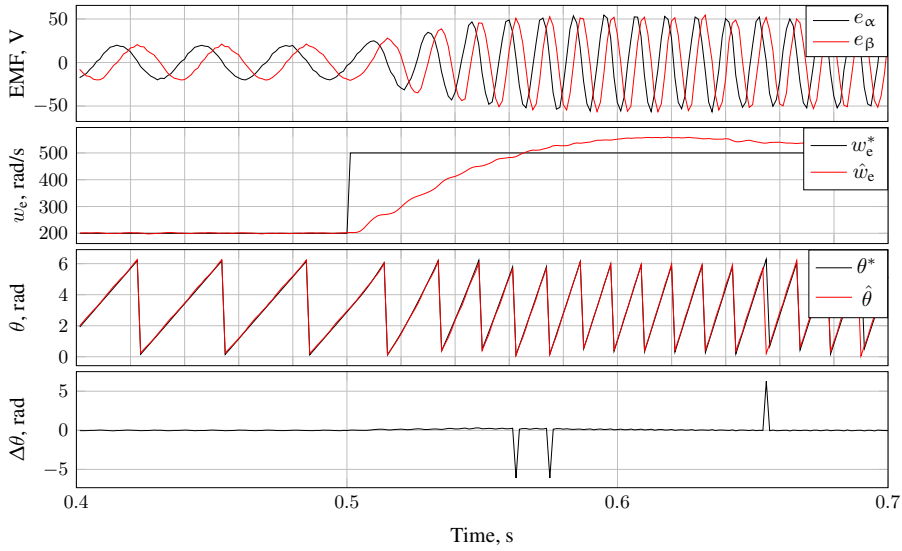

Fig. 2.28. Simulation results of PLL behaviour under the step response

The PLL estimator and the PMSM control system were simulated using the Matlab programming language. The phase voltages v_β and v_β are calculated knowing v_d and v_q voltages. Their v_d and v_q voltages are set-point voltages and are calculated by the PI current controller. The transient behaviour of the PLL estimator than the set-point of the electrical rotor speed (w^*) changes from 200 rad/s to 500 rad/s is shown in Fig. 2.28. As demonstrated, when the back-EMF voltages (e_α and e_β) increase, the rotor speed increases, too (Dilys, 2020). The electrical rotor speed set-point goes suddenly, and the real electrical rotor speed ($\hat{w}_e$) follows the command. The time to reach the set-point value depends on

the speed and current controller parameters. The electrical rotor speed and current settling times should not be too small compared to the PLL settling time (t_s), which is 0.1 s in this case. Based on Fig. 2.28, the PLL estimator is tracking the rotor position with a small rotor position error ($\Delta\theta$). The back-EMF voltages are then calculated using these voltages and currents. Also, the speed controller is stabilising the rotor speed to 200 rad/s and then to 500 rad/s. The stabilisation time depends on the settling time (Fig. 2.28).

2.5. Conclusions of the Second Chapter

1. The enhanced PMSM model considers the following parameters: electromagnetic torque, reluctance torque, cogging torque, synchronous inductances, back-EMF and flux linkage at the simulation stage, only knowing geometrical PMSM parameters and the rotor position.
2. The EKF calculation can be separated into two different procedures. One is the control procedure, and the other is the background procedure. The background procedure calculates the Kalman gain and all covariance matrices. The control procedure is executed on every PWM switching period, predicts the new state vector and updates the predicted state vector.
3. The Phase Locked Loop method based on the back-EMF voltage can track the PMSM rotor position and speed.

3

Experimental Research of Permanent Magnet Synchronous Motor Control Systems and Parameter Estimation

This chapter begins with an explanation of the magnetic flux density measurement system's design issues. Two magnetic flux density measurement systems are presented which were designed during the dissertation period. Then, magnetic flux measurement results in the PMSM are provided using the magnetic flux density measurement system to validate the enhanced PMSM model's accuracy. Next, a review of experimental systems for PMSM control design setup is provided, with hardware and software design explanation details. Using the experimental setup, the experimental research of the PMSM parameter estimation and rotor position estimation techniques is validated.

The research results were published in the author's publications (Balevicius et al., 2020; Dilys & Baskys, 2017; Dilys et al., 2021; Dilys & Stankevic, 2022; Stankevic et al., 2020; Stankevič et al., 2023;). The results were announced at international ICACE (London, 2022), Open Readings (Vilnius, 2022), "eStream" (Vilnius, 2017, 2022) and national "Science – the Future of Lithuania" (Vilnius, 2017, 2019), "FizTech" (Vilnius 2019, 2021) scientific conferences.

3.1. Implementation of Magnetic Flux Density Measurement System's Setup and Results

As already mentioned, the direct measurement of the magnetic field in PMSMs requires the use of special meters. This is due to the rather complex design of motors and processes, which take place in these motors. First, the direction of the magnetic field inside motors is varied in time and depends on the location of the sensor. Most known sensors for magnetic fields are sensitive to the direction of the magnetic field (pick-up coils, Hall

sensors and others). This means the direction must be known in advance, and the sensor has to be fixed perpendicular to the direction of the magnetic field, otherwise, the sensor will measure only the projection of the magnitude of the magnetic field onto the plane of the sensor. The additional problem is that during the operation of the motor the direction of the magnetic field changes. Of course, three sensors that are positioned in opposite directions can be used to solve this issue. However, the use of the three-dimensional design makes set-ups bulky with dimensions that are relatively large, making it difficult to measure locally or in very small volumes. The Center for Physical Sciences and Technology (CPST) already has a developed prototype of magnetic field sensors, for the measurement of strong magnetic field pulses. Films of polycrystalline $LaSrMnO_3$ manganites exhibiting colossal magnetoresistance are perspective materials for developing magnetic field sensors measuring the strong pulsed magnetic field. Moreover, these films are suitable for measuring the magnitude (CMR B-scalar sensor) of milliseconds range magnetic flux density in small (≈ 0.05 mm^3) volumes. The electrical and magnetic properties of these films can be tuned in broad ranges: changes in chemical composition and the deposition conditions can significantly alter the phase transition temperature, magnetoresistance (MR) and its anisotropy as well as the relaxation time. For measuring the magnetic field, the team CPST developed PC-controlled measuring system (Stankevič et al., 2014). The advantage of the magnetic field sensor in the measuring system is that it can measure the magnetic field in any direction. This makes it easier to install them in the measuring position because the sensor doesn't need to be exactly oriented to the magnetic field's direction. However, in order to assign a value of B to the sensor's magnetic field-induced resistance change R, a calibration is required because the temperature-dependent response of the sensor is not a linear function of the magnetic flux density B. The measurement system with these sensors was used to measure magnetic field diffusion in rails of an electromagnetic launcher (Stankevič et al., 2013) and in non-destructive pulsed magnets (Balevičius et al., 2013). However, this measurement system has a few drawbacks. One is that this system was designed to measure single-pulse magnetic fields.

The measurement principle of this system consisted of the following: the meter first has to measure the resistance of the sensor before the pulse; using this data, the ambient temperature is determined, and then calibration data is chosen, which convert the change in sensor resistance into a magnetic field flux. Such a measurement system is unacceptable when measuring the magnetic field in a motor. This is due to the reason that during the measurement the ambient temperature is not constant and is constantly changing. This means that it is necessary to measure the temperature independently. The second drawback of this measurement system is that the sensor was supplied with a constant voltage according to Winston's half-bridge scheme. In this case, the change in voltage on the sensor is not proportional to the change in resistance and depends on the ratio of the resistance of the sensor and the resistor connected in series with it. Three types of meters were developed in order to overcome these drawbacks and adapt sensors to measure the flux of the magnetic field in motors: the hand-held multifunction magnetic field meter with a colour touch-screen for waveform show and two other modules, which are controlled by PC. By employing a system that compensates for electromotive force-caused parasitic voltage in the sensor wires, one of these modules is able to measure high-amplitude pulsed magnetic fields with pulse durations in the hundreds of microseconds range, while the other module is able to measure pulses with durations in the microsecond range.

3.1.1. Structure of the Hand-Held Magnetic Field Meter

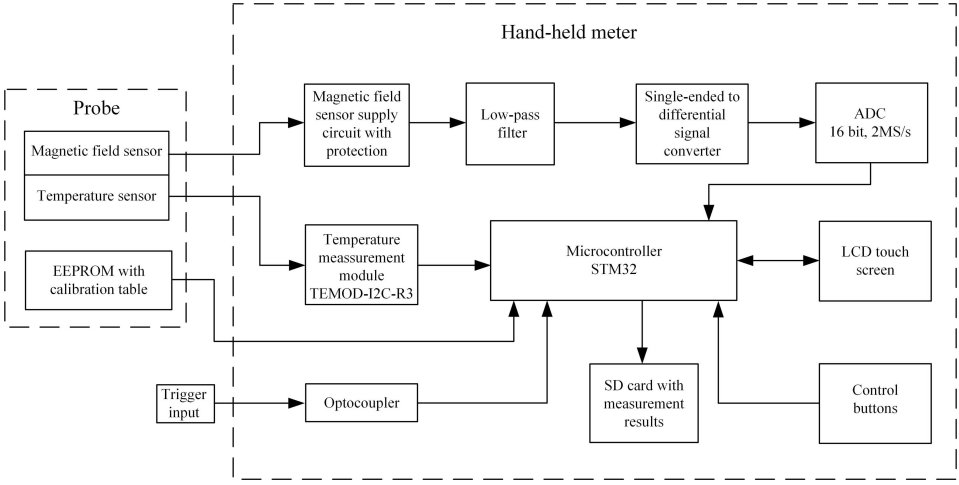

Fig. 3.1. Block diagram of the hand-held B-scalar magnetic field meter (Balevicius et al., 2020)

The new hand-held magnetic field meter has been developed for the measurement of magnetic flux density in the PMSM air gap (Balevicius et al., 2020). It enables the measurement of the magnitude of pulsed, alternating, or permanent magnetic flux density in a range from 0.06 up to 10 T. A block diagram of the hand-held magnetic field meter is presented in Fig. 3.1. There are two parts to it: the probe and the hand-held meter. The magnetic field and temperature sensors that make up the probe are connected to the handheld meter by a cable made of two pairs of bifilarly twisted wires and a connector that contains an EEPROM chip. The temperature is measured with the standard resistive temperature sensor Pt1000. A CMR B-scalar sensor based on nanostructured manganite films is utilised for measuring the magnetic field magnitude. The EEPROM chip contains the calibration field sensor's adjustment information, which are utilised for the change of the reaction voltage signal to magnetic field values. A supply circuit for the magnetic field sensor is included in the handheld meter based on a precise current source ($I = 200$ μA) with a low-pass filter and overvoltage protection circuit for the suppression of noise signals. The obtained signal is transformed into a differential signal by the single-ended to the differential signal converter. A precise 16 bit-25 Msps ADC is used to change a differential analogue signal into a digital one. The temperature estimation block TEMOD-I2C-R333 is utilised for the change of the temperature sensor's resistance to voltage. The obtained data of the magnetic flux density are displayed on a TFT LCD screen measuring 4.3-inches as a graph of B vs time.

In addition, it is utilised for controlling the device's operation and setting the parameters of the magnetic field meter. The measured magnetic flux density curves' data tables are saved to an SD memory card. The two control buttons on the handheld meter allow for

both the start and stop of the measurement as well as the saving of the measured curves to the SD card. The ARM architecture microcontroller STM32 is the main part of the device. It processes the data from the temperature and magnetic field sensors and uses the calibration table data from the EEPROM chip to figure out the values of the magnetic flux density. There is some dispersion in the parameters of the various magnetic field sensors. As a result, the implementation of distinct calibration tables for each magnetic field sensor makes it possible to guarantee the highest level of measurement precision. Furthermore, the microcontroller controls the activity of the hand-held magnetic field meter what's more, takes into consideration the settings of the necessary boundaries. The hand-held meter has a circuit that feeds the trigger pulse through the BNC connector so that external pulse sources can be used to trigger the device. The optocoupler keeps this trigger input galvanically isolated from the microcontroller.

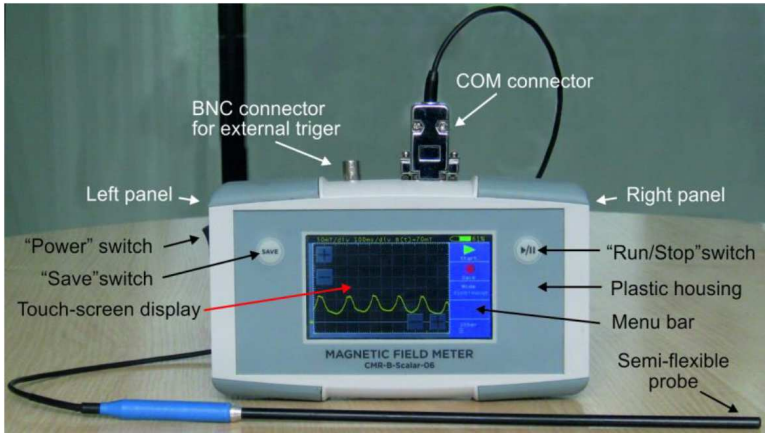

Fig. 3.2. Outside view of the hand-held B-scalar-06 magnetic field meter with a colour touch screen for waveform display. The hand-held semi-flexible probe is connected to the device (Balevicius et al., 2020)

The following is how the device works: the current of the precise current source led through the field sensor permits obtaining a voltage reaction signal corresponding to the sensor's impedance change due to CMR effect. The voltage signal is converted using a precise ADC converter after passing through the low-pass filter. The computerized signal given by the microcontroller's digital inputs and outputs are connected to the LCD touch screen, and control buttons. The SD card stores the recalculated measurement data that are displayed on the LCD touch screen.

The external view of the hand-held meter's design is shown in Fig. 3.2. Inside a housing made of plastic, the meter is mounted. The device's front panel has a touch-screen display, a switch for run and stop operation, and a save switch. A COM connector connects the magnetic field probe to the housing's upper panel, and a BNC connector connects the housing to the trigger pulse transmission cable. The left side board of the lodging contains a power switch for the on and off exchanging of the battery, a small-scale USB Connector for charging the battery and two LEDs for showing the action of the battery charging

process. The right side board of the lodging has a connector for the smaller than normal SD card.

3.1.2. Design of Scalar Probe for Hand-Held Meter

The structure of the hand-held magnetic field meter's probe is presented shown in Fig. 3.3. As already mentioned, the probe consists of a B-scalar sensor made from two thin nanostructured polycrystalline $LaSrMnO_3$ films and the resistive temperature sensor Pt1000. The magnetic field sensor's design was constructed according to the patent two $LaSrMnO_3$ films (sensor I and sensor II) (Fig. 3.3) exhibiting different resistivity versus temperature dependencies were connected in series. This plan diminishes the all-out magnetoresistance what's more, zero field opposition conditions on temperature and builds the aversion to the magnetic field at room and higher temperatures. Additionally, the B-scalar sensor is mounted close to the resistive temperature sensor Pt1000. This allows for the measurement of the temperature in the vicinity of the magnetic field sensors. The active area of a single magnetic field sensor (manganite film) is $400 \times 50 \times 0.4$ μm^3. The distance between the $LaSrMnO_3$ films is about 400 μm. Thus, this design provides an excellent measurement of the local magnetic fields in small ($\sim 10^{-3}$ mm^3) volumes.

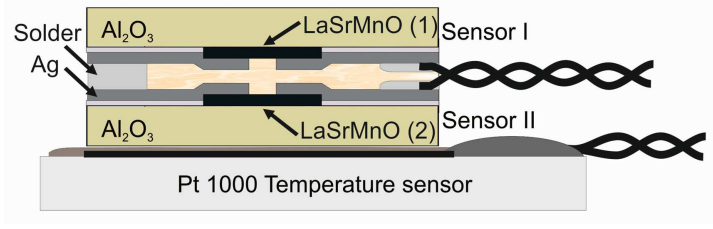

Fig. 3.3. Structure of the B-scalar magnetic field meter probe (Balevicius et al., 2020)

The CMR B-scalar probes can be made in two configurations: a hand-held solid probe with a cable that can bend (Fig. 3.2). and a flexible probe which usually is mountable. In the first configuration, the probe is equipped with a hard fibreglass tube with a handle, with an outside diameter of 6 mm and a length of 300 mm. In the second configuration, the probe is made of a flexible cable with an outside diameter of 3 ± 0.5 mm. The active elements (sensors) are positioned in the centre of the plastic tube or cable at a distance of 2 mm from the tips of these probes. The cable is made of two pairs of bifilarly twisted wires with braid shielding. Both probes come with a standard 1 m length cable, which can be customised up to 2 m. The connection of the probes to the meter is made through a 9-pin metallic connector. The calibration data for these probes are stored in the EPROM chip positioned inside this connector, allowing for fast and simple changing of the probe. The meter configures itself automatically each time a probe is connected. Our tests have demonstrated that a cable length of one meter is sufficient to keep the hand-held meter safe from the measured area and prevent the magnetic field from entering the electronics. For example, when the magnetic flux density in the middle of a coil with a pulsed field coil is

10 T, the magnetic flux density is only $\sim 10^{-7}$ T in the area at a distance of 1 m from it. For other applications, the cable can be lengthened up to 2 m.

For the testing of the device, a special short-duration magnetic field pulse generator was used (Balevicius et al., 2020). The testing results have shown that this compact hand-held multifunction magnetic field meter with a B-scalar probe for the measurement of the magnitude of magnetic fields of unknown directions can be successfully used not only for the measurement of the magnetic field in the motor but in the different field of industry and science. It combines the advantages of an oscilloscope with the functionality of a digital magnetometer. This device with a graphical colour touch screen is able to display a magnetic field waveform $B(t)$ for DC, AC, and pulse mode measurements without the use of an external oscilloscope or another analogue graphing device. It was obtained that the average error due to the MR anisotropy effect of the B-scalar manganite sensors in the temperature range from 10 °C to 50 °C depends on the magnetic field value and does not exceed $\pm 2\%$ at B $>$ 1 T.

3.1.3. Structure of the Scalar Magnetic Field Measurement Module

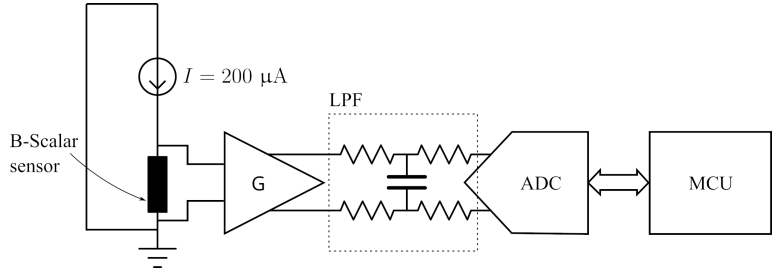

Fig. 3.4. Block diagram of measurement module using CMR B-scalar sensor

For the measurement of the magnetic field in a hard condition, the measurement module with a screened electric circuit controlled by a PC was developed. The operating principle of this module is similar to the hand-held meter described above. The module used for data acquisition and recording was an electronic device specially protected against harsh electromagnetic conditions by an inner 4 mm thick steel box and an external 1.5 mm thick aluminum box. The analogue signal of the sensor in this module was digitised using a 16-bit analogue-digital converter with a sampling rate of 25 MHz. The high-pulsed magnetic field measurement module, consisting of the CMR B-scalar sensor and the electronic module, was able to measure the magnetic field in frequency ranges from DC to 100 kHz with a resolution of the magnetic flux value of not less than 10 mT. This was sufficient to achieve good time resolution during the measurement of the magnetic pulses with durations of several hundred microseconds. The measured signal was processed and recorded in the memory of the module. Then, the recorded signal was transmitted to a personal computer by means of a fibre optic link. CMR B-scalar sensor is supplied by the circuit

based on a precise current source ($I = 200/400$ μA) with over-voltage protection and a low-pass filter for the suppression of noise signals (Fig. 3.4).

The single-ended to differential signal converter transforms the obtained signal into a differential signal. A precise 16-bit and alternatively fast 25 Msps ADC is employed for the conversion of the differential analogue signal to a digital one. The temperature measurement block TEMOD-I2C-R333 is used for the conversion of the Pt1000 temperature sensor's resistance to voltage and after that, for the conversion of the voltage signal to the digital I2C standard signal. The main component of the device is the ARM architecture NXP LPC54606 microcontroller for PC meters. The microcontroller processes the data received from the magnetic field and temperature. Unlike the hand-held meter, which stores the calibration table in an external EEPROM chip located in the sensor connector, in this design, these calibration tables are stored in the module itself in FLASH memory. There is some dispersion in the parameters of the various magnetic field sensors. Subsequently, the presentation of individual alignment tables for each magnetic field sensor takes into account the assurance of maximal estimation exactness. The ability to connect multiple devices for a single measurement and the faster ADC sample speed are the main benefits of this PC-controlled module.

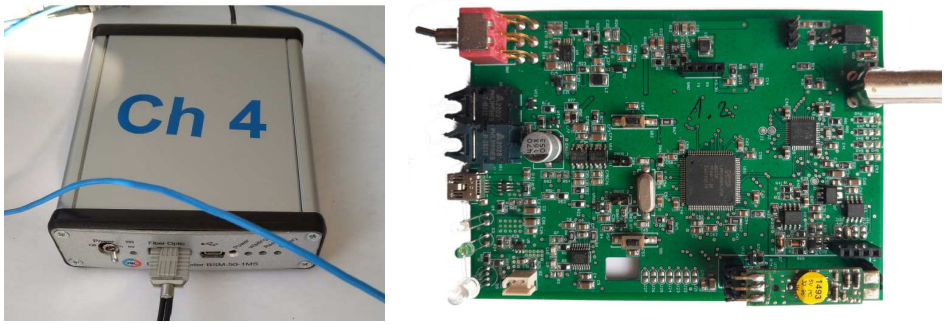

(a) (b)

Fig. 3.5. Pictures of the B-scalar magnetic field measurement module (a) and the module board (b)

Moreover, the module has more precise trigger capabilities. The external view of the design of the magnetic field measurement module and board is shown in Fig. 3.5. The module board is mounted inside a metal housing working as a shield against electromagnetic noises. For communication with the magnetic field measurement module, the PC software has been designed. The PC software was written using Visual Studio 2010 in the C-Sharp programming language.

The program's main task is to visualise signals received from the B-scalar meter. The PC-meter software can send settings and write new calibration table data to the B-scalar meter.Additionally, the PC-meter software enables configuring the B-scalar meter trigger level and type.Moreover, the PC-meter software has embedded the newest firmware version and can update the B-scalar meter firmware too. The new firmware is downloaded to the B-scalar PC-meter via the same USB port as the data and main window. The firmware is

encrypted with the AES-256 algorithm for security purposes. Moreover, the device can use the B-scalar probe with or without a temperature sensor. The created device is easy to use and can be used not only for measuring the magnetic field dynamics inside of the motor but for other purposes as well. For example, it was successfully used during an experiment on Magnetic Pulse Welding (Stankevic et al., 2020).

3.1.4. Measurement System for Short-Pulsed Magnetic Fields

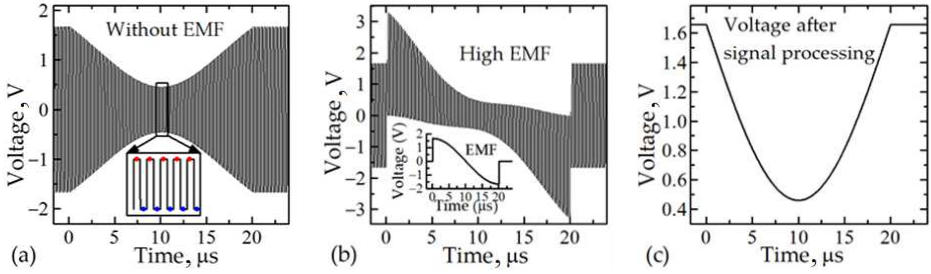

Fig. 3.6. Voltage across the CMR sensor that is powered by pulsed voltage: (a) without the back-EMF; (b) with the EMF; (c) after signal processing. Inset: in (a) points indicate time instants at which the ADC reads positive and negative voltage values; in (b) back-EMF induced in the sensor and its wires (Stankevič et al., 2023)

The high electromotive force signal that appears in the transmission line of the sensor as a result of the rapidly changing magnetic field is another issue that needs to be resolved during the operation of the aforementioned meters for measuring high-frequency magnetic fields. A twisted pair cable, which was utilised in all sensors, can somewhat tackle this issue. Therefore, a magnetic field meter that can measure high-pulsed magnetic fields with pulse durations of several microseconds is proposed and developed as a result of this. The core of the answer to this issue is utilising the bipolar-pulse supply of the B-scalar magnetic field sensor. The LTspice simulation was initially used. Fig. 3.6 displays the results of the simulated voltage across the CMR sensor when it was subjected to a 20 $upmu$s long magnetic field pulse at a frequency of 5 MHz. Fig. 3.6a presents the result when the back-EMF in there is no transmission line. As may be obvious, because of the negative magnetoresistance of manganite film the positive and negative pulsed voltages are diminishing evenly during the applied magnetic field pulsed. This change is influenced by the electromotive force, which is proportional to the time differential of the magnetic field, in the second scenario (Fig. 3.6b). After these voltages have been processed in accordance with equation $V = 0.5\,[(V^+ + e) - (V^- + e)]$, the e is eliminated, and only the sensor's resistance change in a magnetic field results in a voltage change (Fig. 3.6c). In this equation, V^+ and V^- are the adjacent voltages of two pulses when the sensor receives positive and negative voltages, respectively (in the inset in Fig. 3.6a. The new proposed measurement system is depicted in a block diagram in Fig. 3.7. The CMR sensor ($\mathrm{R_s}$), connected with two ballast resistors ($\mathrm{R_bal}$) is supplied by a supply with a bipolar

pulse. The magnetic field generator has a sensor in the middle of a coil Fig. 3.8. shows a more definite circuit of the power supply and recording framework. It has an analogue-to-digital converter with a high-frequency differential and a high-frequency bipolar-pulse power generator. The CMR sensor's primary power source is a bipolar-pulse generator with an integral circuit based on RS485 that produces rectangular-shaped pulses at up to 12.5 MHz. The LTC2203, a 16-bit analogue-to-digital converter that records the sensor's negative and positive voltages from peak to peak at a sampling rate of up to 25 Msps, is synchronized with the pulse generator. The ADC's output data are processed and recorded by a microprocessor (LPC54606J256BD100E) in accordance with the equation (Fig. 3.6a). The back-EMF is therefore removed from the measured signal, and only the useful voltage change brought about by the change in the magnetic field is measured.

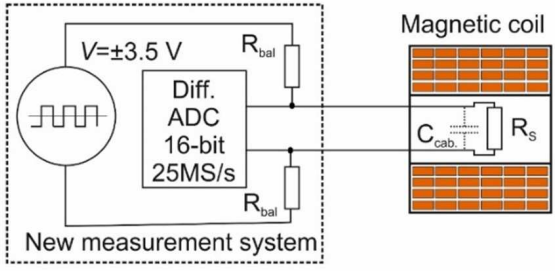

Fig. 3.7. Block graph of the new estimation framework and magnetic curl utilised for testing and alignment of the sensor (Stankevič et al., 2023)

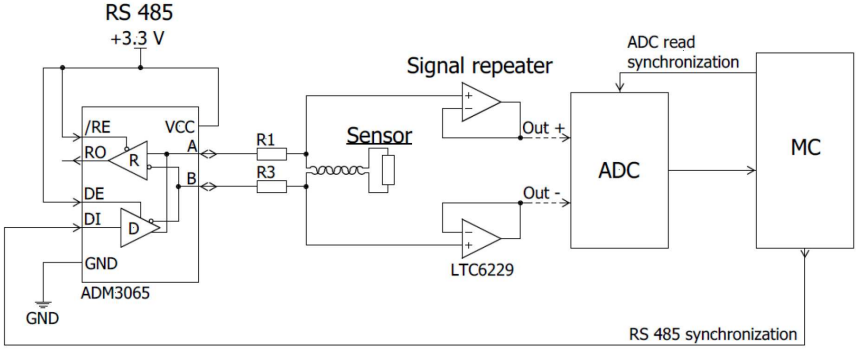

Fig. 3.8. The digitalisation of the output signal and the sensor supply circuit diagram (Stankevič et al., 2023)

The proposed new magnetic field meter is an electronic device for estimations of short-pulsed magnetic fields. Electronic circuits are shielded from electromagnetic interference (EMI) by the meter's casing, which consists of an internal steel box that is 4 mm thick and an external aluminum box that is 1.5 mm thick. The B-scalar meter's block dia-

gram can be found in Fig. 3.9. The electronic circuits are powered by a 3.6 V lithium-ion rechargeable battery. The inward power supply guarantees that the device can work without being associated with any outer power sources. Refusing to use the signal conditioning circuits was made possible by using a high-resolution ADC, which reduced the number of analogue components needed. The voltage change is converted into the magnetic field and stored after the measured signal is processed. In addition to being influenced by the temperature of the surrounding environment, the magnetic flux density B has no linear effect on the sensor's response. To assign a value of B to the sensor's magnetic field induced resistance change (ΔR) calibration of the sensors is required. The same measurement module houses the fabricated sensors' calibration tables, to which each sensor is assigned a serial number.

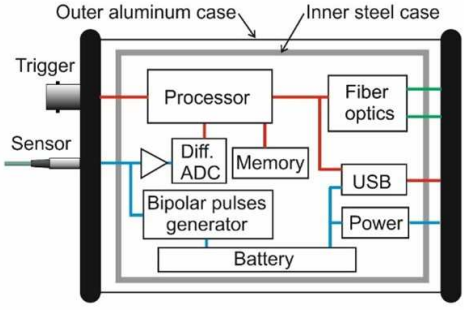

Fig. 3.9. Block diagram of the fast B-scalar meter (Stankevič et al., 2023)

Short-pulsed magnetic field generators were used to test the newly developed short magnetic field measurement system. In more detail, the boundaries of the new meter and experimental outcomes are portrayed in the article (Stankevic et al., 2023). The obtained results allow for concluding that a novel pulsed magnetic field measurement system with a fast measurement module and a B-scalar sensor based on a thin manganite film is capable of measuring high magnitude (up to 25 T) and short-pulsed magnetic fields. A local field measurement is guaranteed by the system as the active volume of the sensor is $400 \times 50 \times 0.4 \mu\mathrm{m}^3$. In addition, a casing made of a thick steel box inside and a thick aluminum box outside was used to shield the electronic circuit from strong electromagnetic interference.

3.2. Measurement of Magnetic Flux Density

The measurement of the magnetic flux density of two, same-design motors of nominal 800 W power was performed. First, the motors were disassembled by separating the rotor from the stator. The air gap between the stator and rotor of selected motors is only 0.5 mm, and mounting of sensors in the air gap was impossible because of the size of the sensor. The sensors were mounted into the slot gap of the stator as close as possible to air gap (Fig. 3.10). After the sensors were embedded, the rotor was placed back into the stator.

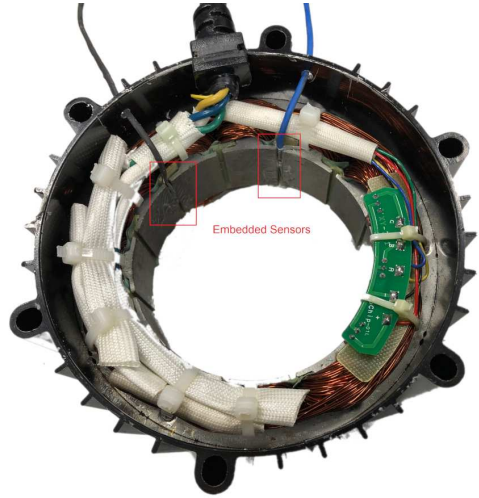

Fig. 3.10. Embedded CMR B-scalar sensors to motor stator

3.2.1. Measurement Results of Magnetic Flux Density Magnitude Using B-Scalar Meter

The magnetic flux density is measured for two identical motors (the same model) but physically different PMSMs. All measurements were made with the created B-scalar meter and using the meter module controlled by a PC. At the frequency and magnitude of the magnetic field typical for the PMSM, both meters are able to measure the magnetic field in ± 10 mT accuracy.

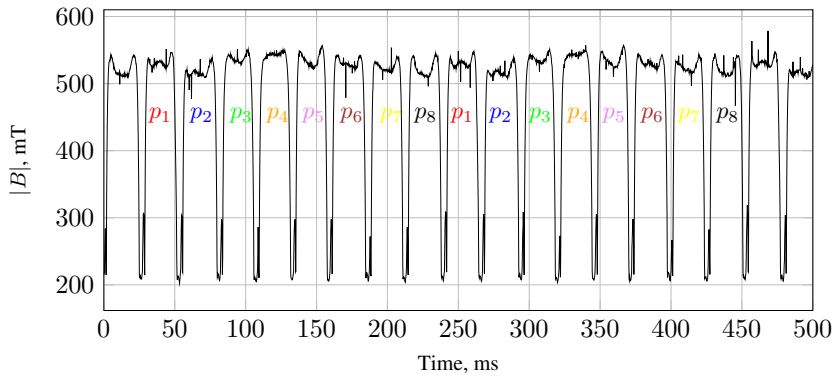

Fig. 3.11. Magnetic flux density magnitude waveforms of the first motor where p_{i} stands for a unique pole number

The investigated PMSM has eight poles (four pole pairs). The armature reaction magnetic flux can be neglected because the motor has been started and running without any mechanical load being put on its shaft. The PMSM magnetic flux density was measured with a CMR B-scalar sensor; then, the rotor was rotated at a constant speed. The measurement results are shown in Fig. 3.11. Fig. 3.11 shows that eight different shape pulses (each for an appropriate pole) were generated during one full revolution of the PMSM rotor. The unique pole number is marked p_i (the first pole number is marked p_1). Fig. 3.11 shows how the p_1 pole shape repeats after a revolution cycle. The same tendency goes for other poles as well. Because the PMSM has eight poles, there are eight different shapes, one for each pole, as shown in Fig. 3.11. The difference betweenthe two adjacent pole shapes is not due to the ideal manufacturing process or due to exploitation. This detailed magnetic flux density measurement allows for determining the quality of the magnets and PMSM rotor type as well.

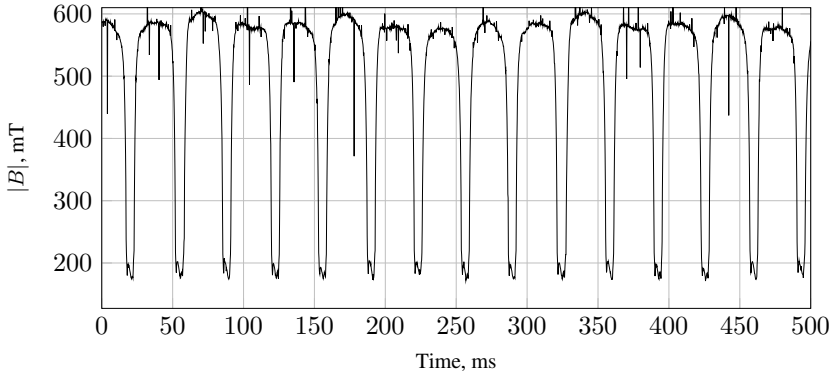

Fig. 3.12. Magnetic flux density magnitude waveforms of the second motor

The measurement results of the magnetic flux density of the second are physically different, but the same model of PMSM using the same the same B-scalar sensor is shown in Fig. 3.12. As in the previous experiment, eight different poles can be seen for one repetition of the rotor. Comparing Figs. 3.12 and 3.11 shows that the first motor's peaks have a fold; meanwhile, the second motor's peaks have a bend-like shape. This allows for a conclusion that the manufacture or exploitation process has a big influence on the magnetic flux density distribution. However, from a graphical view of the analysis, it is practically impossible to determine the exact the PMSM's magnetisation type because of the chaotic shape distribution of the magnetic flux density for different poles. However, by analysing the shape, the closest magnetisation type could be selected.

3.2.2. Comparison of the Magnetic Flux Density Measurement with the Model

An enhanced PMSM model is compared with the ideal PMSM model and with a real PMSM in regard to the magnetic flux density distribution in the air gap region. For an en-

hanced PMSM model simulation to be as close as possible to real PMSM, the assumption is made that the permanent PMSM magnets are magnetised in parallel. These assumptions were made by analysing the experimental measurement of the real PMSM magnetic flux density in the air gap. Additionally, to replicate the measurement of the real PMSM, the enhanced PMSM model's magnetic flux density simulation was recorded at the air gap region near the stator core. Meanwhile, the ideal PMSM model magnetic flux density distribution in the air gap was obtained by making the following assumptions: the stator is slotless, and the rotor permanent magnets are optimally magnetised and take all of the surrounding space. This assumption makes the ideal PMSM flux density to be sinusoidal. The absolute value of the ideal PMSM magnet flux density is shown in Fig. 3.13, in a green line. All results of the measurement and simulation are shown in Fig. 3.13, which shows a close magnetic flux density relation of the simulated enhanced PMSM model compared to the measure of the real PMSM. The total integral of the magnetic flux density magnitude of the measured and simulated coincidence is 97% (the difference of 3%), and it is a good indicator of a properly designed enhanced PMSM model and accurate measurement. The difference between the magnetic flux density magnitude integral of the enhanced PMSM model and the ideal PMSM model is 20%. The enhanced PMSM model has a large benefit compared to the ideal PMSM model because it evaluates a more accurate magnetic field distribution and is very close to the real PMSM.

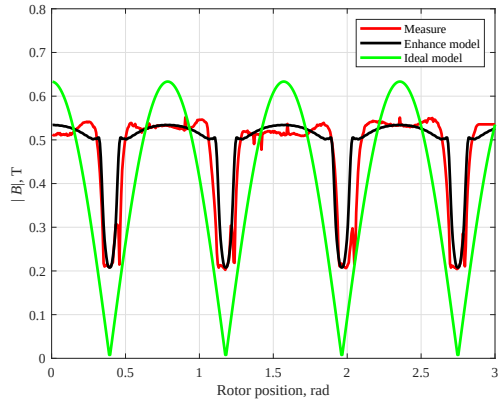

Fig. 3.13. Measured and simulated magnetic flux density waveforms

3.3. Hardware Setup for Motor Control

The implemented drive control structure with a speed controller is shown in Fig. 3.14. The vector control method with sensorless speed and position estimation is implemented. A vector control method with i_{d} set to zero is used. For the position and speed estimation, the modified extended Kalman filter with reduced execution time is implemented. The

command voltage vector is realised by the space vector pulse width modulation (SVPWM).

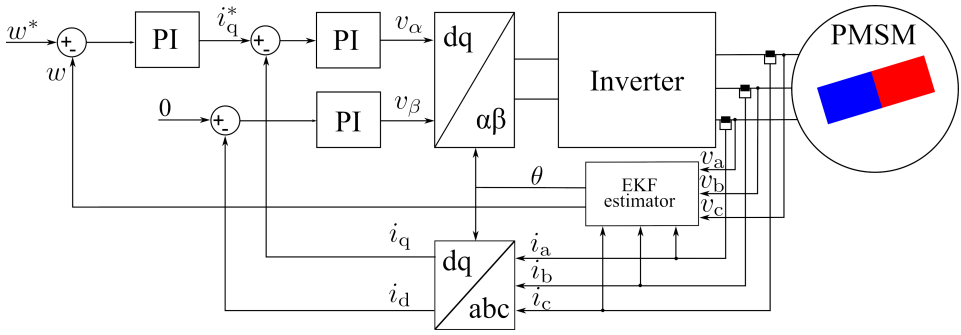

Fig. 3.14. Block diagram of the implemented control algorithm

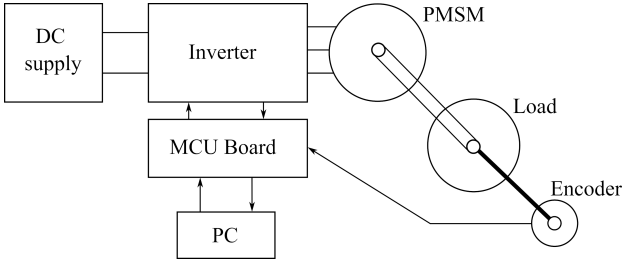

Fig. 3.15. Experimental system configuration

The basic structure of the laboratory setup is depicted in Fig. 3.15. The photography of the experimental system is shown in Fig. 3.16. The setup consists of a PMSM and a brushed DC motor as a load. The PMSM is fed by the frequency inverter controlled directly by the LPC1549 board.

The LPC1549 board is plugged into the self-made inverter (Fig. 3.17). The inverter is fed by the DC laboratory supply. Fig. 3.18 illustrates a block diagram of the inverter drive used in this dissertation. The transistors used for the inverter are MOSFET transistors. MOSFET transistors were chosen due to the superior switching speed compared to their counterparts and the low drop voltage. The motor currents (i_a, i_b, i_c) are measured using three current shunt resistors connected to the ground as shown in Fig. 3.18. Because shunt resistors are connected to the ground, the ADC sample is valid, only then are low transistors on. An important hardware configuration choice is the number of shunt resistors to use. This number is ultimately used by the Clarke transform to convert from a three-phase system to a two-phase system. Three shunt resistors are used if all the phases have a shunt resistor from the bottom transistor to the ground, as shown in Fig. 3.18.

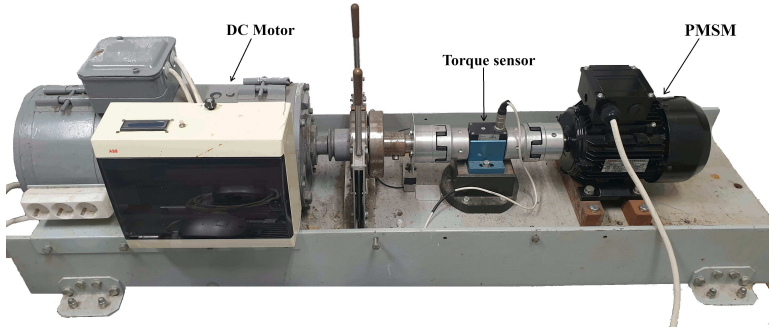

Fig. 3.16. Photography of the experimental system

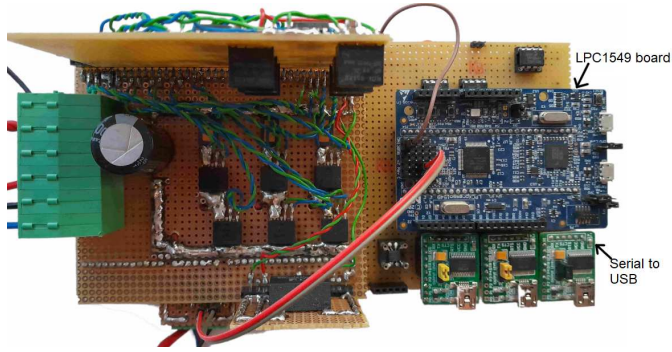

Fig. 3.17. Inverter view for the PMSM control

Motor phase voltages (v_a, v_b, v_c) are measured directly from the motor phases using a simple RC low-pass filter. The RC filter gain is selected for the maximum motor voltage to scale phase voltages not to exceed the ADC reference level. The cut-off frequency of 4.7 kHz is selected to filter the switching frequency harmonics.

An LPC1549 board performs all measurements in real-time and transmits data to a personal computer. Sensors sampled the phase current, while the control algorithm calculated the phase voltages. A photoelectric incremental rotary encoder's signal was compared to the EKF's estimate of the rotor's position.

For the execution of the vector control in a drive framework, a NXP LPC1549 microcontroller was utilised. The 32-bit ARM Cortex M3-based LPC1549 microcontroller operates at a frequency of up to 72 MHz. It is a microcontroller that is inexpensive and uses very little power. It has four voltage comparators, two ADCs, and a PWM/timer subsystem with four multi-purpose state configurable timers. Since the LPC1549 microcontroller does not support operations in floating point, all calculations were performed on variables of the integer type. The implementation's variables are 16-bit fixed-point variables with 32-bit long words as their data type. The IAR compiler was used for the C language implementation and code compilation.

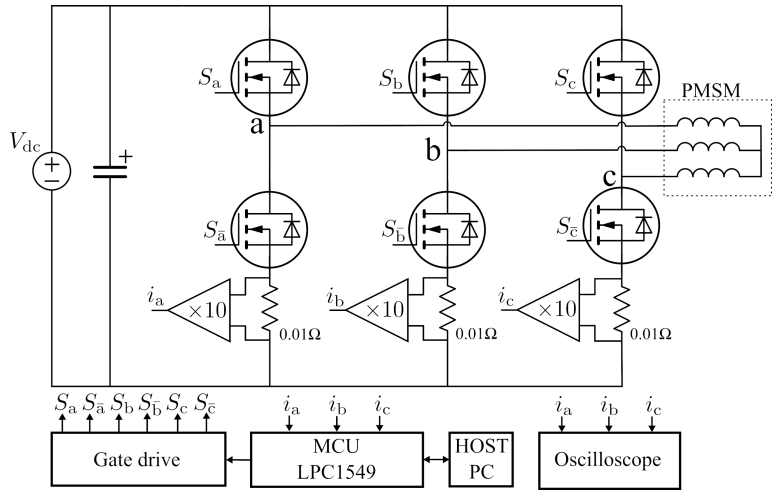

Fig. 3.18. Schematic of the inverter

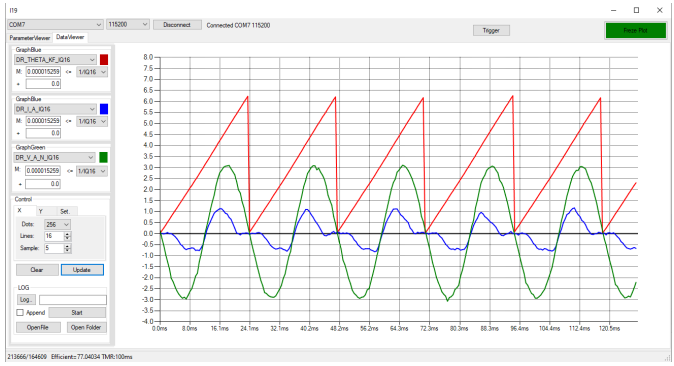

Fig. 3.19. PC program main window for data acquisition

For data transmission from the inverter to a PC, USB converters (MIKROE-1203) were used. PC software with Visual Studio 2019 C-Sharp programming language was created. The main program window for software is shown in Fig. 3.19. This software enables a user to send all required settings to the inverter, like reference speed and updated motor control parameters. The main benefit of PC software is to sample measured values from the inverter and visualise it on PC screen.

The data from the inverter are sent in blocks to make data not chopped, and up to three signals at the same time can be visualised. Additionally, the sampled data can be saved to a PC hard disk as text files.

3.4. Control and Estimation Results

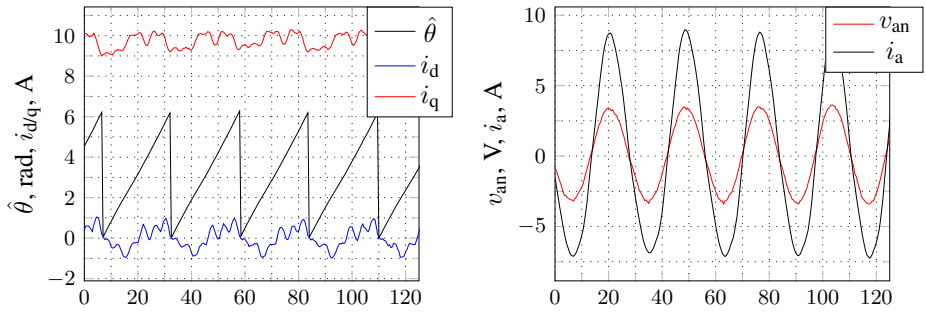

Fig. 3.20. Vector control results: (a) the dq-axis currents and the estimated rotor position ($\hat{\theta}$); (b) the a-axis voltage (v_{an}) and current (i_a)

In rotating reference for the surface-mounted PMSM, the vector control goal is to control i_d currents to zero, and the i_q current is responsible for electrical torque. Fig. 3.20a shows the i_d and i_q current waveform under load test, where the i_d current reference point is set to zero. In the rotating reference frame, the a-phase voltage and current are shown in Fig. 3.20b. Fig. 3.20b) which shows the phase voltage and current like sine waves. In Fig. 3.20b the phase voltage and current cross zero at the same point, which means that the power factor is close to one.

3.4.1. Stator Inductance and Resistance Estimation at Standstill

During the whole assessment time, just three short-time rectangular voltage pulses are applied into motor windings. Inactive time separates active vectors from one another, and the phase windings are not energized during the inactive time. The all-phase windings could be connected to the ground or not connected at all during inactivity. Three active space vector pulse width modulation vectors $v_1(100)$, $v_3(010)$ and $v_5(001)$ are used in sequence as shown in Fig. 1.5 (Dilys & Baskys, 2017). The diagram of the phase current distribution profiles appears in Fig. 3.21. Stationary three-phase currents i_a, i_b and i_c are measured with sensors. And two-phase dynamic currents i_d and i_q are calculated from stationary phase currents following estimation of the rotor's position. Three-phase stationary currents i_a, i_b and i_c are used to estimate the rotor's position.

The proposed method is depicted graphically in Fig. 3.22. Where the active vector goes in sequence v_i is v_1, v_3 or v_5, and the sequence never changes.

This inverter makes use of MOSFETs (metal oxide semiconductor field effect transistors) with N-channels because of their high speed and low voltage drop. All of the necessary control processing is done by the microcontroller LPC1549. The three shunt current measurement method is utilised for current measurement. The current of the mo-

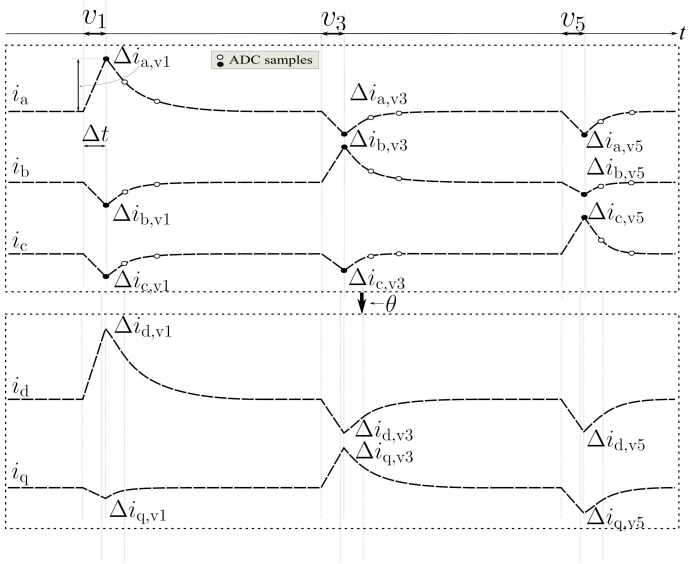

Fig. 3.21. Current distribution profiles (Dilys & Stankevic, 2022)

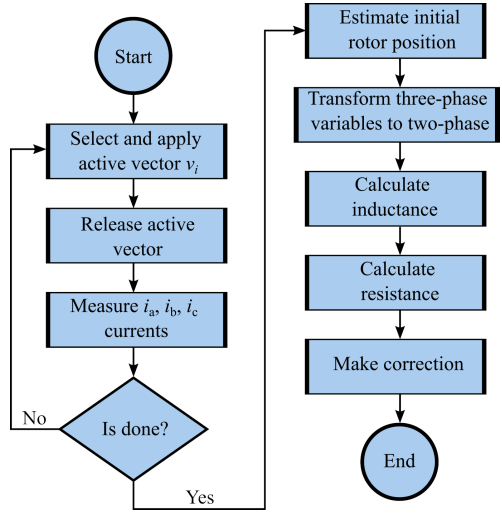

Fig. 3.22. Algorithm diagram of the proposed method (Dilys & Stankevic, 2022)

tor phase can only be measured when the low transistor is on due to the type of current shunt connection. The signal from the phase currents is amplified ten times before being sampled by the ADC of the microcontroller LPC1549 with a resolution of 12 bits. The inverter is supplied by a 24 V laboratory DC voltage power source. Two different perma-

Table 3.1. Rated power and parameters of the two motors used in the tests

Parameter		PMSM-1	PMSM-2
Power supply voltage	V_{dc}	24	24, V
Nominal power	P_{n}	500	78, W
*Phase resistance	R_s	0.06	0.38, Ω
*Inductance d-axis	L_{d}	140	145, μH
*Inductance q-axis	L_{q}	210	180, μH
Pole pair number	p	6	4

*_Note_. Parameters are measured using an LCR meter.

nent magnet-type brushless DC motors with specifications given in Table 3.1 were used during the experimental test. A particular gate switching modulation is implemented on LPC1549 microcontroller and displayed in Fig. 3.23. The hardware uses the switching pattern, which means that phase currents can only be measured when low-side transistors are on. The gate switching period T_{s} is taken to be large (30 ms), this enables decay energy after excitation. The voltage pulse time $\Delta t = 20$ μs is selected for all vectors v_1, v_3 and v_5. The selected dead-time T_{d} is 700 ns for the inverter. The ADC sampling for peak currents begins after the delay time T_{w}, after all low-side switches ($S_{\bar{a}}$, $S_{\bar{b}}$, $S_{\bar{c}}$) are on. The delay time T_{w} is added to suppress noises due to switching, and for the inverter $T_{\text{w}} = 4$ μs is taken. The sample time delay t_{d} accounts for both the ADC delay time and the dead-time, and is given as $t_{\text{d}} = T_{\text{d}} + T_{\text{w}}$. Experiments were carried out on two different motors using the parameters given in Table 3.1. During the supply vector v_1 , the currents build up for PMSM-1 motor is shown in Fig. 3.24. Solely for illustrational purposes, the rotor position is set to zero and the estimated rotor position $\hat{\theta} = -0.05$ rad. The transformed phase currents into a rotating reference frame are displayed in Fig. 3.24b, where the i_{q} phase current disappears when the rotor is in the zero position. The phase current i_{d} increases linearly from zero to its maximum value as shown in Fig. 3.24b. The small current spikes at times 80 and 100 μs are switching noises and take approximately 3 μs (Dilys & Stankevic, 2022).

The phase currents during the whole estimation period for PMSM-1 are shown in Fig. 3.25c and Fig. 3.25d.

The rotor position was set arbitrarily to any position and estimated is $\hat{\theta} = 1.23$ rad. Without a correction step, the estimated dq-axis inductances are $\hat{L}_{\text{d}} = 146$ μH and $\hat{L}_{\text{q}} = 215$ μH. respectively. The estimated resistance $\hat{R}_s = 0.057\ \Omega$ without applying the correction step. The final estimated inductance after the correction step are $\hat{L}_{\text{d}}^{\text{c}} = 145$ μH, $\hat{L}_{\text{q}}^{\text{c}} = 215$ μH and $\hat{R}_s^{\text{c}} = 0.057\ \Omega$ (Dilys & Stankevic, 2022).

Fig. 3.26 represents the estimated stator values versus mechanical rotor position for PMSM-1. The average d-axis inductance values 145 μH and for q-axis 213 μH, average resistance value is $0.057\ \Omega$ for PMSM-1. The maximum relative error for q-axis inductance is 3.7%, for d-axis inductance is 3.0% and for stator resistance is 5.5%.

The estimation results for PMSM-1 with different dead-time delays are shown in Fig. 3.27, which shows that the presented method accounts for the dead-time effect very well. The phase currents during the whole estimation period for the PMSM-2 are shown in Fig. 3.28. The rotor position is set randomly to any position and estimated $\hat{\theta}$ =2.2

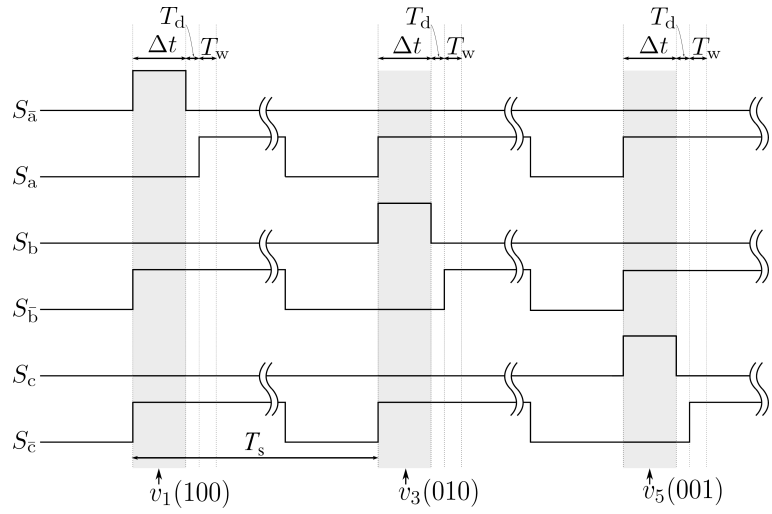

Fig. 3.23. The gate switching sequence (Dilys & Stankevic, 2022)

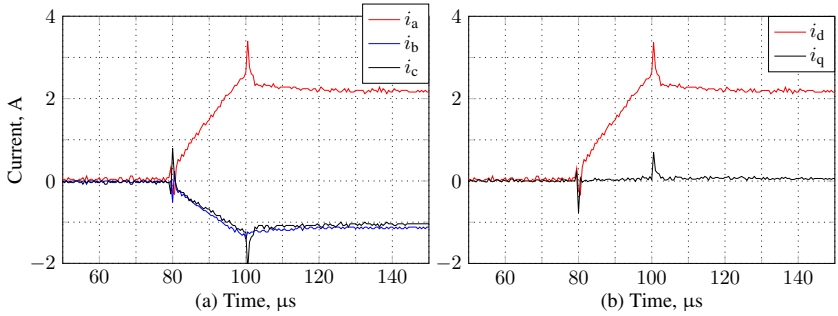

Fig. 3.24. Measured current linear build up during the supply vector v_1 at the estimated rotor position $\hat{\theta} = -0.05$ rad for PMSM-1: (a) the stationary phase currents; and (b) the d-axis and q-axis currents

rad. Because of higher stator resistance, the decay of the PMSM-2 is faster, as shown in Fig. 3.28 compared to Fig. 3.25d. The final estimated inductance values are $\hat{L}_{\mathrm{d}}^{\mathrm{c}} = 145$ µH, $\hat{L}_{\mathrm{q}}^{\mathrm{c}} = 174$ µH and $\hat{R}_s^{\mathrm{c}} = 0.37\ \Omega$.

Fig. 3.29 illustrates the estimated stator values versus mechanical rotor position for the PMSM-2. Average values for the d-axis inductance 148 µH, and for the q-axis 178 µH, the average resistance value is 0.35 Ω for the PMSM-2. The maximum relative error for the d-axis inductance is 1.9%, for the q-axis inductance 2.1%, and for the resistance 5.8% for the PMSM-2 (Dilys & Stankevic, 2022).

The maximum absolute identification error (compared to nominal values) for the d-axis inductance 7.0%, for the q-axis inductance 4.5%, and for the resistance 9.4% for the PMSM-1. And for the PMSM-2 d-axis inductance 3.7%, for the q-axis inductance 2.8%

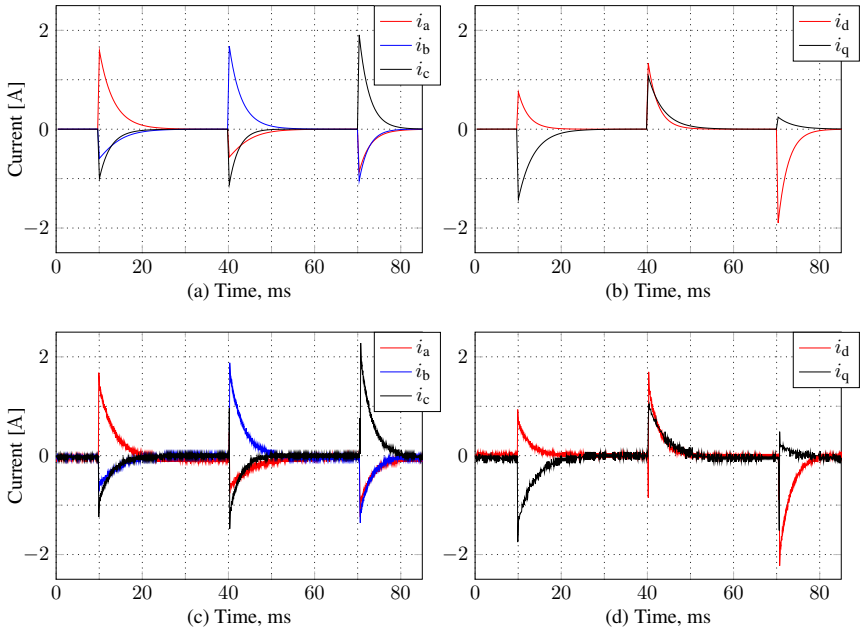

Fig. 3.25. Comparison of PMSM-1's measured and simulated phase currents at the rotor position $\hat{\theta} = 1.23$ rad: (a) stationary reference frame (simulation); (b) rotating reference frame (simulation); (c) stationary reference frame (measured); (d) rotating reference frame (measured)

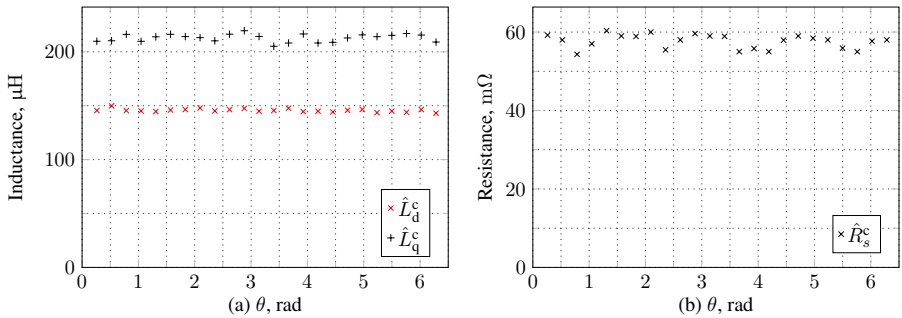

Fig. 3.26. PMSM-1's stator resistance and inductance dependence on mechanical rotor position: (a) dq-axis inductances; (b) stator resistance

and for the resistance 13.1%. In order to verify the effectiveness of the proposed method the results are compared with previous studies and are shown in Table. 3.2. Table. 3.2 allows for concluding that the proposed method's accuracy is very similar to that of previous studies. The identification process is very fast and takes only a part of a second. Moreover, the use of additional equipment is not needed. The motor tests can be performed with or without a locked rotor and do not require knowledge of the initial position. Such an estimation process does not require high computation power; therefore, it can be used

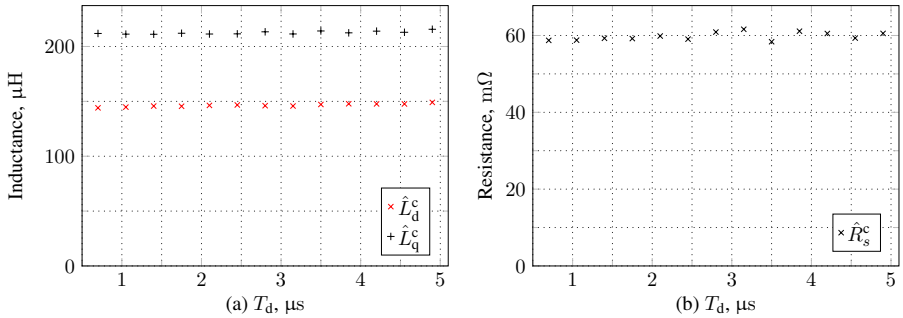

Fig. 3.27. Dependences of stator inductance and resistance on different dead-time for the PMSM-1 motor: (a) dq-axis inductances; (b) stator resistance

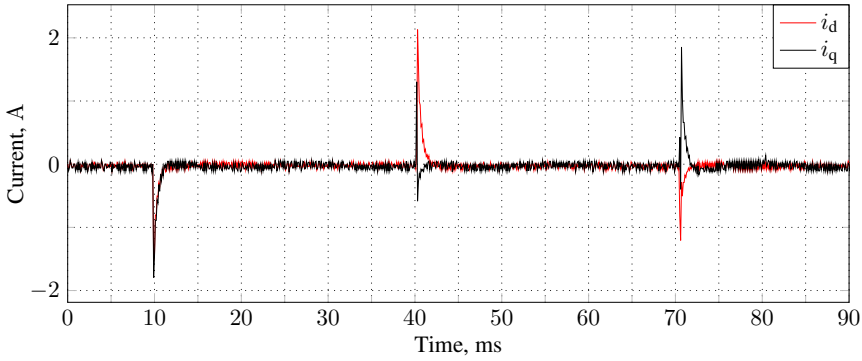

Fig. 3.28. Measured phase currents for the PMSM-2 at rotor position $\hat{\theta} = 2.2$ rad in rotating reference frame

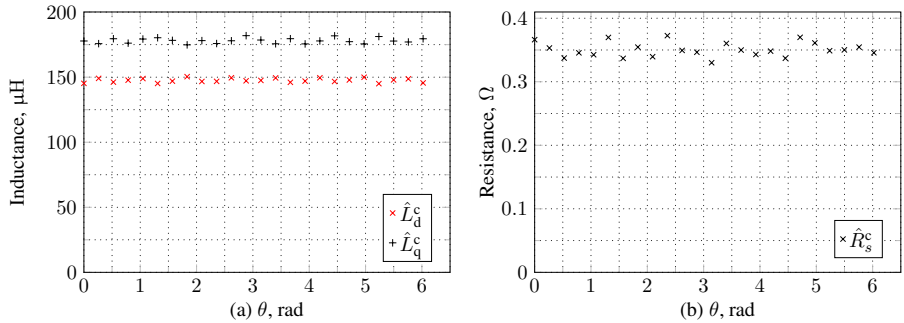

Fig. 3.29. Dependences of stator inductance and resistance on the mechanical rotor position for the PMSM-2: (a) dq-axis inductances; and (b) the stator resistance

for low-cost, low-power embedded systems. A good agreement with the reference PM models is obtained in all the cases. It is shown that the method accounts for the dead-time effect as well (Dilys & Stankevic, 2022). The difference in the method's accuracy com-

Table 3.2. Comparison of maximum identification errors

Method	L_{d}	L_{q}	R_s
Proposed method (PMSM-1)	7.0%	4.5%	9.4%
Proposed method (PMSM-2)	3.7%	2.8%	13.1%
(Wang et al., 2022)	6%	6%	-
(Liu & Zhu, 2016)	14.9%	13.3%	13.3%
(Pescetto & Pellegrino, 2018)	12.4/3.6/5.7%	12.2/3.1/6.6%	-
(Wu et al., 2019)	3.43%	2.68%	-
(Yeh & Yang, 2021)	16%	16%	12/9%
(Wang et al., 2014)	2.90%	12.77%	3.35%

pared to experimental results of the PMSM-1 with the PMSM-2 is because of limitations of physical measurement system. Because the first (PMSM-1) motor stator resistance was much smaller compared to the PMSM-2, the decay time constant is much larger and more accurate measurement were performed in the experiment.

3.4.2. Modified Extended Kalman Filter Experimental Results with Parallel Calculation

Because the EKF algorithm involves heavy online computation performed on matrices, it can be a time-consuming process. To address this issue, it is suggested that the EKF algorithm's overall time be reduced by separating the calculation of EKF matrices from the prediction and measurement update steps. The microcontroller with the ARM Cortex-M3 was used to implement the strategy.

In Fig. 3.30a, the encoder's measured rotor position and the estimated rotor position are compared, for the reference speed is set to 400 rad/s. Fig. 3.30b shows position variance, and Fig. 3.30d presents the Kalman gains for position measurement corrections. The switching frequency f_{s} was set for 5 kHz, while the Kalman gain and all covariance matrices are calculated at the same frequency of $f_{\mathrm{b}} = 5$ kHz. The same measurements are taken in Fig. 3.31 with a 1 kHz Kalman gain and covariance matrix calculation frequency. The Kalman gain and covariance matrixes are computed five times slower to produce the Fig. 3.31 results. The position error is approximately the same average value when comparing the results in Fig. 3.30b and 3.31b. The following provides additional information about position error dependency. The variance P_{44} in Fig. 3.30a and 3.31a is about the same value (0.35 – 0.37). This indicates that the frequency at which Kalman's gain and covariance matrices were calculated did not alter the variance of the estimated position. The extended Kalman gains for position estimation in Fig. 3.30d and Fig. 3.31d have similar shapes and the same magnitude peak values, but the shapes in Fig. 3.31d has more discrete form. The primary reason for the larger discretisation steps is a decrease in the Kalman gain calculation frequency. Within a brief period $(1/f_{\mathrm{b}})$ the control procedure uses the extended Kalman gain matrix multiple times until the background procedure calculates a new one because it is assumed to have a constant value. The position error and covariance matrices calculation rate did not increase when the Kalman gain was reduced, as further experimental tests demonstrated, until some minimum frequency of f_{bmin}

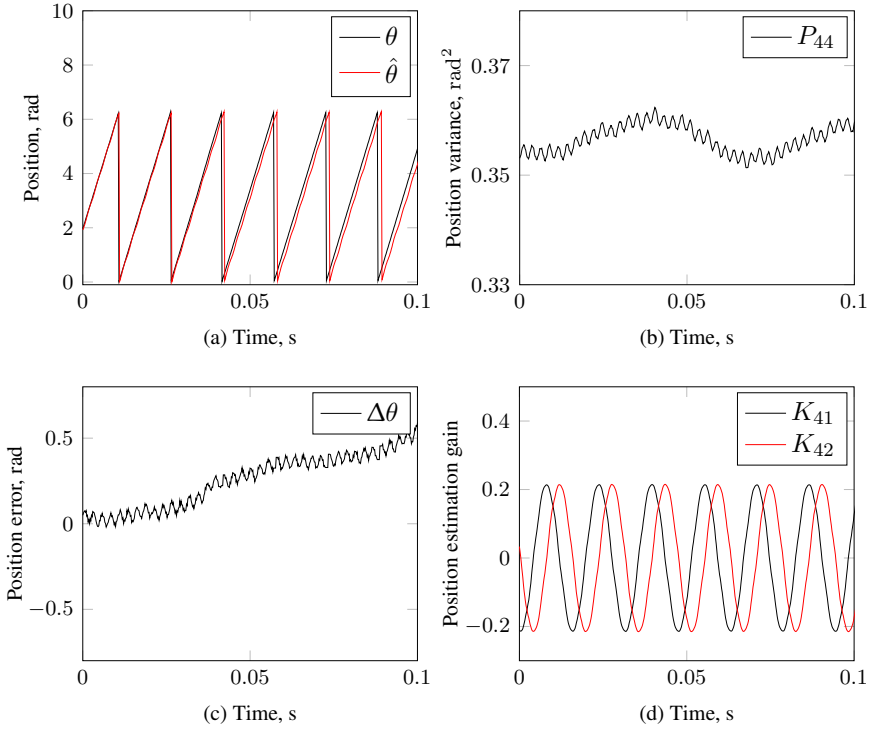

Fig. 3.30. Experimental results of the rotor position estimation performance at $f_b = 5$ kHz $f_s = 5$ kHz and $w_e = 400$ rads: (a) measured and estimated rotor positions; (b) the estimated position error; (c) the estimated position variance; and (d) position estimation Kalman gains

is reached. The errors at various f_b frequencies for the position are shown in Fig. 3.33. Fig. 3.33e the Kalman gain, and its covariance estimation update rate, is multiple times more slow ($f_b = f_s/12$) than the switching frequency, and the order of the position error roughly matches the calculation for each switching instance (Dilys et al., 2021).

However, synchronization will be lost if the Kalman gain and covariance matrices' update rate is slowed. The synchronization is lost, the rotor speed decreases to zero, and reverse spin occurs when $f_b = f_s/13$ and the reference speed is set to w_{eref} =400 Hz, as shown inFig. 3.32.

The most recent experimental tests have demonstrated that the relationship between the fundamental electrical rotor speed and the minimum Kalman gain and covariance matrices' calculation update rate is very similar to simulation results.

Fig. 3.32b shows the position error with a small Kalman gain and covariance matrices update rate.

Fig. 3.34a depicts the relation between the minimum matrices' calculation frequency f_{bmin} and fundamental rotor frequency f_e. To obtain the relation of $\frac{f_b}{f_e}$ the experiments with

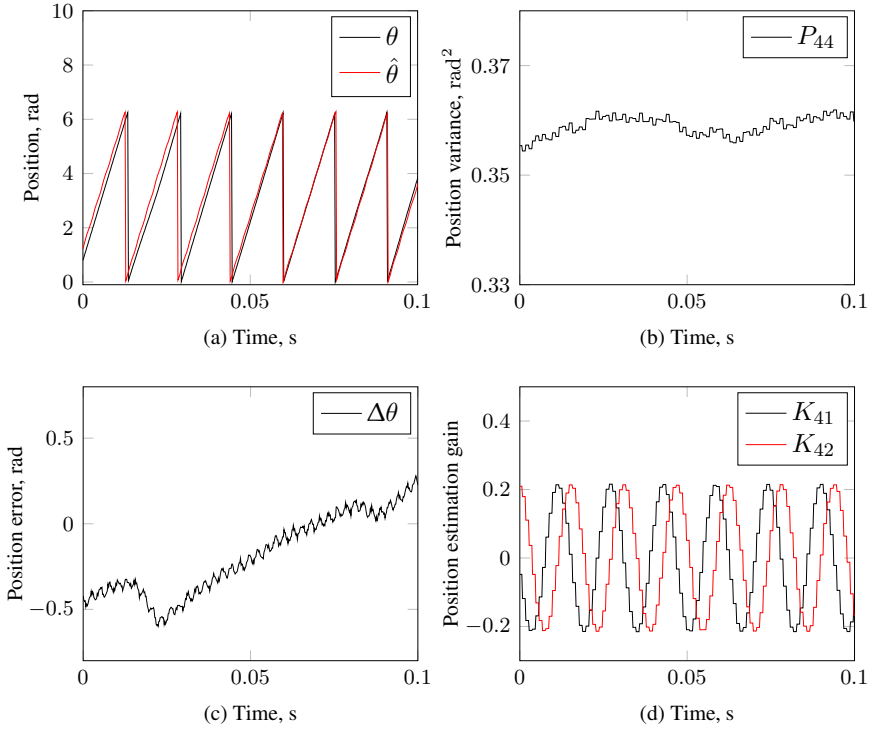

Fig. 3.31. Experimental results at the rotor position estimation performance at $f_{\mathrm{b}} = 1$ kHz, $f_{\mathrm{s}} = 5$ kHz and $w_{\mathrm{e}} = 400$ rads: (a) measured and estimated rotor positions; (b) estimated rotor position error; (c) estimated rotor position variance; (d) Kalman gains for rotor position estimation

different speed reference points were analysed. For each speed reference point, the minimum frequency f_{bmin} was searched. The frequency f_{bmin} was considered enough high if the motor speed with constant reference speed was controllable. In the experiment, the frequency f_{bmin} was reduced until the control was lost. The loss of control was easy to see from the rotor speed not able to follow the speed reference set-point, and the speed of rotor dropped to zero. The synchronization was lost (Dilys et al., 2021). This experiment revealed that the required update matrices calculation rate increased with reference speed. Fig. 3.34a shows the relation of the minimum required f_{bmin} and f_{e} is linear. Fig. 3.34b displays the same measured data as Fig. 3.34a, by calculating the ratio $\frac{f_{\mathrm{b}}}{f_{\mathrm{e}}}$. Fig. 3.34b shows how often, per rotor electrical period, the Kalman gain and the covariance lattices must be registered without letting completely go. For high frequencies ($f_{\mathrm{e}} > 50$ Hz), the minimum Kalman gain and the covariance matrices must be computed seven times per one-rotor electrical period, as shown in Fig. 3.34b. The lower ratio of the Kalman gain and the covariance matrix calculation ratio ($\frac{f_{\mathrm{b}}}{f_{\mathrm{e}}} < 6$) will mostly cause the loss of control. Of course, the higher ratio ($\frac{f_{\mathrm{b}}}{f_{\mathrm{e}}} > 7$) will be beneficial, but the higher ratio implies that

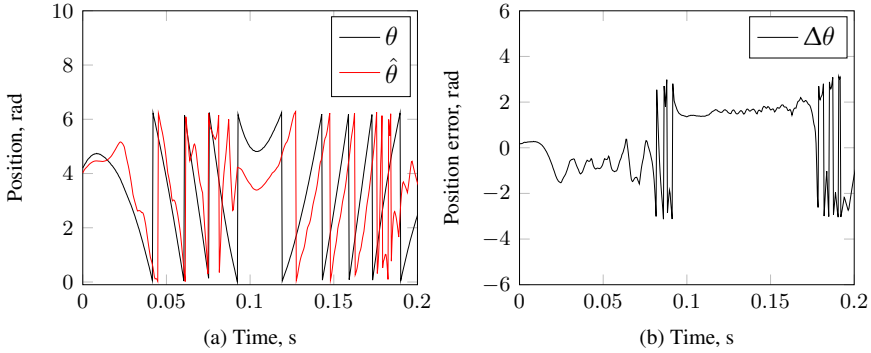

Fig. 3.32. At, synchronization failed: $f_{\mathrm{b}} = 384$ Hz, $f_{\mathrm{s}} = 5$ kHz and reference speed $w_{\mathrm{eref}} = 400$ rad/s: (a) measured (θ) and estimated ($\hat{\theta}$) rotor positions; (b) estimated rotor position error ($\Delta\theta$)

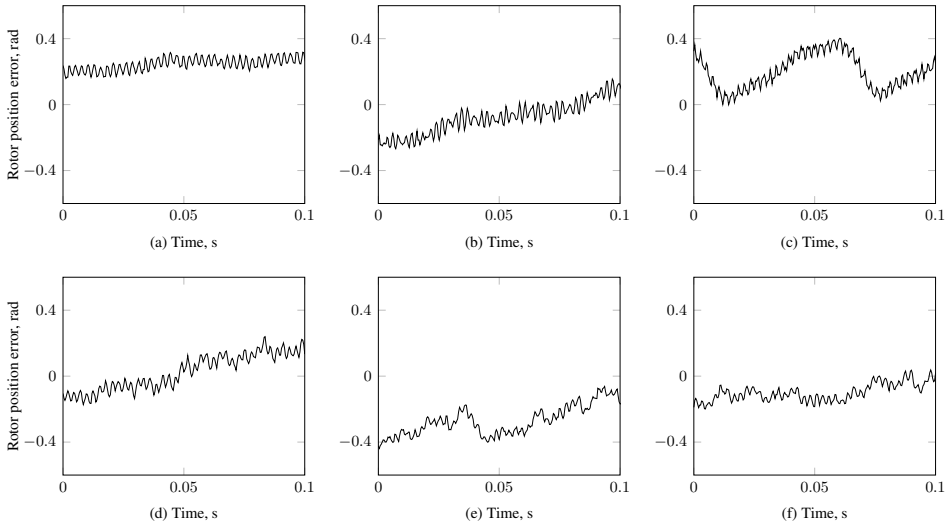

Fig. 3.33. Estimated position errors. The electrical angular speed of the rotor is 400 rad/s, and the switching frequency is 5 kHz: (a) $f_{\mathrm{b}} = 5$ kHz; (b) $f_{\mathrm{b}} = 2.5$ kHz; (c) $f_{\mathrm{b}} = 1.25$ kHz; (d) $f_{\mathrm{b}} = 500$ Hz; (e) $f_{\mathrm{b}} = 454$ Hz; (f) $f_{\mathrm{b}} = 416$ Hz

more computational power is required. In addition, Fig. 3.34b allows for concluding that at low frequencies ($f_{\mathrm{e}} < 50$ Hz), a ratio of $\frac{f_{\mathrm{b}}}{f_{\mathrm{e}}}$ higher than seven is needed, but Fig. 3.34a shows that the minimal requirement frequency f_{bmin} is diminishing regardless of whether the proportion $\frac{f_{\mathrm{bmin}}}{f_{\mathrm{e}}}$ increases (Dilys et al., 2021).

The uses of the ARM Cortex-M3 LPC1549 processor for running the EKF estimator at various background frequencies are described in Table 3.3. Additionally, we can de-

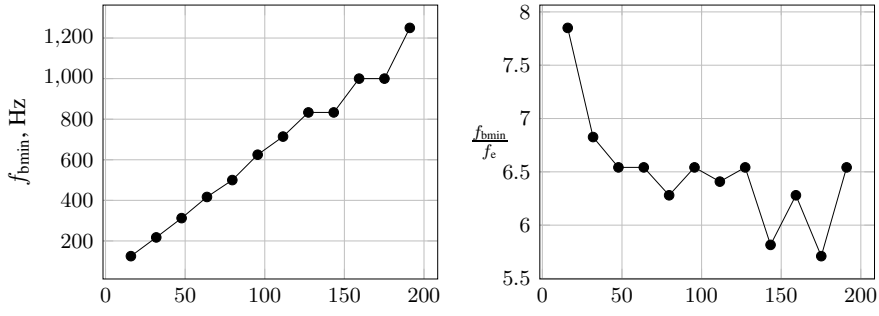

Fig. 3.34. Relation measured experimentally between the calculation frequency and the rotor electrical frequency: (a) between the minimum required f_{bmin} and f_{e}; (b) between the ratio of f_{bmin} to f_{e} to electrical frequency f_{e}

Table 3.3. Processor uses for executing EKF estimator with different background frequencies, $f_{\text{s}} = 5$ kHz.

f_{b}	**CPU Use**	f_{emax}
5 kHz	18.85%	714 Hz
2.5 kHz	10.95%	357 Hz
1.25 kHz	7.0%	179 Hz
500 Hz	6.21%	71 Hz

termine the maximum permissible electrical frequency (f_{emax}) in control by applying the requirement that Kalman gain and covariance matrices be computed at least seven times per electrical period of a rotor. The system's maximum electrical frequency and processor use must be balanced at that level of optimization. Table Table 3.3 reveals that even a two-fold reduction in background frequency from 5 kHz to 2.5 kHz yields a satisfactory time optimization. The processor time for each step is reduced as a result of this additional reduction. The maximum improvement in processor performance, which reduced the total the processor use by more than three times, was from 18.85% to 6.21%.

3.4.3. The Unscented Kalman Filter for the Sensorless Speed Control

Table 3.4. ARM processor uses for EKF and UKF comparison

Method	**No Optimisation**	**Optimised**
EKF	260 μs	38 μs
UKF	1000 μs	90 μs

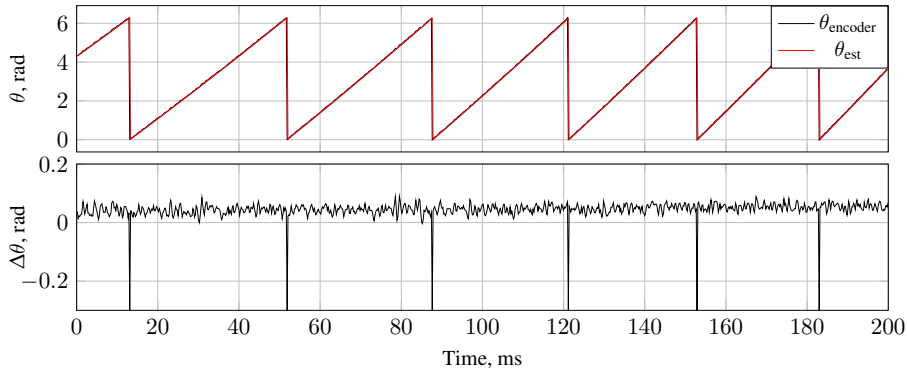

Fig. 3.35. UKF rotor position estimation performance

The unscented Kalman filter performance of estimating the PMSM rotor position is shown in Fig. 3.35. The estimated rotor position is θ_{est}, and the measured rotor position is θ_{encoder}. The position estimation error is obtained by $\Delta\theta = \theta_{\text{encoder}} - \theta_{\text{est}}$. Based on Fig. 3.35, the position error $\Delta\theta$ is relatively small, and UKF is suited for the PMSM rotor position estimation. The experimentally obtained UKF execution time has been compared with extended Kalman filter execution time (Table. 3.4). The UKF for speed and position estimation execution time on the ARM Cortex-M3 processor are more than two times longer compared to the extended Kalman filter. The total execution time of the UKF filter is about 90 µs and can only be implemented at a low switching frequency.

3.5. Conclusions of the Third Chapter

1. The d- and q-axis inductances at standstill operation were estimated by applying three short-time voltage pulses and measuring phase current peak values. For the stator inductance and the resistance estimation at a standstill experiments were conducted on two different PMSMs. For the first motor, the maximum relative error for the d-axis inductance was 3.0%, for the q-axis inductance 3.7% and for resistance 5.5%. For the second motor the maximum relative error for the d-axis inductance is 1.9%, for the q-axis inductance 2.1% and for the resistance 5.8%.
2. The execution time of the extended Kalman filter for speed and position was reduced from 260.4 µs to 37.7 µs without a loss in accuracy. Additionally, the separation of a Kalman gain and the covariance matrix calculation from prediction and measurement state update reduces the total microcontroller processing use from 18.8% to 6.2%.
3. In EKF sensorless control, the minimum required Kalman gain and all covariance matrix update ratios depend on the fundamental electrical frequency; the higher the electrical frequency, the higher the update frequency is required.
4. The EKF method provides two times shorter speed and position estimation time

on the ARM Cortex-M3 processor compared to the UKF method.

5. The B-scalar sensor can be used for measuring the magnetic flux density at the PMSM air gap region.

General Conclusions

1. The created mathematical model of the permanent magnet synchronous motor, based on analytical expressions of magnetic flux density, allows evaluating the pulsations of the torque, distribution of stator inductance, and form of the electromotive force.
2. The proposed modification of the extended Kalman filter algorithm for determining the speed and position of the PMSM rotor allows reducing the computation time by three times, by separating the calculation of the covariance matrices from the entire algorithm and calculating them at a slower frequency.
3. The stator resistance and inductance of a permanent magnet synchronous motor can be determined, with the rotor in a standstill state, by using three 20 μs voltage pulses and measuring the phase stator currents.
4. The designed magnetic field measurement systems based on the CMR sensor can be used to measure the magnetic flux density waveform in PMSM the air gap region.

References

Alonso, D. F., Kang, Y., Fernández Laborda, D., Gómez, M. M., Reigosa, D. D., & Briz, F. (2021). Permanent magnet synchronous machine torque estimation using low cost hall-effect sensors. *IEEE Transactions on Industry Applications*, 57(4):3735–3743.

Alonso, D. F., Kang, Y., Laborda, D. F., Gómez, M. M., Reigosa, D. D., & Briz, F. (2019). Permanent magnet synchronous machine torque estimation using low cost hall-effect sensors. In *2019 IEEE 10th International Symposium on Sensorless Control for Electrical Drives (SLED)* 1–6.

Atallah, K., Zhu, Z. Q., & Howe, D. (1998). Armature reaction field and winding inductances of slotless permanent-magnet brushless machines. *IEEE Transactions on Magnetics*, 34(5):3737–3744.

Auger, F., Hilairet, M., Guerrero, J. M., Monmasson, E., Orlowska-Kowalska, T., & Katsura, S. (2013). Industrial applications of the Kalman filter: A review. *IEEE Transactions on Industrial Electronics*, 60(12):5458–5471.

Bae, B.-H., Sul, S.-K., Kwon, J.-H., & Byeon, J.-S. (2003). Implementation of sensorless vector control for super-high-speed pmsm of turbo-compressor. *IEEE Transactions on Industry Applications*, 39(3):811–818.

Balevičius, S., Žurauskienė, N., Stankevič, V., Herrmannsdörfer, T., Zherlitsyn, S., Skourski, Y., Wolff-Fabris, F., & Wosnitza, J. (2013). Cmr-b-scalar sensor application for high magnetic field measurement in nondestructive pulsed magnets. *IEEE Transactions on Magnetics*, 49(11):5480–5484.

Balčaitis, M. (2016). Ventiliacinės sistemos bešepetės pavaros tyrimas. *Vilniaus Gedimino technikos universitetas*.

Bellini, A., Concari, C., Franceschini, G., Tassoni, C., & Toscani, A. (2006). Vibrations, currents and stray flux signals to asses induction motors rotor conditions. In *IECON 2006-32nd Annual Conference on IEEE Industrial Electronics* 4963–4968. IEEE.

Bian, X., Wei, Z., He, J., Yan, F., & Liu, L. (2021). A two-step parameter optimization method for low-order model-based state-of-charge estimation. *IEEE Transactions on Transportation Electrification*, 7(2):399–409.

Bolognani, S., Tubiana, L., & Zigliotto, M. (2003). Extended Kalman filter tuning in sensorless pmsm drives. *IEEE Transactions on Industry Applications*, 39(6):1741–1747.

Borsje, P., Chan, T., Wong, Y., & Ho, S. (2005). A comparative study of Kalman filtering for sensorless control of a permanent-magnet synchronous motor drive. In *IEEE International Conference on Electric Machines and Drives, 2005.* 815–822.

Boussak, M. (2005). Implementation and experimental investigation of sensorless speed control with initial rotor position estimation for interior permanent magnet synchronous motor drive. *IEEE Transactions on Power Electronics*, 20(6):1413–1422.

Bui, M. X., Xiao, D., Rahman, M. F., & Guan, D. Q. (2017). Online estimation of inductances of permanent magnet synchronous machines based on current derivative measurements. In *2017 20th International Conference on Electrical Machines and Systems (ICEMS)* 1–6.

Burgos, R. P., Kshirsagar, P., Lidozzi, A., Jang, J., Wang, F., Boroyevich, D., Rodriguez, P., & Sul, S.-K. (2006). Design and evaluation of a pll-based position controller for sensorless vector control of permanent-magnet synchronous machines. In *IECON 2006 - 32nd Annual Conference on IEEE Industrial Electronics* 5081–5086.

Chau, K. (2015). *Electric Vehicle Machines and Drives: Design, Analysis and Application (IEEE Press)*. Wiley-IEEE Press, 1 edition.

Cheng, W., Sun, Y., Yu, L., Huang, L., Lv, Y., & Li, L. (2015). Analytical solution to magnetic field distribution of a parallel magnetised rotor with cylindrical or ring-type permanent magnet. *IET Electric Power Applications*, 9(6):429–437.

Chethan, G. N. & Kodeeswara Kumaran, G. (2019). Performance analysis of pmsm drive with spacevector pwm and sinusoidal pwm fed vsi. In *2019 International Conference on Power Electronics Applications and Technology in Present Energy Scenario (PETPES)* 1–6.

Cho, S., Ahn, H., Cong Liu, H., Hong, H.-S., Lee, J., & Go, S.-C. (2017). Analysis of inductance according to the applied current in spoke-type pmsm and suggestion of driving mode. *IEEE Transactions on Magnetics*, 53(6):1–4.

Choi, S., Haque, M. S., Tarek, M. T. B., Mulpuri, V., Duan, Y., Das, S., Garg, V., Ionel, D. M., Masrur, M. A., Mirafzal, B., & Toliyat, H. A. (2018). Fault diagnosis techniques for permanent magnet ac machine and drives—a review of current state of the art. *IEEE Transactions on Transportation Electrification*, 4(2):444–463.

Consoli, A., Scarcella, G., & Testa, A. (2001). Industry application of zero-speed sensorless control techniques for pm synchronous motors. *IEEE Transactions on Industry Applications*, 37(2):513–521.

Dhaouadi, R., Mohan, N., & Norum, L. (1991). Design and implementation of an extended Kalman filter for the state estimation of a permanent magnet synchronous motor. *IEEE Transactions on Power Electronics*, 6(3):491–497.

Djelloul-Khedda, Z., Boughrara, K., Dubas, F., & Ibtiouen, R. (2017). Nonlinear analytical prediction of magnetic field and electromagnetic performances in switched reluctance machines. *IEEE Transactions on Magnetics*, 53(7):1–11.

Djelloul-Khedda, Z., Boughrara, K., Dubas, F., Kechroud, A., & Souleyman, B. (2018). Semi-analytical magnetic field predicting in many structures of permanent-magnet synchronous machines considering the iron permeability. *IEEE Transactions on Magnetics*, 54(7):1–21.

Eklund, P. & Eriksson, S. (2019). The influence of permanent magnet material properties on generator rotor design. *Energies*, 12(7):1314.

Elez, A., Tomicic, B., & Colak, A. (2008). The comparison of magnetic values obtained from hall probes and measuring coils in synchronous generators. In *2008 18th International Conference on Electrical Machines* 1–4.

Elkasabgy, N., Eastham, A., & Dawson, G. (1992). Detection of broken bars in the cage rotor on an induction machine. *IEEE Transactions on Industry Applications*, 28(1):165–171.

Fabian, M., Hind, D. M., Gerada, C., Sun, T., & Grattan, K. T. V. (2018). Comprehensive monitoring of electrical machine parameters using an integrated fiber bragg grating-based sensor system. *Journal of Lightwave Technology*, 36(4):1046–1051.

Feng, G., Lai, C., & Kar, N. C. (2016). A novel current injection-based online parameter estimation method for pmsms considering magnetic saturation. *IEEE Transactions on Magnetics*, 52(7):1–4.

Filho, C., de Alvarenga, B. P., & de Paula, G. T. (2020). On-load apparent inductance derivative of ipmsm: Assessment method and torque estimation. *IEEE Transactions on Magnetics*, 56(4):1–10.

Fitzgerald, A. (2022). *Electric Machinery*. McGraw-Hill Science/Engineerin, 6 edition.

Fracarolli, J. P., Rosolem, J. B., Tomiyama, E. K., Floridia, C., Penze, R. S., Peres, R., Dini, D. C., Hortencio, C. A., Dilli, P. I., da Silva, E. V., Marcéu C, d. S., & Fruett, F. (2016). Development and field trial of a FBG-based magnetic sensor for large hydrogenerators. In *Fiber Optic Sensors and Applications XIII*, Vol 9852 159–164. SPIE.

Ge, S., Qiu, L., Zhang, Z., Guo, D., & Ren, H. (2022). Integrated impacts of non-ideal factors on the vibration characteristics of permanent magnet synchronous motors for electric vehicles. *Machines*, 10(9):739.

Gibbs, W. (1958). *Conformal Transformations in Electrical Engineering*. Chapman and Hall.

Gieras, J. (2009). *Permanent Magnet Motor Technology: Design and Applications, Third Edition (Electrical and Computer Engineering)*. CRC Press, 3 edition.

Gutfleisch, O., Willard, M. A., Brück, E., Chen, C. H., Sankar, S. G., & Liu, J. P. (2010). Magnetic Materials and Devices for the 21st Century: Stronger, Lighter, and More Energy Efficient. *Advanced Materials*, 23(7):821–842.

Guziński, J., Morawiec, M., Krzemiński, Z., Łuksza, K., Strankowski, P., & Kouzou, A. (2019). Sensorless low speed pmsm motor control with cogging torque compensation. In *2019 2nd International Conference on Smart Grid and Renewable Energy (SGRE)* 1–6.

Gómez, D. J., Tovar-Barranco, A., Rodríguez, A. L., López-de Heredia, A., & Villar, I. (2016). On-load cogging torque calculation using frozen permeability method and permeance network models. In *2016 XXII International Conference on Electrical Machines (ICEM)* 499–505.

Hannon, B., Sergeant, P., Dupré, L., & Pfister, P.-D. (2019). Two-dimensional fourier-based modeling of electric machines—an overview. *IEEE Transactions on Magnetics*, 55(10):1–17.

Hu, C., Duan, P., Wang, J., Duan, W., Zou, Z., & Chang, L. (2011). Colossal magnetoresistance effect in perovskite la0.9sb0.1mno3 films prepared by pulsed laser deposition. In *2011 International Conference on Multimedia Technology* 2044–2046.

Ilioudis, V. C. (2017). Pll type estimator applied in pmsm sensorless control for speed and position. In *2017 Twelfth International Conference on Ecological Vehicles and Renewable Energies (EVER)* 1–8.

Imamura, R., Wu, T., & Lorenz, R. D. (2019). Design of variable magnetization pattern machines for dynamic changes in the back emf waveform. *IEEE Transactions on Industry Applications*, 55(4):3469–3478.

Isfahani, A. H., Vaez-Zadeh, S., & Rahman, M. A. (2008). Using modular poles for shape optimization of flux density distribution in permanent-magnet machines. *IEEE Transactions on Magnetics*, 44(8):2009–2015.

Jabbar, M., Zhejie, L., & Jing, D. (2003). Time stepping finite element analysis for the dynamic performance of a permanent magnet synchronous motor. In *2003 IEEE International Magnetics Conference (INTERMAG)* FP–08.

Jahns, T. M., Kliman, G. B., & Neumann, T. W. (1986). Interior permanent-magnet synchronous motors for adjustable-speed drives. *IEEE Transactions on Industry Applications*, IA-22(4):738–747.

Ji, L., Xu, Y., Zou, J., & Wang, M. (2019). Sensorless control for pmsm with novel back emf observer based on quasi-pr controller. In *2019 22nd International Conference on Electrical Machines and Systems (ICEMS)* 1–5.

Jiang, F., Yang, K., Sun, S., Xu, Y., & Liu, A. (2019). Back-emf based sensorless control of pmsm with an improved pll for eliminating the position estimation fluctuation. In *2019 22nd International Conference on Electrical Machines and Systems (ICEMS)* 1–4.

Julier, S. & Uhlmann, J. (2004). Unscented filtering and nonlinear estimation. *Proceedings of the IEEE*, 92(3):401–422.

Kar, S., Sarkar, J., & Raychaudhuri, A. K. (2006). Investigation of the effect of microstructure and grain boundaries in nanostructured cmr thin films using scanning tunneling microscopy (stm) and local conductance map (lcmap). *IEEE Transactions on Nanotechnology*, 5(6):707–711.

Kim, P. & Huh, L. (2010). *Kalman Filter for Beginners with MATLAB Examples*. A-JIN.

Kim, S. A., Song, J. H., Han, S. W., & Cho, Y. H. (2018). An improved dynamic modeling of permanent magnet synchronous machine with torque ripple characteristics. *Journal of Clean Energy Technologies*, 6(2):117–120.

Kim, S.-H. (2017). *Electric Motor Control: DC, AC, and BLDC Motors*. Elsevier Science, 1 edition.

Kim, U. & Lieu, D. (1998). Magnetic field calculation in permanent magnet motors with rotor eccentricity: with slotting effect considered. *IEEE Transactions on Magnetics*, 34(4):2253–2266.

Klontz, K. W. (2017). Permanent magnet motor with tested efficiency beyond ultra-premium / ie 5 levels.

Lascu, C. & Andreescu, G.-D. (2020). Pll position and speed observer with integrated current observer for sensorless pmsm drives. *IEEE Transactions on Industrial Electronics*, 67(7):5990–5999.

Le Roux, W., Harley, R., & Habetler, T. (2003). Detecting rotor faults in permanent magnet synchronous machines. In *4th IEEE International Symposium on Diagnostics for Electric Machines, Power Electronics and Drives, 2003. SDEMPED 2003.* 198–203.

Lee, J. (1992). Measurement of magnetic fields in axial field motors. *IEEE Transactions on Magnetics*, 28(5):3021–3023.

Lee, S. B., Shin, J., Park, Y., Kim, H., & Kim, J. (2021). Reliable flux-based detection of induction motor rotor faults from the fifth rotor rotational frequency sideband. *IEEE Transactions on Industrial Electronics*, 68(9):7874–7883.

Ley, B. J. & Charmatz, A. (1955). Magnetic flux density measurements in rotating machines. *Transactions of the American Institute of Electrical Engineers, Part I: Communication and Electronics*, 74(4):525–528.

Li, Q., Fan, T., & Wen, X. (2013). Armature-reaction magnetic field analysis for interior permanent magnet motor based on winding function theory. *IEEE Transactions on Magnetics*, 49(3):1193–1201.

Liang, P., Pei, Y., Chai, F., Bi, Y., & Cheng, S. (2016). An improved method for armature-reaction magnetic field calculation of interior permanent magnet motors. *IEEE Transactions on Magnetics*, 52(7):1–4.

Liu, G., Du, X., Zhao, W., & Chen, Q. (2017). Reduction of torque ripple in inset permanent magnet synchronous motor by magnets shifting. *IEEE Transactions on Magnetics*, 53(2):1–13.

Liu, K. & Zhu, Z. Q. (2016). Determination of electrical parameters of pmsm drive system at standstill. In *2016 IEEE Vehicle Power and Propulsion Conference (VPPC)* 1–6.

Maeda, Y., Urata, S., & Nakai, H. (2018). Measurement technique for magnetic flux in a motor core under operating conditions. *IEEE Transactions on Magnetics*, 54(11):1–4.

Matsui, N. (1996). Sensorless pm brushless dc motor drives. *IEEE Transactions on Industrial Electronics*, 43(2):300–308.

Matsui, N. & Takeshita, T. (1994). A novel starting method of sensorless salient-pole brushless motor. In *Proceedings of 1994 IEEE Industry Applications Society Annual Meeting*, Vol 1 386–392.

Min, S. G. & Sarlioglu, B. (2017). Investigation of electromagnetic noise on pole and slot number combinations with possible fractional-slot concentrated windings. In *2017 IEEE Transportation Electrification Conference and Expo (ITEC)* 241–246.

Mohammed, A. & Djurovic, S. (2019). In-situ thermal and mechanical fibre optic sensing for in-service electric machinery bearing condition monitoring. In *2019 IEEE International Electric Machines & Drives Conference (IEMDC)* 37–43.

Mohammed, A. & Djurović, S. (2018). Stator winding internal thermal monitoring and analysis using in situ fbg sensing technology. *IEEE Transactions on Energy Conversion*, 33(3):1508–1518.

Mohammed, A., Melecio, J. I., & Djurović, S. (2019). Open-circuit fault detection in stranded pmsm windings using embedded fbg thermal sensors. *IEEE Sensors Journal*, 19(9):3358–3367.

Mohammed, A., Melecio, J. I., & Djurović, S. (2020). Electrical machine permanent magnets health monitoring and diagnosis using an air-gap magnetic sensor. *IEEE Sensors Journal*, 20(10):5251–5259.

Paitandi, S. & Sengupta, M. (2017). Design and implementation of sensorless vector control of surface mounted pmsm using back-emf estimation and pll based technique. In *2017 National Power Electronics Conference (NPEC)* 129–134.

Paitandi, S. & Sengupta, M. (2020). Analysis, fabrication and detailed comparative study of surface and interior rotor PMSM prototypes of identical nominal ratings and stators. *Sādhanā*, 45(1).

Parasiliti, F., Villani, M., & Tassi, A. (2006). Dynamic analysis of synchronous reluctance motor drives based on simulink® and finite element model. In *IECON 2006 - 32nd Annual Conference on IEEE Industrial Electronics* 1516–1520.

Park, Y., Choi, H., Lee, S. B., & Gyftakis, K. N. (2020a). Search coil-based detection of nonadjacent rotor bar damage in squirrel cage induction motors. *IEEE Transactions on Industry Applications*, 56(5):4748–4757.

Park, Y., Choi, H., Shin, J., Park, J., Lee, S. B., & Jo, H. (2020b). Airgap flux based detection and classification of induction motor rotor and load defects during the starting transient. *IEEE Transactions on Industrial Electronics*, 67(12):10075–10084.

Park, Y., Fernandez, D., Lee, S. B., Hyun, D., Jeong, M., Kommuri, S. K., Cho, C., Diaz Reigosa, D., & Briz, F. (2019a). Online detection of rotor eccentricity and demagnetization faults in pmsms based on hall-effect field sensor measurements. *IEEE Transactions on Industry Applications*, 55(3):2499–2509.

Park, Y., Yang, C., Lee, S. B., Lee, D.-M., Fernandez, D., Reigosa, D., & Briz, F. (2019b). Online detection and classification of rotor and load defects in pmsms based on hall sensor measurements. *IEEE Transactions on Industry Applications*, 55(4):3803–3812.

Pescetto, P. & Pellegrino, G. (2018). Automatic tuning for sensorless commissioning of synchronous reluctance machines augmented with high-frequency voltage injection. *IEEE Transactions on Industry Applications*, 54(5):4485–4493.

Phyu, H. N. & Chao, B. (2012). Effect of magnetization on high-speed permanent magnet synchronous motor design. In *2012 15th International Conference on Electrical Machines and Systems (ICEMS)* 1–6.

Pillay, P. & Krishnan, R. (1988). Modeling of permanent magnet motor drives. *IEEE Transactions on Industrial Electronics*, 35(4):537–541.

Pitrėnas, A. (2013). Imitacinis elektroniškai komutuojamos nuolatinės srovės pavaros modelis. *Science: Future of Lithuania*, 5(2):164–168.

Piña Ortega, A. J., Paul, S., Islam, R., & Xu, L. (2016). Analytical model for predicting effects of manufacturing variations on cogging torque in surface-mounted permanent magnet motors. *IEEE Transactions on Industry Applications*, 52(4):3050–3061.

Ponomarev, P., Petrov, I., & Pyrhönen, J. (2014). Influence of travelling current linkage harmonics on inductance variation, torque ripple and sensorless capability of tooth-coil permanent-magnet synchronous machines. *IEEE Transactions on Magnetics*, 50(1):1–8.

Popescu, M. (2006). Prediction of the electromagnetic torque in synchronous machines through maxwell stress harmonic filter (hft) method. *Electrical Engineering*, 89:117–125.

Proca, A., Keyhani, A., El-Antably, A., Lu, W., & Dai, M. (2003). Analytical model for permanent magnet motors with surface mounted magnets. *IEEE Transactions on Energy Conversion*, 18(3):386–391.

Pusca, R., Romary, R., Ceban, A., & Brudny, J.-F. (2010). An online universal diagnosis procedure using two external flux sensors applied to the ac electrical rotating machines. *Sensors*, 10(11):10448–10466.

Qiu, A., Wu, B., & Kojori, H. (2004). Sensorless control of permanent magnet synchronous motor using extended Kalman filter. In *Canadian Conference on Electrical and Computer Engineering 2004 (IEEE Cat. No.04CH37513)*, Vol 3 1557–1562 Vol.3.

Rabinovici, R. (1996). Magnetic field analysis of permanent magnet motors. *IEEE Transactions on Magnetics*, 32(1):265–269.

Rahideh, A. & Korakianitis, T. (2011). Analytical magnetic field distribution of slotless brushless machines with inset permanent magnets. *IEEE Transactions on Magnetics*, 47(6):1763–1774.

Rahideh, A. & Korakianitis, T. (2012). Analytical magnetic field distribution of slotless brushless pm motors. part 2: Open-circuit field and torque calculations. *Electric Power Applications, IET*, 6:639–651.

Rahideh, A., Mardaneh, M., & Korakianitis, T. (2013). Analytical 2-d calculations of torque, inductance, and back-emf for brushless slotless machines with surface inset magnets. *IEEE Transactions on Magnetics*, 49(8):4873–4884.

Rallabandi, V., Taran, N., Ionel, D. M., & Zhou, P. (2019). Inductance testing for ipm synchronous machines according to the new ieee std 1812 and typical laboratory practices. *IEEE Transactions on Industry Applications*, 55(3):2649–2659.

Ramakrishnan, K., Curti, M., Zarko, D., Mastinu, G., Paulides, J. J., & Lomonova, E. A. (2016). A comparison study of modelling techniques for permanent magnet machines. In *2016 Eleventh International Conference on Ecological Vehicles and Renewable Energies (EVER)* 1–6.

Ramirez-Nunez, J. A., Antonino-Daviu, J. A., Climente-Alarcón, V., Quijano-López, A., Razik, H., Osornio-Rios, R. A., & Romero-Troncoso, R. d. J. (2018). Evaluation of the detectability of electromechanical faults in induction motors via transient analysis of the stray flux. *IEEE Transactions on Industry Applications*, 54(5):4324–4332.

Reigosa, D., Fernandez, D., González, C., Lee, S. B., & Briz, F. (2018). Permanent magnet synchronous machine drive control using analog hall-effect sensors. *IEEE Transactions on Industry Applications*, 54(3):2358–2369.

Romary, R., Roger, D., & Brudny, J.-F. (2009). Analytical computation of an ac machine external magnetic field. *The European Physical Journal - Applied Physics*, 47(3):31102.

Saadoun, A. & Amirat, Y. (2014). Magnetic flux density measurement in permanent magnet synchronous machines. In *2014 15th International Conference on Sciences and Techniques of Automatic Control and Computer Engineering (STA)* 355–359.

Schneider, M., Schneider, R., Stankevic, V., Balevicius, S., & Zurauskiene, N. (2007). Highly local measurements of strong transient magnetic fields during railgun experiments using cmr-based sensors. *IEEE Transactions on Magnetics*, 43(1):370–375.

Shi, Y., Zhu, Z., & Howe, D. (2005). Ekf-based hybrid controller for permanent magnet brushless motors combining hall sensors and a flux-observer-based sensorless technique. In *IEEE International Conference on Electric Machines and Drives, 2005.* 1466–1472.

Simón-Sempere, V., Burgos-Payán, M., & Cerquides-Bueno, J.-R. (2017). Cogging torque cancellation by magnet shaping in surface-mounted permanent-magnet motors. *IEEE Transactions on Magnetics*, 53(7):1–7.

Solli, J. F. (2014). *Measurements of Magnetic Flux Density in Rotating Machines*. University of Agder.

Song, W., Gang, Y., Zhi-Jian, Q., Shuang-shuang, S., & Chao, C. (2009). Identification of pmsm based on ekf and elman neural network. In *2009 IEEE International Conference on Automation and Logistics* 1459–1463.

Song, X., Fang, J., & Han, B. (2016). High-precision rotor position detection for high-speed surface pmsm drive based on linear hall-effect sensors. *IEEE Transactions on Power Electronics*, 31(7):4720–4731.

Sousa, K. M., Dreyer, U. J., Martelli, C., & Cardozo da Silva, J. C. (2016). Dynamic eccentricity induced in induction motor detected by optical fiber bragg grating strain sensors. *IEEE Sensors Journal*, 16(12):4786–4792.

Stankevič, T., Medišauskas, L., Stankevič, V., Balevičius, S., Žurauskienė, N., Liebfried, O., & Schneider, M. (2014). Pulsed magnetic field measurement system based on colossal magnetoresistance-b-scalar sensors for railgun investigation. *Review of Scientific Instruments*, 85(4):044704.

Stankevič, T., Schneider, M., & Balevičius, S. (2013). Magnetic diffusion inside the rails of an electromagnetic launcher: Experimental and numerical studies. *IEEE Transactions on Plasma Science*, 41(10):2790–2795.

Tan, J. Y., Wang, K., Cao, R. W., & Lyu, G. (2018). Sensorless control of pmsm machine based on improved pll structure eliminating integral drift of third harmonic back-emf. In *2018 21st International Conference on Electrical Machines and Systems (ICEMS)* 1686–1690.

Tao, P., Wang, F., Mei, X., & Lin, J. (2017). Pll with piecewise judgement function for smo beased sensorless control of pmsm. In *2017 5th International Conference on Enterprise Systems (ES)* 190–194.

Tian, G., Yan, Y., Jun, W., Ru, Z. Y., & Peng, Z. X. (2018). Rotor position estimation of sensorless pmsm based on extented Kalman filter. In *2018 IEEE International Conference on Mechatronics, Robotics and Automation (ICMRA)* 12–16.

Tian, Z., Zhang, C., & Zhang, S. (2017). Analytical Calculation of Magnetic Field Distribution and Stator Iron Losses for Surface-Mounted Permanent Magnet Synchronous Machines. *Energies*, 10(3):320.

Turner, R. & Rasmussen, C. E. (2010). Model based learning of sigma points in unscented Kalman filtering. In *2010 IEEE International Workshop on Machine Learning for Signal Processing* 178–183.

Urresty, J.-C., Riba, J.-R., & Romeral, L. (2013). A back-emf based method to detect magnet failures in pmsms. *IEEE Transactions on Magnetics*, 49(1):591–598.

Ustun, O., Bayram, D., Durak, B., & Kivanc, O. C. (2017). Comparison of different line start interior permanent magnet synchronous motor types with respect to ie4 efficiency class. In *2017 18th International Symposium on Electromagnetic Fields in Mechatronics, Electrical and Electronic Engineering (ISEF) Book of Abstracts* 1–2.

Vaez-Zadeh, S. (2018). *Control of Permanent Magnet Synchronous Motors*. Oxford University Press, illustrated edition.

Vas, P. (1998). *Sensorless Vector and Direct Torque Control (Monographs in Electrical and Electronic Engineering, 42)*. Oxford University Press.

Vyšniauskas, G. (2021). Elektromobilio pavaros valdymo sistemos tyrimas. *Vilniaus Gedimino technikos universitetas*.

Wan, E. & Van Der Merwe, R. (2000). The unscented Kalman filter for nonlinear estimation. In *Proceedings of the IEEE 2000 Adaptive Systems for Signal Processing, Communications, and Control Symposium (Cat. No.00EX373)* 153–158.

Wang, G., Qu, L., Zhan, H., Xu, J., Ding, L., Zhang, G., & Xu, D. (2014). Self-commissioning of permanent magnet synchronous machine drives at standstill considering inverter nonlinearities. *IEEE Transactions on Power Electronics*, 29(12):6615–6627.

Wang, M., Xu, Y., & Zou, J. (2018). Sensorless control for pmsm connected with lc filter based on extended state observer. In *2018 21st International Conference on Electrical Machines and Systems (ICEMS)* 1644–1648.

Wang, Q., Wang, G., Liu, S., Zhang, G., & Xu, D. (2022). An inverter-nonlinearity-immune offline inductance identification method for pmsm drives based on equivalent impedance model. *IEEE Transactions on Power Electronics*, 37(6):7100–7112.

Wang, X., Li, Q., Wang, S., & Li, Q. (2003). Analytical calculation of air-gap magnetic field distribution and instantaneous characteristics of brushless dc motors. *IEEE Transactions on Energy Conversion*, 18(3):424–432.

Wu, L. & Zhu, Z.-Q. (2014). Analytical modeling of surface-mounted pm machines accounting for magnet shaping and varied magnet property distribution. *IEEE Transactions on Magnetics*, 50(7):1–11.

Wu, X., Fu, X., Lin, M., & Jia, L. (2019). Offline inductance identification of ipmsm with sequence-pulse injection. *IEEE Transactions on Industrial Informatics*, 15(11):6127–6135.

Xia, C., Ji, B., & Yan, Y. (2015). Smooth speed control for low-speed high-torque permanent-magnet synchronous motor using proportional–integral–resonant controller. *IEEE Transactions on Industrial Electronics*, 62(4):2123–2134.

Xiao, X., Chen, C., & Zhang, M. (2010). Dynamic permanent magnet flux estimation of permanent magnet synchronous machines. *IEEE Transactions on Applied Superconductivity*, 20(3):1085–1088.

Xu, J., Odavic, M., Zhu, Z., Wu, Z.-Y., & Freire, N. (2022). A novel space vector pwm technique with duty cycle optimization through zero vectors for dual three-phase pmsm. *IEEE Transactions on Energy Conversion* 1–1.

Yeh, H.-C. & Yang, S.-M. (2021). Phase inductance and rotor position estimation for sensorless permanent magnet synchronous machine drives at standstill. *IEEE Access*, 9:32897–32907.

Zamudio-Ramirez, I., Osornio-Rios, R. A., Antonino-Daviu, J. A., Razik, H., & Romero-Troncoso, R. d. J. (2022). Magnetic flux analysis for the condition monitoring of electric machines: A review. *IEEE Transactions on Industrial Informatics*, 18(5):2895–2908.

Zamudio-Ramírez, I., Osornio-Ríos, R. A., Antonino-Daviu, J. A., & Quijano-Lopez, A. (2020). Smart-sensor for the automatic detection of electromechanical faults in induction motors based on the transient stray flux analysis. *Sensors*, 20(5).

Zarko, D., Ban, D., & Lipo, T. (2006). Analytical calculation of magnetic field distribution in the slotted air-gap of a surface permanent-magnet motor using complex relative air gap permeance. *IEEE Transactions on Magnetics*, 42(7):1828–1837.

Zhang, Z., Jing, L., Wu, X., Xu, W., Liu, J., Lyu, G., & Fan, Z. (2021). A deadbeat pi controller with modified feedforward for pmsm under low carrier ratio. *IEEE Access*, 9:63463–63474.

Zhou, Y. & Xue, Z. (2021). Analytical method for calculating the magnetic field of spoke-type permanent magnet machines accounting for eccentric magnetic pole. *IEEE Transactions on Industrial Electronics*, 68(3):2096–2107.

Zhu, Z. & Howe, D. (1993a). Instantaneous magnetic field distribution in brushless permanent magnet dc motors. ii. armature-reaction field. *IEEE Transactions on Magnetics*, 29(1):136–142.

Zhu, Z. & Howe, D. (1993b). Instantaneous magnetic field distribution in brushless permanent magnet dc motors. iii. effect of stator slotting. *IEEE Transactions on Magnetics*, 29(1):143–151.

Zhu, Z., Howe, D., Bolte, E., & Ackermann, B. (1993). Instantaneous magnetic field distribution in brushless permanent magnet dc motors. i. open-circuit field. *IEEE Transactions on Magnetics*, 29(1):124–135.

Zhu, Z., Howe, D., & Chan, C. (2002). Improved analytical model for predicting the magnetic field distribution in brushless permanent-magnet machines. *IEEE Transactions on Magnetics*, 38(1):229–238.

Zhu, Z., Howe, D., & Xia, Z. (1994). Prediction of open-circuit airgap field distribution in brushless machines having an inset permanent magnet rotor topology. *IEEE Transactions on Magnetics*, 30(1):98–107.

Zhu, Z. Q., Wu, L. J., & Xia, Z. P. (2010). An accurate subdomain model for magnetic field computation in slotted surface-mounted permanent-magnet machines. *IEEE Transactions on Magnetics*, 46(4):1100–1115.

Žurauskienė, N., Balevičius, S., Stankevič, V., Keršulis, S., Schneider, M., Liebfried, O., Plaušinaitienė, V., & Abrutis, A. (2010). B-scalar sensor using cmr effect in thin polycrystalline manganite films. *IEEE Transactions on Plasma Science*, 39(1):411–416.

Žurauskienė, N., Stankevič, V., Keršulis, S., Klimantavičius, J., Šimkevičius, Č., Plaušinaitienė, V., Vagner, M., & Balevičius, S. (2019). Increase of operating temperature of magnetic field sensors based on la–sr–mn–o films with mn excess. *IEEE Transactions on Plasma Science*, 47(10).

List of Scientific Publications by the Author on the Topic of the Dissertation

Papers in the Reviewed Scientific Journals

Balevičius, S., Žurauskienė, N., Stankevič, V., Keršulis, S., Baškys, A., Bleizgys, V., Dilys, J., Lučinskis, A., Tyshko, A., & Brazil, S. (2020). Hand-held magnetic field meter based on colossal magnetoresistance B-Scalar sensor. *IEEE Transactions on Instrumentation and Measurement, 69*(6), 2808–2816. doi: 10.1109/TIM.2019.2925411

Dilys, J., Stankevič, V., & Łuksza, K. (2021). Implementation of extended Kalman filter with optimized execution time for sensorless control of a PMSM using ARM Cortex-M3 microcontroller. *Energies, 14*(12), 3491. doi: 10.3390/en14123491

Stankevič, V., Lueg-Althoff, J., Hahn, M., Tekkaya, A. E., Žurauskienė, N., Dilys, J., Klimantavičius, J., Keršulis, S., Šimkevičius, C., & Balevičius, S. (2020). Magnetic field measurements during magnetic pulse welding using CMR-B-Scalar sensors. *Sensors, 20*(20), 5925. doi: 10.3390/s20205925

Stankevič, V., Keršulis, S., Dilys, J., Bleizgys, V., Viliūnas, M., Vertelis, V., Maneikis, A., Rudokas, V., Plaušinaitienė, V., & Žurauskienė, N. (2023). Measurement system for short-pulsed magnetic fields. *Sensors, 23*(3), 1435. doi: 10.3390/s23031435

Papers in Other Editions

Dilys, J. (2020). Modeling of Sensorless Control of Permanent-magnet Synchronous Motors. In *2020 IEEE Open Conference of Electrical, Electronic and Information Sciences (eStream)*. IEEE. doi: 10.1109/eStream50540.2020.9108863

Dilys, J., & Baškys, A. (2017). Self-identification of permanent magnet synchronous motor inductance for efficient sensorless control. In *2017 Open Conference of Electrical, Electronic and Information Sciences (eStream)*. IEEE. doi: 10.1109/eStream.2017.7950306

Dilys, J., & Stankevic, V. (2022). A simple method for stator inductance and resistance estimation for PMSM at standstill. *International Journal of Robotics and Control Systems, 2*(3), 477–491. doi: 10.31763/ijrcs.v2i3.741

Summary in Lithuanian

Įvadas

Problemos formulavimas

Sinchroninių variklių su nuolatiniais magnetais (SVNM) valdymas yra sudėtingas dėl didelio parametrų netiesiškumo ir sudėtingo magnetinio ryšio tarp statoriaus ir rotoriaus. Be to, dėl variklio parametrų kitimo laike ši problema tampa dar rimtesnė. Paprastai laikoma, kad sinchroninio variklio su nuolatiniais magnetais statoriaus varža induktyvumai yra pastovūs laike. Tačiau, praktikoje šie parametrai kinta. Tikslūs sinchroninio variklio su nuolatiniais magnetais parametrai yra labai svarbūs siekiant užtikrinti variklio valdymo sistemos stabilumą, efektyvumą ir dinaminį atsaką. Per pastaruosius kelis dešimtmečius variklių parametrų įvertinimo metodai buvo intensyviai tobulinami, o parametrai gali būti įvertinami tiek dinaminiu tiek statiniu atveju. Todėl prieš projektuojant valdymo sistemą konkrečiam sinchroniniam varikliui su nuolatiniais magnetais visada labai svarbu atlikti valdymo sistemos tyrimą naudojant kompiuterinį modeliavimą. Daugumoje atvejų sinchroniniams varikliams su nuolatiniais magnetais modeliavimui naudojami supaprastinti matematiniai modeliai, kuriuose variklio parametrų vertės laikomos pastoviomis. Tokie variklių modeliai neįvertina netiesinių variklio charakteristikų, sukimo momento pulsacijų, induktyvumo pasiskirstymo, atgalinės elektromagnetinės jėgos ir kitų parametrų. Tik keliuose publikuotuose darbuose yra pasiūlyti matematiniai modeliai, įvertinantys anksčiau paminėtus reiškinius, tačiau šie modeliai paremti baigtinių elementų metodu, todėl naudojant juos sinchroninio variklio su nuolatiniais magnetais modeliavimo laikas tampa nepriimtinai ilgas.

Pagrindinė disertacijoje sprendžiama problema – idealus matematinis SVNM modelis

neatsižvelgia į tokius svarbius variklio reiškinius kaip sukimo momento pulsacijos, induktyvumo ir atgalinės elektrovaros pasiskirstymai.

Buvo iškelta hipotezė, kad patobulintas SVNM modelis, sukurtas naudojant analitinius magnetinio srauto tankio sprendinius, leidžia padidinti SVNM modelio tikslumą palyginti su idealiu SVNM modeliu.

Darbo aktualumas

Sinchroniniai varikliai su nuolatiniais magnetais yra populiarūs daugelyje sričių dėl šių jiems būdingų privalumų: aukšto efektyvumo; didelio sukimo momento ir svorio santykio; mažo dydžio ir t.t (Paitandi & Sengupta, 2020). Sinchroniniai varikliai su nuolatiniais magnetais yra plačiai naudojami elektromobiliuose ir kituose elektra varomose transporto priemonėse, pramonėje, kosmonautikoje, buitiniuose prietaisuose, informacinėje ir biuro įrangoje. Daugelyje sinchroninių variklių su nuolatiniais magnetais taikymų ir ypač kai nuolat kinta variklio mechaninė apkrova, yra svarbu tiksliai, realiuoju laiku valdyti į statorių tiekiamos kintamosios trifazės įtampos, kurią generuoja inverteris, parametrus.

Kuriant sinchroninio variklio su nuolatiniais magnetais valdymo sistemas svarbų vaidmenį atlieka tokių sistemų kompiuterinis modeliavimas. Todėl kurti naujus, tikslesnius sinchroninio variklio su nuolatiniais magnetais matematinius modelius yra aktualu, nes tai leidžia gauti patikimesnius modeliavimo rezultatus.

Kadangi modeliavimo patikimumas priklauso ne tik nuo modelio, bet ir nuo modelyje naudojamų parametrų verčių, todėl taip pat aktualu yra kurti sinchroninio variklio su nuolatiniais magnetais matematinių modelių parametrų nustatymo metodus, leidžiančius tiksliai ir patogiai tuos parametrus nustatyti.

Tyrimų objektas

Tyrimo objektas – sinchroninis variklis su nuolatiniais magnetais.

Darbo tikslas

Disertacijos tikslas – sukurti sinchroninio variklio su nuolatiniais magnetais analitinį matematinį modelį, kuris įvertintų sukimo momento pulsacijas, statoriaus induktyvumo pasiskirstymą bei elektrovaros formą, sukurti magnetinio lauko tankio matavimo sistemas ir pasiūlyti variklio parametrų nustatymo metodą.

Darbo uždaviniai

Siekiant išspręsti iškeltą problemą ir pasiekti darbo tikslą, suformuluoti tokie uždaviniai:

1. Sukurti sinchroninio variklio su nuolatiniais magnetais matematinį modelį, pagrįstą analitinėmis magnetinio srauto tankio lygtimis.
2. Sukurti sinchroninio variklio su nuolatiniais magnetais vektorinio valdymo metodą ir atlikti eksperimentinius tyrimus.
3. Sukurti sinchroninio variklio su nuolatiniais magnetais elektrinių parametrų nustatymo metodą.

4. Suprojektuoti magnetinio srauto tankio matavimo sistemas, skirtas magnetinio srauto tankiui matuoti variklyje.

5. Eksperimentiškai ištirti magnetinio srauto tankio pereinamuosius procesus naudojant sukurtas magnetinio srauto tankio matavimo sistemas.

Tyrimų metodika

Darbe yra taikomi teorinės analizės metodai, modeliavimas bei eksperimentiniai tyrimai. Kompiuterinis modeliavimas atliktas naudojant MATLAB programinę įrangą. Eksperimentiniams tyrimams buvo sukurti trys įterptinių sistemų įrenginiai, įskaitant aparatinę ir programinę įrangą. Pirmieji du įrenginiai skirti magnetinio srauto tankio matavimui, realizuoti panaudojant ARM tipo mikrovaldiklį LPC54619. Trečiasis įrenginys, skirtas SVNM valdymui, sukurtas panaudojant ARM tipo mikrovaldiklį LPC1549. Visiems minėtiems įrenginiams buvo sukurta asmeninio kompiuterio pagalbinė programinė įranga, skirta duomenų nuskaitymui ir perdavimui į asmeninį kompiuterį.

Darbo mokslinis naujumas

1. Sukurtas naujas sinchroninio variklio su nuolatiniais magnetais matematinis modelis, paremtas analitinėmis matematinėmis išraiškomis, įvertinantis sukimo momento pulsacijas, statoriaus induktyvumo pasiskirstymą ir elektrovaros formą.

2. Sukurta nauja išplėstinio Kalmano filtro modifikacija leidžianti sutrumpinti skaičiavimo laiką, nustatant rotoriaus padėtį.

3. Pasiūlytas naujas sinchroninio variklio su nuolatiniais magnetais statoriaus varžos ir induktyvumo įvertinimo metodas, esant rotoriui ramybės būsenos.

4. Sukurtos magnetinio srauto tankio matavimo sistemos, leidžiančios matuoti magnetinio lauko pereinamuosius procesus sinchroniniame variklyje ir įvertinti patobulinto SVNM modelio tikslumą.

Darbo rezultatų praktinė reikšmė

Sukurtas modelis, įvertinantis sukimo momento pulsacijas, statoriaus induktyvumo pasiskirstymą ir elektrovaros formą leis atlikti tikslesnį variklio modeliavimą. Taip pat, sukurtos magnetinio srauto tankio matavimo sistemos gali būti naudojamos ne tik variklio magnetinio srauto tankio pereinamiesiems procesams matuoti, bet ir kitose pramonės ir mokslo srityse, kur būtina tirti nežinomos arba besikeičiančios krypties magnetinį lauką mažame tūryje.

Šioje disertacijoje pristatyti tyrimo rezultatai taip pat buvo panaudoti vykdant Lietuvos mokslo tarybos projektą – „Spartūs magnetovaržiniai procesai nanostruktūrizuotų manganitų sluoksnių jutikliuose, skirtuose elektromagnetinio formavimo įtaisų monitoringui“, MIP-17-470 (2017 – 2020).

Ginamieji teiginiai

Daktaro disertacijos ginamieji teiginiai yra šie:

1. Sukurtas naujas sinchroninio variklio su nuolatiniais magnetais matematinis modelis, naudojantis analitines matematines išraiškas įvertina sukimo momento pulsacijas, statoriaus induktyvumo pasiskirstymą ir elektrovaros formą.
2. Sukurta išplėstinio Kalmano filtro modifikacija rotoriaus padėčiai nustatyti leidžia tris kartus sutrumpinti skaičiavimo trukmę lyginant su klasikiniu Kalmano filtru, atskiriant variacijos matricų skaičiavimą nuo viso algoritmo.
3. Sinchroninio variklio su nuolatiniais magnetais statoriaus varža ir induktyvumas, esant rotoriui ramybės būsenos, gali būti nustatyti naudojant tris 20 μs trukmės įtampos impulsus bei matuojant statoriaus sroves.
4. Sukurtos magnetinio srauto tankio matavimo sistemos, leidžia matuoti magnetinio srauto tankį variklio oro tarpe, nepriklausomai nuo magnetinio lauko krypties.

Darbo rezultatų aprobavimas

Pagrindiniai disertacijos rezultatai paskelbti 7 mokslinėse publikacijose: 4 iš jų buvo išspausdintos recenzuojamuose mokslo žurnaluose, įtrauktuose į *Clarivate Analytics Web of Science* sąrašą ir turinčiuose citavimo rodiklį, 3 kitose duomenų bazėse. Rezultatai buvo pristatyti 8 mokslinėse konferencijose.

Disertacijos tematikai skirti tyrimo rezultatai buvo pristatyti aštuoniose mokslinėse konferencijose:

- Tarptautinė konferencija apie automatizavimą ir valdymą „International Conference on Automation and Control Engineering“, 2022 m. vasario 15 – 16 d., Londonas, Jungtinė Karalystė.
- 65-oji tarptautinė fizikos bei gamtos mokslų studentų konferencija „Open Readings“, 2022 m., Vilnius, Lietuva.
- 11-oji fizinių ir technologijos mokslų centro doktorantų ir jaunųjų mokslininkų konferencija „FizTech2021“, 2021 m., Vilnius, Lietuva.
- 9-oji fizinių ir technologijos mokslų centro doktorantų ir jaunųjų mokslininkų konferencija „FizTech2019“, 2019 m., Vilnius, Lietuva.
- Tarptautinė konferencija „Open Conference of Electrical, Electronic and Information Science (eStream)“, 2020 m., Vilnius, Lietuva.
- Tarptautinė konferencija „Open Conference of Electrical, Electronic and Information Science (eStream)“, 2017 m., Vilnius, Lietuva.
- 20-oji Lietuvos jaunųjų mokslininkų konferencija „Mokslas – Lietuvos ateitis“, 2017 m., Vilnius, Lietuva.
- 22-oji Lietuvos jaunųjų mokslininkų konferencija „Mokslas – Lietuvos ateitis“, 2019 m., Vilnius, Lietuva.

Padėka

Aš išreiškiu didžiausią padėką prof. dr. Voitech Stankevič ir prof. dr. Algirdui Baškiui už puikų vadovavimą, rūpestį, kantrybę, entuziazmą ir puikia mokslinę aplinką. Ypatingą padėką skiriu habil. dr. Marcin Morawiec už paramą terminologijoje ir pasidalinima žiniomis, ir prof. habil. dr. Jarosław Guziński ir jo komandai už kvietimą į Gdansko technologijos universitetą.

Taip pat dėkoju prof. dr. Jurijui Novickiui ir prof. dr. Daliui Navakauskui už jų recenzijas ir daugybę pastabų bei pasiūlymų, kurios labai padėjo pagerinti šio darbo kokybę.

Disertacijos struktūra

Disertaciją sudaro: įvadas, trys skyriai, bendrosios išvados, literatūros sąrašas su atskirai pateiktomis autoriaus publikacijomis ir trys priedai. Darbo apimtis yra 137 puslapių, kuriuose yra pateikta: 108 formulių, 87 paveikslai ir 14 lentelių. Disertacijoje remtasi 140 kitų autorių literatūros šaltinių.

1. Sinchroninio variklio su nuolatiniais magnetais veikimo principo apžvalga

Šiame skyriuje apžvelgiama sinchroninių variklių su nuolatiniais magnetais (SVNM) konstrukcija ir klasifikavimas. Taip pat skyriaus pradžioje trumpai aptariamas SVNM matematinis modelis, įvairūs rotoriaus greičio ir padėties nustatymo algoritmai bei aptariami SVNM parametrų įvertinimo metodai. Galiausiai pateikiamas dvimatis magnetinio lauko analitinis modelis, taip pat aptariama SVNM statoriaus armatūros ir rotoriaus magnetinio lauko teorija. Sinchroniniai varikliai su nuolatiniais magnetais yra bešepetėliniai didelio patikimumo ir efektyvumo varikliai. Lyginant su asinchroniniais indukciniais varikliais, SVNM dėl rotoriuje naudojamų nuolatinių magnetų turi didesnį efektyvumą, sukimo momentą ir mažesnį svorį. Pagal nuolatinių magnetų išdėstymą rotorius galima suskirstyti į rotorius su lanko formos magnetais, sumontuotais paviršiuje, arba su magnetais, įmontuotais į plieninį cilindrą, o statoriaus konstrukcija yra tokia pati kaip asinchroninių indukcinių variklių. Paviršinio montavimo magnetai gali būti įmagnetinami radialiai arba lygiagrečiai. Radialinis magnetų įmagnetinimas yra dažniausiai naudojamas didelio greičio pavarose. Skirtingas nuolatinių magnetų įmagnetinimas sukuria variklio sistemoje skirtingą magnetinio lauko pasiskirstymą, o tai gali veikti variklio charakteristikas. Todėl, norint gauti tinkamas variklio charakteristikas, būtina atlikti tyrimą, kaip nuolatinių magnetų magnetinio lauko konfigūracija veikia variklio parametrus.

Siekiant padidinti variklių efektyvumą, reikia turėti informaciją apie rotoriaus padėtį ir jo greitį tam, kad per grįžtamąjį ryšį atitinkamai galima būtų valdyti tiekiamos į variklį kintamosios įtampos parametrus. Kartais tam yra naudojami jutikliai, kurie matuoja rotoriaus padėtį. Valdymo sistemose, kuriose nenaudojami jutikliai, rotoriaus padėčiai nustatyti yra naudojamas išplėstinis Kalmano filtras (EKF). Matematinis Kalmano filtras yra modelis, kuris veikia kartu su valdymo sistema ir yra dažniausiai naudojamai nežinomos sistemos būsenai nustatyti. Skirtumas tarp išmatuotų ir apskaičiuotų parametrų yra naudojamas variklio valdymui koreguoti per grįžtamąjį ryšį. Grįžtamojo ryšio koeficientas

yra apskaičiuojamas taip, kad būsenos įvertis būtų optimalus. Rotoriaus padėčiai ir greičiui nustatyti naudojant išplėstinį Kalmano filtrą yra matuojamos tik statoriaus srovės, o statoriaus įtampos yra nustatomos iš įtampos impulsų pločio moduliacijos parametrų.

Sinchroniniams varikliams maitinti yra naudojami inverteriai kurie nuolatinę maitinimo įtampą paverčia į kintamąją naudojant tranzistorinius raktus ir taikant erdvinio vektoriaus impulsų pločio moduliaciją. Priešingai nuo sinusinės impulsų pločio moduliacijos, kai visi raktai komutuojami vienu metu, vektorinio valdymo srityje naudojama komutacija tarp kelių, iš anksto pasirinktų inverterio būsenų, iš kurių kiekviena atitinka tam tikrą įtampos vektoriaus erdvinę padėtį. Todėl gauname valdomą erdvinį vektorių su pastoviu kampiniu dažniu. Pagrindinis vektorinio valdymo metodo tikslas yra valdyti statoriaus magnetinį lauką nepriklausomai nuo rotoriaus magnetinio lauko. Vektoriniam valdymui įgyvendinti naudojama variklio modelio parametrų ir kintamųjų transformacija iš įprastinės stacionarios abc atskaitos sistemos į dvimatę dq koordinačių sistemą.SVNM sukimo momentas valdomas kontroliuojant statoriaus srovės vektorių. Tokio metodo privalumai yra reikiamo sukimo momento palaikymas, greitas reagavimas į mechaninės apkrovos pokyčius ir tikslus greičio reguliavimas. Sukurto sinchroninio variklio su pastoviaisiais magnetais matematiniam modeliui patikriniti būtina atlikti tiesioginius magnetinio lauko matavimus. Tokiems matavimams dažniausia yra naudojami Holo arba kilpiniai jutikliai. Tačiau, tokio tipo jutikliai turi vieną esminį trūkumą – jie yra jautrūs magnetinio lauko krypčiai. Todėl, sukurto matematinio modelio patikrai reikalingi kitokie jutikliai, kurie galėtu išmatuoti magnetinį lauką siaurame tarpe tarp rotoriaus ir statoriaus, o jų signalas nepriklausytu nuo magnetinio lauko krypties.

Atlikus literatūros apžvalgą buvo padarytos tokios išvados:

1. Sinchroninių variklių su nuolatiniais magnetais tikslus parametrų (statoriaus varžos, statoriaus induktyvumo, rotoriaus greičio ir padėties) įvertinimas yra labai svarbus siekiant pagerinti variklio valdymo našumą ir eksploatacinį patikimumą.
2. Variklio dinaminiai modeliai yra pagrįsti baigtiniu elementų metodu, todėl skaičiavimo laikas naudojant tokius modelius yra ilgas. Skaičiavimo laiką galima sutrumpinti naudojant analitinėmis lygtimis pagrįstus variklio modelius.
3. Sinchroninio variklio su nuolatiniais magnetais dvimačiui magnetinio lauko pasiskirstymui apskaičiuoti galima taikyti Furjė teoriją.
4. Atsižvelgti į statoriaus plyšelių įtaką - įvedama santykinės skvarbos sąvoką, kuri leidžia patikslinti analitinius magnetinio lauko sprendinius.
5. Magnetinio lauko jutikliai reikalingi tiesioginiam magnetinio lauko varikliuose matavimui ir modeliavimo patikimumui įvertinti. Tačiau šiuo metu žinomi jutikliai nėra tinkami tokiems matavimams.

2. Sinchroninių variklių su nuolatiniais magnetais modeliavimas ir simuliavimas naudojant analitines magnetinio lauko išraiškas

Antrajame skyriuje pateikiami analitiniai sprendiniai, kurie yra naudojami magnetiniam srauto tankiui SVNM oro tarpe ir apvijose skaičiuoti. Pirmiausia yra skaičiuojamas roto-

riaus sukurtas magnetinis laukas. Po to pateikiami magnetinio srauto tankio, kurio šaltinis yra variklio statoriaus apvijos, sprendiniai. Paskui yra įvertinama statoriaus izoliacinių griovelių tarpų įtaka magnetinio srauto tankiui. Žinant magnetinio srauto tankį duotu laiko momentu yra apskaičiuojami variklio išvestiniai parametrai: induktyvumai, magnetinio srauto pastovioji, jėgos momentas ir pulsacijos momentas. Gauti parametrai yra naudojami diferencialinių lygčių sprendimuose, kuriant variklio matematinį modelį. Reikia pabrėžti, kad klasikiniame SVNM modelyje laikomasi prielaidos, kad šie parametrai yra nekintantys. Sudarytas matematinis SVNM modelis įgyvendintas Matlab programinėje aplinkoje.

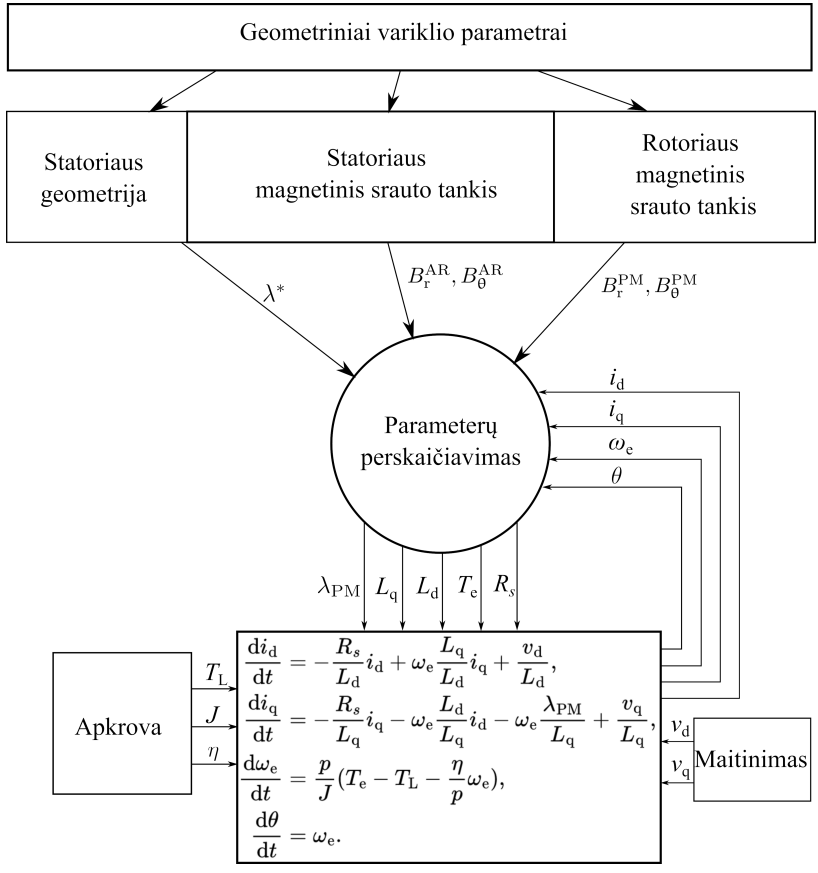

S2.1 pav. Patobulinto sinchroninio variklio su nuolatiniais magnetais modelio parametrų diagrama

Analizuojant literatūrą galima surasti daug sprendimo metodų, paremtų analitinėmis išraiškomis, skaičiuojant SVNM magnetinį lauką. Tačiau dauguma iš jų yra pritaikyti konkrečiai variklio konstrukcijai ir variklio parametrams. Be to skaičiavimo tikslumas ir skaičiavimo vykdymo laikas nėra tinkami. Šitame darbe pasiūlytas alternatyvus SVNM

modelis, paremtas analitinėmis išraiškomis, jame atskiros variklio modelio dedamosios (statoriaus geometrija, statoriaus magnetinis laukas ir rotoriaus magnetinis laukas) yra skaičiuojamos atskirai. Toks atskyrimas leidžia supaprastinti modeliavimą ir pagreitinti skaičiavimą. Atskyrimo principas parodytas S2.1 pav. Rodyklėms parodyta, kaip vyksta duomenų srautų perdavimas ir ryšys tarp jų. Dėl tokio atskyrimo kiekvienas analitinis sprendimo rezultatas yra atskirtas nuo kitų ir todėl labai greitai ir lengvai gali būti pakeistas kitu analitiniu sprendiniu. Bendri variklio parametrai (pavyzdžiui induktyvumas) skaičiuojami atskirai ir nepriklauso nuo konkretaus analitinio sprendimo metodo.

S2.1 lentelė. Sinchroninio variklio su nuolatiniais magnetais modelio parametrai

Parametras	Simbolis	Vertė
Polių porų skaičius	p	4
Statoriaus griovelių skaičius	Q_s	6
Magnetų spindulys	R_m	59,5 mm
Statoriaus vidinis spindulys	R_s	60,5 mm
Rotoriaus paviršiaus spindulys	R_r	46,5 mm
Ašinis ilgis	L	75,6 mm
Apvijų žingsnio kampas	α_y	1,0472 rad
Įmagnetinimas	B_R	1,0 T
Santykinė skvarba	μ_r	1,05
Magneto užimtumo santykis	α_p	0,85
Apvijų skaičius	N_s	15
Griovelio tarpo plotis	b_0	2 mm
Apvijų storis	h_w	3,5 mm
Ritės žingsnio kampas	θ_c	3,14 rad
Išsiplėtimo kampas	λ_c	0,2094 rad
Apkrova	T_L	20 Nm
Trinties koeficientas	η	0,005 rad
Inercijos momentas	J	0,01 kgm^2

Parametrai, kurie buvo naudojami atliekant variklio su nuolatiniais magnetais sumontuotais rotoriaus paviršiuje modeliavimą pateikti S2.1 lentelėje. Pirmiausia buvo skaičiuojamas statoriaus magnetinis srauto tankis neįvertinant statoriaus griovelių įtakos. Po to buvo atlikti skaičiavimai įvertinus statoriaus griovelių įtaką magnetinio lauko pasiskirstymui.

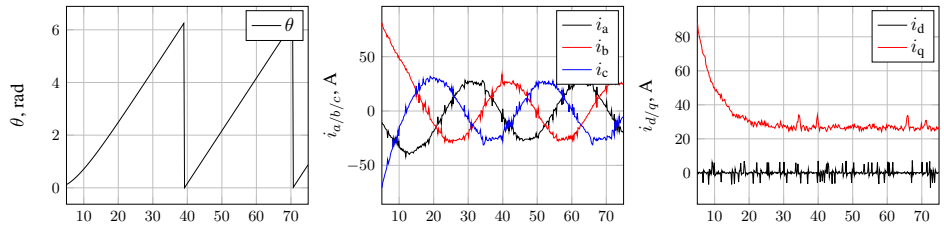

S2.2 pav. Vektorinio valdymo su patobulinto sinchroninio variklio ir paviršiuje montuojamais magnetais rezultatai: (a) rotoriaus padėtis; (b) stacionarios statoriaus srovės; (c) dinaminės statoriaus srovės

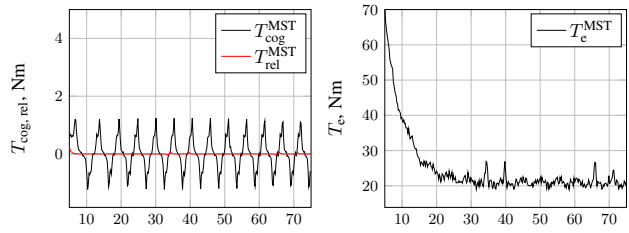

S2.3 pav. Vektorinio valdymo su patobulinto sinchroninio variklio ir paviršiuje montuojamais magnetais rezultatai: (a) vibracijų momentas; (b) elektrinis jėgos momentas

Variklio sukimo momento, fazinių srovių ir statoriaus srovės vektoriaus dedamosios i_q ir i_d modeliavimo rezultatai pateikti S2.2 pav. ir S2.3 pav. parodyti sukimo momento, o S2.4 pav. induktyvumo, magnetinio srauto ir elektrovaros skaičiavimo rezultatai. Skaičiavimai buvo atlikti, kai atraminis kampinis sukimosi greitis lygus $w_e^* = 200$ rad/s. Be to, iš S2.4 pav. a, matome, kad šiam atvejui induktyvumo projekcijos į d- ir q-ašį yra beveik vienodos ($L_d \approx L_q$), todėl pasipriešinimo sukimo momentas (T_{rel}) yra artimas nuliui. Tačiau skaičiavimo rezultatai, kuriuose įvertinami statoriaus grioveliai, parodė, kad sukimo momento pulsacijų momentas nėra lygus nuliui ir svyruoja su sinchroninių dažnių (S2.3 pav. a). Tai patvirtina teoriją, kad sukimo momento pulsacijos nepriklauso nuo statoriaus apvijų srovės ir atsiranda tik dėl variklio konstrukcijos. Be to, iš S2.3 pav., a, ir S2.2 pav., a, galime padaryti išvadą, kad sukimo momento pulsacijos osciliuoja šešis kartus per vieną elektrinio rotoriaus ciklą ir sutampa su teoriškai apskaičiuotu periodu ($\theta_{cog} = \frac{2\pi}{\text{lcm}(2p,Q_s)}$).

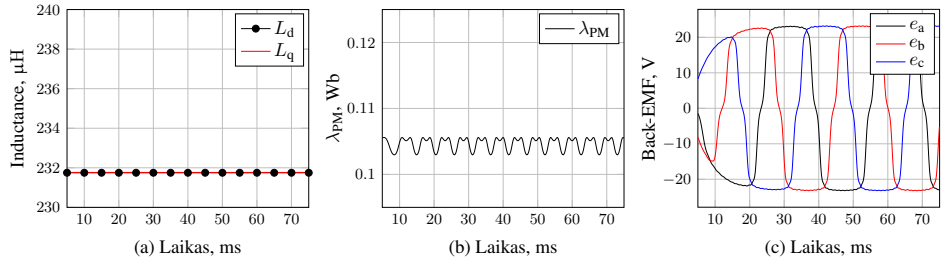

S2.4 pav. Vektorinio valdymo su patobulinto sinchroninio variklio ir paviršiuje montuojamais magnetais rezultatai: (a) induktyvumas; (b) magnetinis srautas; (c) atgalinė įtampa (elektrtovara)

Taip pat skaičiavimai parodė, kad veikiant varikliui magnetinio srauto ryšio konstantos (λ_{PM}) laike nesikeičia (S2.4 pav., b), o trijų fazių atgalinė įtampa turi trapecijos formą (S2.4 pav., c), S2.5 pav., a, ir S2.5 pav., b, parodyti rotoriaus ir statoriaus magnetinio srauto tankio skaičiavimo rezultatai. Kaip matome, magnetinio srauto tankis priklauso nuo rotoriaus padėties (α) ir nuo matavimo padėties (θ_r).

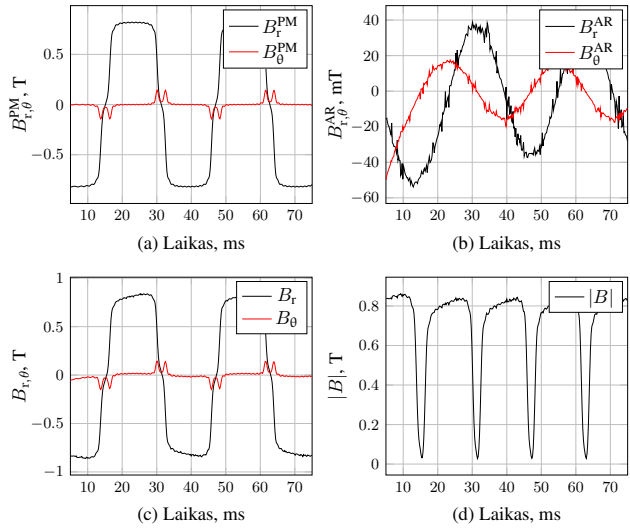

S2.5 pav. Valdymo su patobulinto sinchroninio variklio ir paviršiuje montuojamais magnetais rezultatai: (a) rotoriaus magnetinis srauto tankis; (b) statoriaus magnetinis srauto tankis; (c) suminis magnetinis srauto tankis; (d) magnetinio tankio absoliučioji vertė

Magnetinio srauto tankio priklausomybei nuo rotoriaus padėties įvertini pasirenkama magnetinio lauko nulinė matavimo pozicija ($\theta = 0$). Suminis statoriaus ir rotoriaus magnetinio srauto tankis ($|B| = \sqrt{B_r^2 + B_\theta^2}$) parodytas S2.5 pav., c. Matome, kad suminis srautas beveik atkartoja rotoriaus magnetinį lauką. Tai įvyksta dėl to, kad statoriaus apvijų magnetinis laukas yra daug mažesnis už rotoriaus magnetinį lauką. Be to, matome (S2.5 pav., a, ir S2.5 pav., b), kad statoriaus magnetinis laukas atsilieka nuo rotoriaus maždaug $\pi/2$ kampu. Tokia laukų padėtis yra pasiekiama vektorinio valdymo metodu. Esant tokiam kampui yra pasiekiamas maksimalus jėgos momentas ir optimalus valdymas. Absoliučioji suminio magnetinio srauto tankio vertės priklausomybė parodyta S2.5 pav., c. Apibendrinant gautus tyrimų rezultatus, galima padaryti išvadas, kad patobulintas sinchroninio variklio su nuolatiniais magnetais matematinis modelis leidžia apskaičiuoti variklio elektromagnetinį momentą, sukimo ir pasipriešinimo momentus, induktyvumus ir elektrovaromąją jėgą žinant tik variklio geometrinius parametrus ir rotoriaus padėtį. Be to, patobulintas išplėstinio Kalmano filtro algoritmas leidžia sutrumpinti skaičiavimo laiką, atskirai skaičiuojant variklio valdymą ir variklio parametrus. Valdymo procedūra valdo kiekvieną SVNM perjungimo periodą ir koreguoja naują magnetinio lauko vektoriaus būseną.

3. Eksperimentiniai sinhroninio variklio su nuolatiniais magnetais valdymo sistemų ir parametrų nustatymo tyrimai

Šiame skyriuje aprašoma eksperimentinė sąranka ir eksperimentinio tyrimo rezultatai.

Struktūrinė laboratorinio stendo schema parodyta S3.1 pav. Stendą sudaro sinchroninis variklis su nuolatiniais magnetais ir nuolatinės įtampos variklis kuris yra naudojamas kaip mechaninė valdomo variklio apkrova. Sinchroninis variklis su nuolatiniais magnetais yra maitinamas keitikliu, formuojančiu trifazę įtampą suformuotą taikant erdvinio vektoriaus impulsų pločio moduliaciją. Įtampos formavimo procesą valdo specialiai sukurta įterptinė sistema, realizuota naudojant mikrovaldiklį LPC1549. Keitiklis maitinamas iš nuolatinės įtampos maitinimo šaltinio, o kintamajai įtampai formuoti keitiklio inverteryje panaudoti lauko tranzistoriai.

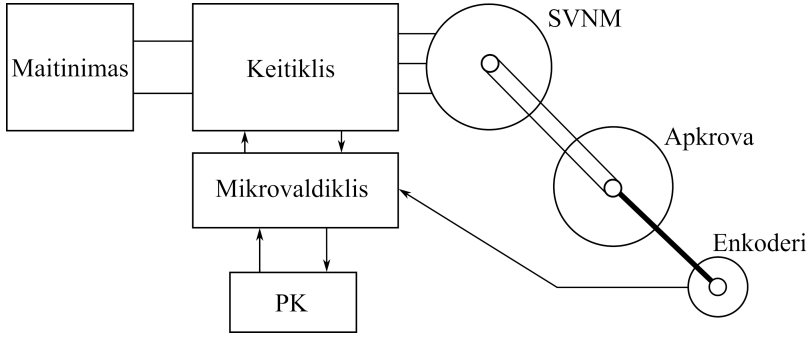

S3.1 pav. Eksperimentinės sistemos konfigūracija

Sinchroninio variklio su nuolatiniais magnetais statoriaus varža ir induktyvumas yra įvertinami esant rotoriui ramybės būsenos, naudojant tris trumpus stačiakampio formos įtampos impulsus kurie yra sukuriami trifazio keitiklio. Tuomet trijų fazių stacionariosios srovės i_{a}, i_{b} ir i_{c} yra matuojamos naudojant rezistorinius jutiklius. Dviejų fazių dinaminės srovės i_{d} ir i_{q} apskaičiuojamos pagal stacionariąsias fazines sroves, įvertinus rotoriaus padėtį. Rotoriaus padėtis yra įvertinama iš srovių: i_{a}, i_{b} ir i_{c} pikinių verčių. Tuomet statoriaus induktyvumai yra įvertinami iš srovės išvestinių pagal laiką. Toliau yra įvertinamas laikas, per kiek statoriaus srovės eksponentiškai gesta, ir apskaičiuojama statoriaus varža. Tam yra matuojamos statoriaus srovės, kai yra atjungiami visi keitiklio raktai. Metodas buvo patikrintas atliekant modeliavimus ir eksperimentinius tyrimus. Eksperimentai buvo atlikti su dviem skirtingais tipo varikliais, buvo gautas geras modeliavimo ir eksperimentinių rezultatų atitikimas. Be to, pasiūlytas metodas yra gana paprastas ir leidžia nustatyti statoriaus varžą ir induktyvumus, esant bet kokiai variklio mechaninei apkrovai. Palyginti su esamais parametrų įvertinimo metodais, siūlomas metodas yra greitesnis, lengvai įgyvendinamas praktiškai, o įvertinimo procesui nereikia didelių skaičiavimo resursų.

Magnetiniam laukui matuoti buvo sukurtos dvi matavimo sistemos. Pirmoji iš jų skirta matuoti impulsinį magnetinį lauką, kurio impulsų trukmė ne mažesnė nei šimtas mikrosekundžių, o likusi skirta trumpiems impulsiniems magnetiniams laukams matuoti. Visose sistemose buvo naudojamas magnetinio lauko CMR B skaliarinis jutiklis pagamintas iš plonų polikristalinių manganitų sluoksnio. Pirmos magnetinio lauko matavimo sistemos modulis parodytas S3.2 pav., a, o antrosios S3.2 pav., b. Sistema skirta magnetiniam laukui matuoti esant elektromagnetiniams trikdžiams. Norint apsaugoti matavimo sistemą nuo elektromagnetinių trikdžių, elektrinė grandinė buvo padėta į 4 mm storio plieninę

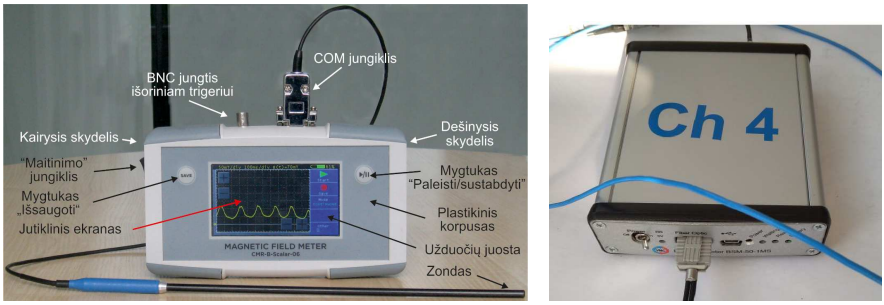

(a) (b)

S3.2 pav. Magnetinio srauto tankio matavimo sistemų vaizdai: (a) mobili matavimo sistema; (b) trumpiems impulsiniams magnetiniams laukams skirta matavimo sistema

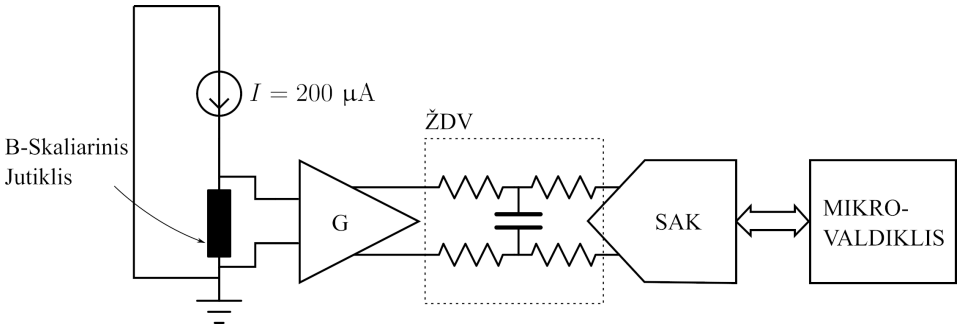

S3.3 pav. Principinė matavimo sistemos schema su CMR B skaliariniu jutikliu

dėžutę. Jutikliai pagaminti iš manganitų sluoksnių veikia magnetovaržiniu principu ir turi neigiamą magnetovaržą. Tai reiškia, kad tokių jutiklių varža mažėja stiprėjant magnetiniam laukui. Jutiklis yra maitinamas nuolatine 200/400 μA srove, su tiksliai išlaikoma verte. Žemųjų dažnių filtras skirtas aukštadažniams trikdžiams slopinti (S3.3 pav.).

Analoginis manganitų sluoksnių jutiklių signalas yra skaitmeninamas panaudojant 16 skilčių analogas-skaičius keitiklį, esant 25 MHz diskretizavimo dažniui. Sukurta impulsinio magnetinio lauko matavimo sistema geba matuoti magnetinį lauką dažnių diapazonuose nuo nulio iki 100 kHz, esant ne mažesnei kaip 10 mT magnetinio srauto vertės skiriamajai gebai. Šios matuoklio charakteristikos leidžia atlikti kelių šimtų mikrosekundžių trukmės magnetinio lauko impulsų matavimus. Išmatuotas signalas yra apdorojamas ir įrašomas į modulio pastoviąją atmintį. Tuomet įrašytas signalas perduodamas į asmeninį kompiuterį šviesolaidiniu ryšiu. Ryšiui su magnetinio lauko matavimo moduliu palaikyti buvo sukurta asmeninio kompiuterio programa. Kompiuterio programai buvo naudojama „Visual Studio 2010" programavimo aplinka. Programos pagrindinė užduotis yra išmatuoti ir vizualizuoti matuojamą magnetinį lauką. Taip pat programinė įranga naudojama keisti matuoklio nustatymus bei įrašyti jutiklių kalibravimo duomenis. Matavimo sistema leidžia pasirinkti matavimo proceso paleidimo (trigerio) šaltinį (nuo vidinio arba išorinio

trigerio).

Kitas sukurtas ir pagamintas magnetinio lauko matuoklis yra nešiojamo tipo. Jo veikimo principas ir pagrindinė struktūra panaši į pirmojo matuoklio. Tačiau jis turi nuosavą liečiamą ekraną ir jam valdyti nereikalingas kompiuteris. Matuoklis įdėtas į plastikinį korpusą. Kiekvieno jutiklio kalibravimo duomenys yra įrašyti į EEPROM lustą, kuris yra įmontuotas jutiklio jungtyje, todėl keičiant jutiklį, matuoklis jį atpažįsta ir matavimo metu naudoja šiam jutikliui skirtus kalibravimo duomenis. Temperatūrai matuoti yra naudojamas Pt1000 jutiklis ir TEMOD-I2C-R333 blokas, kuris konvertuoja jutiklio varžos pokytį į įtampos ir verčia jį į skaitmeninį I2C sąsajos standarto signalą. Išmatuoti magnetinio lauko duomenys yra įrašomi į Mikro-CD kortelę.

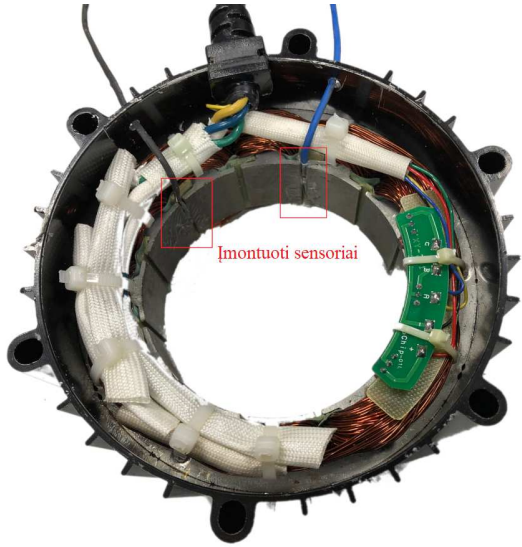

S3.4 pav. Įmontuoti skaliariniai magnetinio srauto tankio jutikliai, nukreipti į statoriaus korpusą

Naudojant sukurtus matuoklius buvo atlikti magnetinio lauko matavimai dviejuose vienodos konstrukcijos 800 W sinchroniniuose varikliuose. Dėl labai mažo oro tarpo tarp rotoriaus ir statoriaus (apie 0,5 mm) magnetinio lauko jutikliai buvo įmontuoti į statoriaus griovelį. Magnetinio lauko jutiklio padėtis parodyta S3.4 pav. Matavimo metu variklis buvo valdomas tam tikslui pagamintu keitikliu, o rotorius buvo neapkraunamas siekiant kuo labiau sumažinti statoriaus magnetinį lauką. Magnetinio srauto tankio matavimo oro tarpelyje rezultatai pateikti S3.5 pav. Analizuojant gautus rezultatus galima matyti, kad visų magnetinio lauko impulsų forma skirtinga ir pasikartoja kas aštuntame impulse. Kadangi šis variklis turi aštuonis polius, tai galime padaryti išvadą, kad kiekvienas impulsas atvaizduoja atskirų polių magnetinio srauto tankį. Palyginus tarpusavyje kiekvieno polio magnetinio lauko formą galima daryti prielaidą, kad visų magnetų įmagnetinimas yra skirtingas. Toks polių magnetinio lauko išbarstymas galbūt atsiranda gamybos procese, dėl neidealių sąlygų arba dėl jų eksploatavimo sąlygų. Tačiau kaip šie magnetai įmagnetinti

(radialiai ar lygiagrečiai), vien tik iš grafiko nustatyti negalima. Esant neapkrautam varikliui, pamatuotas magnetinis srauto tankis yra sukuriamas tik rotoriaus magnetinio srauto, nes statoriaus magnetinis laukas yra mažas.

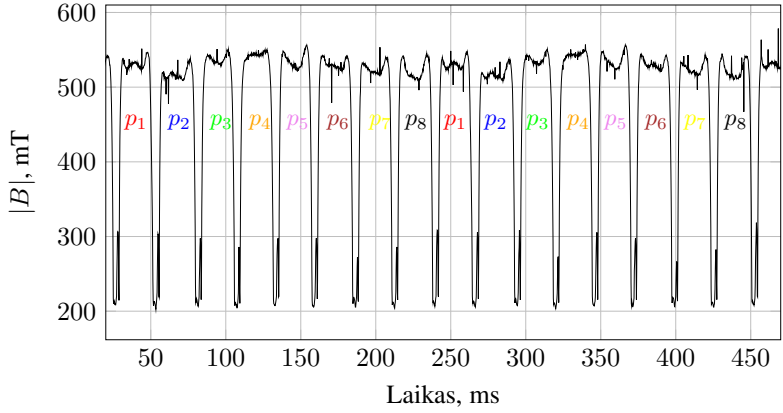

S3.5 pav. Išmatuoto magnetinio srauto tankio absoliučiosios vertės priklausomybė nuo rotoriaus padėties

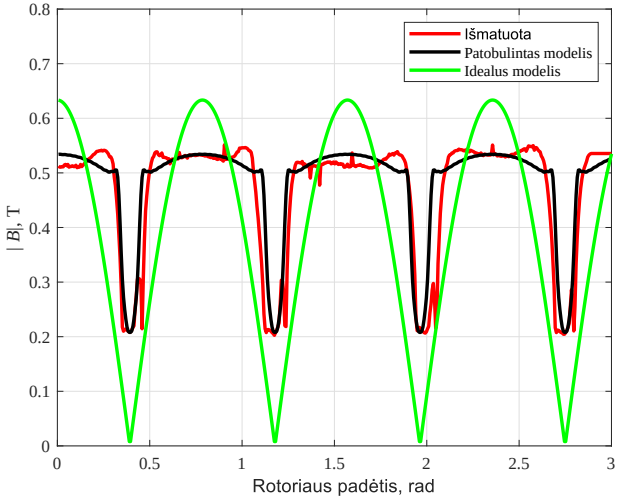

S3.6 pav. Sumodeliuoto ir išmatuoto magnetinio srauto tankio absoliučiosios vertės palyginimas

Magnetinio srauto tankio matavimai ir skaičiavimo rezultatai, naudojant sukurtą patobulintą SVNM modelį pateikti viename grafike (S3.6 pav.). Atliekant patobulinto SVNM

modelio modeliavimą buvo padaryta prielaida, kad nuolatiniai rotoriaus magnetai yra įmagnetinti lygiagrečiai, o magnetinio srauto tankis matuojamas oro tarpe, prie pat statoriaus korpuso. Iš S3.6 pav. pateiktų kreivių galime daryti išvadą, kad eksperimentiškai išmatuotas magnetinis srauto tankis tiek skaitmeninėmis vertėmis, tiek savo forma yra artimas patobulinto SVNM modelio modeliavimo rezultatams. Bendras integralinis patobulinto SVNM modelio magnetinio srauto tankio kreivės sutapimas su fiziškai išmatuotu magnetinio srauto tankiu sudaro 97 % (t. y. skiriasi 3 %), o tai patvirtina gerą pasiūlyto SVNM modelio patikimumą. Tame pačiame grafike taip pat atidėtas ir magnetinio srauto tankis apskaičiuotas naudojant idealų SVNM matematinį modelį. Toks matematinis SVNM modelis yra idealus. Tokio idealaus SVNM modelio magnetinis srauto tankis yra tobulo sinuso formos, o jo absoliučiosios vertės laikinė priklausomybė parodyta žalia kreive S3.6 pav. Palyginus patobulinto SVNM modelio rezultatus su idealiu SVNM modeliu matomas didelis skirtumas. Kiekybinis magnetinio srauto tankio absoliučiosios vertės skirtumas tarp patobulinto SVNM modelio ir idealaus SVNM modelio sudaro 20 %. Todėl galima teigti, kad pasiūlytas patobulintas SVNM modelis yra tikslesnis lyginant su plačiai naudojamu idealiu modeliu.

Bendrosios išvados

1. Sukurtas sinchroninio variklio su nuolatiniais magnetais variklio matematinis modelis pagrįstas analitinėmis magnetinio srauto tankio išraiškomis leidžia įvertinti sukimo momento pulsacijas, statoriaus induktyvumo pasiskirstymą ir elektrovaros formą.
2. Pasiūlyta išplėstinio Kalmano filtro, skirto variklio rotoriaus padėčiai nustatyi, algoritmo modifikacija leidžia skaičiavimo laiką sutrumpinti 3 kartus, atskiriant variacijos matricų skaičiavimą nuo viso algoritmo ir jas skaičiuojant lėtesniu dažniu.
3. Sinchroninio variklio su nuolatiniais magnetais statoriaus varžą ir induktyvumą galima nustatyti, esant rotoriui ramybės būsenos, naudojant tris 20 μs įtampos impulsus, matuojant fazines statoriaus sroves.
4. Sukurtos magnetinio srauto tankio matavimo sistemos leidžia matuoti lauką mažame sinchroninio variklio su nuolatiniais magnetais oro tarpe, esant nežinomai magnetinio srauto krypčiai.

Annex A. Analytical Calculation Equations of Magnetic Field Distribution

The Magnetic Field Density Distribution in Permanent Magnet Motors Equipped with the Surface-Mounted Magnets

In the air gap, the radial and tangential components are expressed as

$$\begin{aligned} B_{\mathrm{r}}^{\mathrm{a}} &= \sum_{n=1,3,5,\ldots}^{\infty} K_{\mathrm{B}}(n) \mathrm{f}_{\mathrm{Br}}(r) \cos(np\theta), \\ B_{\theta}^{\mathrm{a}} &= \sum_{n=1,3,5,\ldots}^{\infty} K_{\mathrm{B}}(n) \mathrm{f}_{\mathrm{B}\theta}(r) \sin(np\theta), \end{aligned} \tag{A. 1}$$

where, for internal motor when $np \neq 1$

$$\begin{aligned} K_{\mathrm{B}}(n) = \frac{\mu_0 M_{\mathrm{n}}}{\mu_{\mathrm{r}}} \frac{np}{(np)^2 - 1} \cdot \\ \cdot \left\{ \frac{(A_{3n} - 1) + 2\left(\frac{R_{\mathrm{r}}}{R_{\mathrm{m}}}\right)^{np+1} - (A_{3n} + 1)\left(\frac{R_{\mathrm{r}}}{R_{\mathrm{m}}}\right)^{2np}}{\frac{\mu_{\mathrm{r}}+1}{\mu_{\mathrm{r}}}\left[1 - \left(\frac{R_{\mathrm{r}}}{R_{\mathrm{s}}}\right)^{2np}\right] - \frac{\mu_{\mathrm{r}}-1}{\mu_{\mathrm{r}}}\left[\left(\frac{R_{\mathrm{m}}}{R_{\mathrm{s}}}\right)^{2np} - \left(\frac{R_{\mathrm{r}}}{R_{\mathrm{m}}}\right)^{2np}\right]} \right\}, \end{aligned} \tag{A. 2}$$

$$\begin{aligned} \mathrm{f_{Br}}(r) &= \left(\frac{r}{R_\mathrm{s}}\right)^{np-1}\left(\frac{R_\mathrm{m}}{R_\mathrm{s}}\right)^{np+1}+\left(\frac{R_\mathrm{m}}{r}\right)^{np+1}, \\ \mathrm{f_{B\theta}}(r) &= -\left(\frac{r}{R_\mathrm{s}}\right)^{np-1}\left(\frac{R_\mathrm{m}}{R_\mathrm{s}}\right)^{np+1}+\left(\frac{R_\mathrm{m}}{r}\right)^{np+1}. \end{aligned} \tag{A. 3}$$

The magnetic field distribution in the magnets for the radial and tangential components is given

$$\begin{aligned} B_\mathrm{r}^\mathrm{m} = &\sum_{n=1,3,5,\ldots}^{\infty}\frac{\mu_0 M_\mathrm{n}}{\mu_\mathrm{r}}\frac{np}{(np)^2-1}\cdot \\ &\cdot\left\{\left[\frac{\left(A_{3n}-\frac{1}{\mu_\mathrm{r}}\right)\left(\frac{R_\mathrm{m}}{R_\mathrm{s}}\right)^{2np}+\left(1+\frac{1}{\mu_\mathrm{r}}\right)\left(\frac{R_\mathrm{r}}{R_\mathrm{m}}\right)^{np+1}\left(\frac{R_\mathrm{m}}{R_\mathrm{s}}\right)^{2np}-}{\frac{\mu_\mathrm{r}+1}{\mu_\mathrm{r}}\left[1-\left(\frac{R_\mathrm{r}}{R_\mathrm{s}}\right)^{2np}\right]-\frac{\mu_\mathrm{r}-1}{\mu_\mathrm{r}}\left[\left(\frac{R_\mathrm{m}}{R_\mathrm{s}}\right)^{2np}-\left(\frac{R_\mathrm{r}}{R_\mathrm{m}}\right)^{2np}\right]}\right.\right. \\ &\left.\left.\frac{-\left(A_{3n}+\frac{1}{\mu_\mathrm{r}}\right)-\left(1-\frac{1}{\mu_\mathrm{r}}\right)\left(\frac{R_\mathrm{r}}{R_\mathrm{m}}\right)^{np+1}}{}\right]\cdot\right. \\ &\left.\cdot\left[\left(\frac{r}{R_\mathrm{m}}\right)^{np-1}+\left(\frac{R_\mathrm{r}}{R_\mathrm{m}}\right)^{np-1}\left(\frac{R_\mathrm{r}}{r}\right)^{np+1}\right]+\left(\frac{R_\mathrm{r}}{r}\right)^{np+1}+A_{3n}\right\}\cos(np\theta), \end{aligned} \tag{A. 4}$$

$$\begin{aligned} B_\theta^\mathrm{m} = &-\sum_{n=1,3,5,\ldots}^{\infty}\frac{\mu_0 M_\mathrm{n}}{\mu_\mathrm{r}}\frac{np}{(np)^2-1}\cdot \\ &\cdot\left\{\left[\frac{\left(A_{3n}-\frac{1}{\mu_\mathrm{r}}\right)\left(\frac{R_\mathrm{m}}{R_\mathrm{s}}\right)^{2np}+\left(1+\frac{1}{\mu_\mathrm{r}}\right)\left(\frac{R_\mathrm{r}}{R_\mathrm{m}}\right)^{np+1}\left(\frac{R_\mathrm{m}}{R_\mathrm{s}}\right)^{2np}-}{\frac{\mu_\mathrm{r}+1}{\mu_\mathrm{r}}\left[1-\left(\frac{R_\mathrm{r}}{R_\mathrm{s}}\right)^{2np}\right]-\frac{\mu_\mathrm{r}-1}{\mu_\mathrm{r}}\left[\left(\frac{R_\mathrm{m}}{R_\mathrm{s}}\right)^{2np}-\left(\frac{R_\mathrm{r}}{R_\mathrm{m}}\right)^{2np}\right]}\right.\right. \\ &\left.\left.\frac{-\left(A_{3n}+\frac{1}{\mu_\mathrm{r}}\right)-\left(1-\frac{1}{\mu_\mathrm{r}}\right)\left(\frac{R_\mathrm{r}}{R_\mathrm{m}}\right)^{np+1}}{}\right]\cdot\right. \\ &\left.\cdot\left[\left(\frac{r}{R_\mathrm{m}}\right)^{np-1}-\left(\frac{R_\mathrm{r}}{R_\mathrm{m}}\right)^{np-1}\left(\frac{R_\mathrm{r}}{r}\right)^{np+1}\right]+\left(\frac{R_\mathrm{r}}{r}\right)^{np+1}-\frac{A_{3n}}{np}\right\}\sin(np\theta), \end{aligned} \tag{A. 5}$$

The induced back-EMF waveform can be calculated from a knowledge of the open-circuit magnetic field distribution and the stator winding distribution

$$e = -\frac{\lambda}{\mathrm{d}t} = \tilde{\Lambda}_0 \sum_{n=1,3,5,\ldots}^{\infty} 2N_\mathrm{s}B_\mathrm{n}R_\mathrm{s}Lw_\mathrm{r}K_\mathrm{dn}\sin(np\alpha), \tag{A. 6}$$

where winding distribution factor are

$$K_{dn} = \sin(np\alpha_{\mathrm{y}}/2), \tag{A. 7}$$

and α_{y} is winding pitch factor.

Open-circuit Magnetic Field Distribution with the Inset Permanent Magnets

The air gap magnetic flux distribution in the slotless permanent magnet synchronous motor with the surface inset permanent magnets can be obtained by

$$\begin{aligned} B_{\mathrm{r}} &= -\mu_0 \sum_{v=1,3,\ldots}^{N_{\mathrm{h}}} vp\hat{\mathbf{a}}^a_{\frac{v+1}{2}} \left[\left(\frac{r}{R_{\mathrm{s}}}\right)^{vp-1} \left(\frac{R_{\mathrm{m}}}{R_{\mathrm{s}}}\right)^{vp+1} + \left(\frac{R_{\mathrm{m}}}{r}\right)^{vp+1} \right] \cos(vp\theta), \\ B_{\theta} &= \mu_0 \sum_{v=1,3,\ldots}^{N_{\mathrm{h}}} vp\hat{\mathbf{a}}^a_{\frac{v+1}{2}} \left[\left(\frac{r}{R_{\mathrm{s}}}\right)^{vp-1} \left(\frac{R_{\mathrm{m}}}{R_{\mathrm{s}}}\right)^{vp+1} - \left(\frac{R_{\mathrm{m}}}{r}\right)^{vp+1} \right] \sin(vp\theta), \end{aligned} \tag{A. 8}$$

where the Fourier series coefficients can be obtained by solving linear equation

$$\begin{bmatrix} \mathbf{C} & \mathbf{D} \\ \mathbf{E} & \mathbf{F} \end{bmatrix} \begin{bmatrix} \hat{\mathbf{a}}^{\mathrm{a}} \\ \hat{\mathbf{a}}^{\mathrm{m}} \end{bmatrix} = \begin{bmatrix} \mathbf{g} \\ \mathbf{h} \end{bmatrix}, \tag{A. 9}$$

where the matrices $\mathbf{C}, \mathbf{D}, \mathbf{E}, \mathbf{F} \in \mathrm{Re}^{\frac{N_{\mathrm{h}}+1}{2} \times \frac{N_{\mathrm{h}}+1}{2}}$ and the matrices $\mathbf{a}^{\mathrm{a}}, \mathbf{a}^{\mathrm{m}}, \mathbf{g}, \mathbf{h} \in \mathrm{Re}^{\frac{N_{\mathrm{h}}+1}{2} \times 1}$. Naming matrix $\mathbf{A} = \begin{bmatrix} \mathbf{C} & \mathbf{D} \\ \mathbf{E} & \mathbf{F} \end{bmatrix}$, $\mathbf{x} = \begin{bmatrix} \hat{\mathbf{a}}^{\mathrm{a}} \\ \hat{\mathbf{a}}^{\mathrm{m}} \end{bmatrix}$ and $\mathbf{b} = \begin{bmatrix} \mathbf{g} \\ \mathbf{h} \end{bmatrix}$ the equation can be solved numerically $\mathbf{x} = \mathbf{A}^{-1}\mathbf{b}$. Each matrix can be obtained by

$$C_{ii} = vp \left[\left(\frac{R_{\mathrm{m}}}{R_{\mathrm{s}}}\right)^{2vp} - 1 \right], \tag{A. 10}$$

$$D_{ij} = np \left[\left(\frac{R_{\mathrm{r}}}{R_{\mathrm{m}}}\right)^{\frac{2np}{\alpha_{\mathrm{r}}}} - 1 \right] (S^-_{vn} - S^+_{vn}), \tag{A. 11}$$

$$E_{ji} = vp \left[\left(\frac{R_{\mathrm{m}}}{R_{\mathrm{s}}}\right)^{2vp} + 1 \right] (S^-_{vn} + S^+_{vn}), \tag{A. 12}$$

$$F_{jj} = -\mu_{\mathrm{r}} \frac{np}{\alpha_{\mathrm{r}}} \left[\left(\frac{R_{\mathrm{r}}}{R_{\mathrm{m}}}\right)^{\frac{2np}{\alpha_{\mathrm{r}}}} + 1 \right], \tag{A. 13}$$

$$g_i = \sum_{n=1,3,\ldots}^{N_{\mathrm{h}}} np \left[k_n|_{r=R_{\mathrm{m}}} - k_n|_{r=R_{\mathrm{r}}} \left(\frac{R_{\mathrm{r}}}{R_{\mathrm{m}}}\right)^{\frac{np}{\alpha_{\mathrm{r}}}+1} \right] (S^-_{vn} - S^+_{vn}), \tag{A. 14}$$

$$h_j = \mu_r \left[\frac{np}{\alpha_r} \, k_n|_{r=R_r} \left(\frac{R_r}{R_m} \right)^{\frac{np}{\alpha_r}+1} + k_n|_{r=R_m} + R_m \frac{\partial k_n}{\partial r}\bigg|_{r=R_m} - \frac{M_{rn}}{\mu_r} \right], \quad \text{(A. 15)}$$

where for case then $np \neq \alpha_r$

$$\begin{aligned} k_n &= \frac{M_{rn} + \frac{np}{\alpha_r} M_{\theta n}}{\mu_r \left[1 - \left(\frac{np}{\alpha_r} \right)^2 \right]}, \\ \frac{\partial k_n}{\partial r} &= 0, \end{aligned} \quad \text{(A. 16)}$$

The Fourier coefficients for three different magnetization patterns (radial, parallel, Halbach) for case then $np \neq \alpha_r$ are expressed as for the radial magnetization

$$\begin{aligned} M_{rn} &= \frac{4B_{rem}}{\mu_0 n\pi} sin\left(\frac{n\pi\alpha_p}{2\alpha_r} \right), \\ M_{\theta n} &= 0, \end{aligned} \quad \text{(A. 17)}$$

for the parallel magnetization

$$\begin{aligned} M_{rn} &= \frac{B_r}{\mu_0} \frac{\alpha_p}{\alpha_r} \left(\frac{sin[(np+\alpha_r)\frac{\pi\alpha_p}{2p\alpha_r}]}{(np+\alpha_r)\frac{\pi\alpha_p}{2p\alpha_r}} + \frac{sin[(np-\alpha_r)\frac{\pi\alpha_p}{2p\alpha_r}]}{(np-\alpha_r)\frac{\pi\alpha_p}{2p\alpha_r}} \right), \\ M_{\theta n} &= \frac{B_r}{\mu_0} \frac{\alpha_p}{\alpha_r} \left(\frac{sin[(np+\alpha_r)\frac{\pi\alpha_p}{2p\alpha_r}]}{(np+\alpha_r)\frac{\pi\alpha_p}{2p\alpha_r}} - \frac{sin[(np-\alpha_r)\frac{\pi\alpha_p}{2p\alpha_r}]}{(np-\alpha_r)\frac{\pi\alpha_p}{2p\alpha_r}} \right), \end{aligned} \quad \text{(A. 18)}$$

and for Halbach magnetization in case then the motor rotor is internal

$$\begin{aligned} M_{rn} &= -\frac{4B_r}{\mu_0 \pi} \frac{\alpha_p}{\alpha_r} \frac{\cos\left(\frac{np\alpha_p}{2\alpha_r} \right)}{\left(\frac{n\alpha_p}{\alpha_r} \right)^2 - 1}, \\ M_{\theta n} &= -M_{rn} \frac{n\alpha_p}{\alpha_r}. \end{aligned} \quad \text{(A. 19)}$$

Armature Reaction Field Produced by the Three-phase Stator Windings Accounting Winding Thickness

Where the component of vector magnetic potential A_z in winding for the internal structure motor is

$$A_z^w(r,\theta) = \sum_{n=1,2,\ldots}^{N_h} \frac{\mu_0 J_n R_c^2}{np[(np)^2-4]} \left\{ \frac{\left\{ -\frac{np+2}{2} + \frac{np-2}{2}\left(\frac{R_c}{R_r}\right)^{2np} + 2\left(\frac{R_s}{R_r}\right)^{np+2}\left(\frac{R_s}{R_c}\right)^{-np+2} \right\}}{1-\left(\frac{R_s}{R_r}\right)^{2np}} \left(\frac{r}{R_r}\right)^{np} + \right.$$
$$+ \frac{\left\{ -\frac{np+2}{2}\left(\frac{R_s}{R_c}\right)^{2np} + \frac{np-2}{2}\left(\frac{R_s}{R_r}\right)^{2np} + 2\left(\frac{R_s}{R_c}\right)^{np+2} \right\}}{1-\left(\frac{R_s}{R_r}\right)^{2np}} \left(\frac{R_c}{r}\right)^{np} +$$
$$\left. + np\left(\frac{r}{R_c}\right)^2 \right\} \sin(np\theta), \tag{A. 20}$$

and A_z component in the air gap region region is

$$A_z^a(r,\theta) = \sum_{n=1,2,\ldots}^{N_h} \frac{\mu_0 J_n R_c^2}{np[(np)^2-4]} \frac{\left\{ -\frac{np+2}{2}\left(\frac{R_s}{R_c}\right)^{2np} + 2\left(\frac{R_s}{R_c}\right)^{np+2} + \frac{np-2}{2} \right\}}{1-\left(\frac{R_s}{R_r}\right)^{2np}} \tag{A. 21}$$
$$\cdot \left[\left(\frac{R_c}{R_r}\right)^{np}\left(\frac{r}{R_r}\right)^{np} + \left(\frac{R_c}{r}\right)^{np} \right] \sin(np\theta).$$

Then the flux density components are deduced from A_z by

$$B_r = \frac{1}{r}\frac{\partial A_z}{\partial \theta}, B_\theta \quad = -\frac{\partial A_z}{\partial r}. \tag{A. 22}$$

The radial magnetic flux density component in the air gap region for the internal motor structure is

$$B_r^a(r,\theta) = \sum_{n=1,2,\ldots}^{N_h} \frac{\mu_0 J_n R_c}{[(np)^2-4]} \frac{\left\{ -\frac{np+2}{2}\left(\frac{R_s}{R_c}\right)^{2np} + 2\left(\frac{R_s}{R_c}\right)^{np+2} + \frac{np-2}{2} \right\}}{1-\left(\frac{R_s}{R_r}\right)^{2np}} \tag{A. 23}$$
$$\cdot \left[\left(\frac{R_c}{R_r}\right)^{np+1}\left(\frac{r}{R_r}\right)^{np-1} + \left(\frac{R_c}{r}\right)^{np+1} \right] \cos(np\theta),$$

and the tangential component in the air gap is

$$B_{\theta}^{\mathrm{a}}(r,\theta) = -\sum_{n=1,2,\ldots}^{N_{\mathrm{h}}} \frac{\mu_0 J_{\mathrm{n}} R_{\mathrm{c}}}{[(np)^2-4]} \frac{\left\{-\frac{np+2}{2}\left(\frac{R_{\mathrm{s}}}{R_{\mathrm{c}}}\right)^{2np} + 2\left(\frac{R_{\mathrm{s}}}{R_{\mathrm{c}}}\right)^{np+2} + \frac{np-2}{2}\right\}}{1-\left(\frac{R_{\mathrm{s}}}{R_{\mathrm{r}}}\right)^{2np}} \cdot \left[\left(\frac{R_{\mathrm{c}}}{R_{\mathrm{r}}}\right)^{np+1}\left(\frac{r}{R_{\mathrm{r}}}\right)^{np-1} - \left(\frac{R_{\mathrm{c}}}{r}\right)^{np+1}\right]\sin(np\theta). \tag{A. 24}$$

The radial magnetic flux density component in the winding region for the internal motor structure is

$$\begin{aligned} B_{\mathrm{r}}^{\mathrm{w}}(r,\theta) = & \sum_{n=1,2,\ldots}^{N_{\mathrm{h}}} \frac{\mu_0 J_{\mathrm{n}} R_{\mathrm{c}}}{[(np)^2-4]} \\ & \left\{ \frac{\left\{-\frac{np+2}{2} + \frac{np-2}{2}\left(\frac{R_{\mathrm{c}}}{R_{\mathrm{r}}}\right)^{2np} + 2\left(\frac{R_{\mathrm{s}}}{R_{\mathrm{r}}}\right)^{np+2}\left(\frac{R_{\mathrm{s}}}{R_{\mathrm{c}}}\right)^{-np+2}\right\}}{1-\left(\frac{R_{\mathrm{s}}}{R_{\mathrm{r}}}\right)^{2np}} + \right. \\ & + \frac{\left\{-\frac{np+2}{2}\left(\frac{R_{\mathrm{s}}}{R_{\mathrm{c}}}\right)^{2np} + \frac{np-2}{2}\left(\frac{R_{\mathrm{s}}}{R_{\mathrm{r}}}\right)^{2np} + 2\left(\frac{R_{\mathrm{s}}}{R_{\mathrm{c}}}\right)^{np+2}\right\}}{1-\left(\frac{R_{\mathrm{s}}}{R_{\mathrm{r}}}\right)^{2np}}\left(\frac{R_{\mathrm{c}}}{r}\right)^{np} + \\ & \left. + np\left(\frac{r}{R_{\mathrm{c}}}\right)^{2}\right\}\cos(np\theta), \end{aligned} \tag{A. 25}$$

and the tangential component in windings is

$$\begin{aligned} B_{\theta}^{\mathrm{w}}(r,\theta) = & -\sum_{n=1,2,\ldots}^{N_{\mathrm{h}}} \frac{\mu_0 J_{\mathrm{n}} R_{\mathrm{c}}}{[(np)^2-4]} \\ & \left\{ \frac{\left\{-\frac{np+2}{2} + \frac{np-2}{2}\left(\frac{R_{\mathrm{c}}}{R_{\mathrm{r}}}\right)^{2np} + 2\left(\frac{R_{\mathrm{s}}}{R_{\mathrm{r}}}\right)^{np+2}\left(\frac{R_{\mathrm{s}}}{R_{\mathrm{c}}}\right)^{-np+2}\right\}}{1-\left(\frac{R_{\mathrm{s}}}{R_{\mathrm{r}}}\right)^{2np}}\left(\frac{r}{R_{\mathrm{r}}}\right)^{np-1} - \right. \\ & \left. - \frac{\left\{-\frac{np+2}{2}\left(\frac{R_{\mathrm{s}}}{R_{\mathrm{c}}}\right)^{2np} + \frac{np-2}{2}\left(\frac{R_{\mathrm{s}}}{R_{\mathrm{r}}}\right)^{2np} + 2\left(\frac{R_{\mathrm{s}}}{R_{\mathrm{c}}}\right)^{np+2}\right\}}{1-\left(\frac{R_{\mathrm{s}}}{R_{\mathrm{r}}}\right)^{2np}}\left(\frac{R_{\mathrm{c}}}{r}\right)^{np+1} + \frac{2r}{R_{\mathrm{c}}}\right\} \cdot \\ & \cdot \sin(np\theta). \end{aligned} \tag{A. 26}$$

Armature Reaction Magnetic Field for Slotless Brushless Machines with the Inset Permanent Magnets

The radial and tangential components in case then $np \neq 2$ of the magnetic flux density in the air gap can be found as

$$\begin{aligned} B_{\mathrm{r}}^{\mathrm{a}} = \sum_{n=1}^{N_{\mathrm{h}}} np \Bigg\{ b_{\mathrm{n}}^{w} \Bigg[\left(\frac{R_{\mathrm{m}}}{R_{\mathrm{s}}}\right)^{np+1} \left(\frac{r}{R_{\mathrm{s}}}\right)^{np-1} + \left(\frac{R_{\mathrm{m}}}{r}\right)^{np+1} \Bigg] - \\ -\zeta_{n1}^{s} \left(\frac{r}{R_{\mathrm{s}}}\right)^{np-1} + \frac{\zeta_{n2}^{s} + \zeta_{n3}^{s}}{2} \left(\frac{r}{R_{\mathrm{a}}}\right)^{np-1} + \frac{\zeta_{n2}^{s} - \zeta_{n3}^{s}}{2} \left(\frac{R_{\mathrm{a}}}{r}\right)^{np+1} \Bigg\} \cdot \\ \cdot \cos(np\theta) - np \Bigg\{ d_{n}^{\mathrm{w}} \Bigg[\left(\frac{R_{\mathrm{m}}}{R_{\mathrm{s}}}\right)^{np+1} \left(\frac{r}{R_{\mathrm{s}}}\right)^{np-1} + \left(\frac{R_{\mathrm{m}}}{r}\right)^{np+1} \Bigg] - \\ -\zeta_{n1}^{c} \left(\frac{r}{R_{\mathrm{s}}}\right)^{np-1} + \frac{\zeta_{n2}^{c} + \zeta_{n3}^{c}}{2} \left(\frac{r}{R_{\mathrm{a}}}\right)^{np-1} + \frac{\zeta_{n2}^{c} - \zeta_{n3}^{c}}{2} \left(\frac{R_{\mathrm{a}}}{r}\right)^{np+1} \Bigg\} \cdot \\ \cdot \sin(np\theta), \end{aligned} \tag{A. 27}$$

$$\begin{aligned} B_{\theta}^{\mathrm{a}} = \sum_{n=1}^{N_{\mathrm{h}}} -np \Bigg\{ b_{\mathrm{n}}^{w} \Bigg[\left(\frac{R_{\mathrm{m}}}{R_{\mathrm{s}}}\right)^{np+1} \left(\frac{r}{R_{\mathrm{s}}}\right)^{np-1} - \left(\frac{R_{\mathrm{m}}}{r}\right)^{np+1} \Bigg] - \\ -\zeta_{n1}^{s} \left(\frac{r}{R_{\mathrm{s}}}\right)^{np-1} + \frac{\zeta_{n2}^{s} + \zeta_{n3}^{s}}{2} \left(\frac{r}{R_{\mathrm{a}}}\right)^{np-1} - \frac{\zeta_{n2}^{s} - \zeta_{n3}^{s}}{2} \left(\frac{R_{\mathrm{a}}}{r}\right)^{np+1} \Bigg\} \cdot \\ \cdot \sin(np\theta) + np \Bigg\{ d_{n}^{\mathrm{w}} \Bigg[\left(\frac{R_{\mathrm{m}}}{R_{\mathrm{s}}}\right)^{np+1} \left(\frac{r}{R_{\mathrm{s}}}\right)^{np-1} - \left(\frac{R_{\mathrm{m}}}{r}\right)^{np+1} \Bigg] - \\ -\zeta_{n1}^{c} \left(\frac{r}{R_{\mathrm{s}}}\right)^{np-1} + \frac{\zeta_{n2}^{c} + \zeta_{n3}^{c}}{2} \left(\frac{r}{R_{\mathrm{a}}}\right)^{np-1} - \frac{\zeta_{n2}^{c} - \zeta_{n3}^{c}}{2} \left(\frac{R_{\mathrm{a}}}{r}\right)^{np+1} \Bigg\} \cdot \\ \cdot \cos(np\theta). \end{aligned} \tag{A. 28}$$

where b_{n}^{w}, d_{n}^{w} are coefficients. For the case then $np \neq 2$

$$\zeta_{n1}^{\mathrm{s}} = \frac{R_{\mathrm{s}} \mu_0 J_{\mathrm{n}}^{s}}{np} \frac{2}{(np)^2 - 4}, \tag{A. 29}$$

$$\zeta_{n1}^{\mathrm{c}} = \frac{R_{\mathrm{s}} \mu_0 J_{\mathrm{n}}^{c}}{np} \frac{2}{(np)^2 - 4}, \tag{A. 30}$$

$$\zeta_{n2}^{\mathrm{s}} = \frac{R_{\mathrm{a}} \mu_0 J_{\mathrm{n}}^{s}}{(np)^2 - 4}, \tag{A. 31}$$

$$\zeta_{n2}^{c} = \frac{R_{\mathrm{a}} \mu_0 J_{\mathrm{n}}^{c}}{(np)^2 - 4}, \tag{A. 32}$$

$$\zeta_{n3}^{\mathrm{s}} = \frac{R_{\mathrm{a}}\mu_0 J_{\mathrm{n}}^{s}}{np}\frac{2}{(np)^2-4}, \tag{A. 33}$$

$$\zeta_{n3}^{\mathrm{c}} = \frac{R_{\mathrm{a}}\mu_0 J_{\mathrm{n}}^{c}}{np}\frac{2}{(np)^2-4}, \tag{A. 34}$$

and

$$\begin{aligned} k_n^{\mathrm{s}} &= \frac{\mu_0 J_{\mathrm{n}}^{\mathrm{s}}}{(np)^2-4}, \\ k_n^{\mathrm{c}} &= \frac{\mu_0 J_{\mathrm{n}}^{\mathrm{c}}}{(np)^2-4}, \end{aligned} \tag{A. 35}$$

where the current density components J_{n} as a product of three phases currents $i_{\mathrm{j}} = i_{\mathrm{a}}, i_{\mathrm{b}}, i_{\mathrm{c}}$ are

$$\begin{aligned} J_{\mathrm{n}}^{\mathrm{s}} &= \sum_{j=1}^{3}\frac{4pN_{\mathrm{s}}}{|R_{\mathrm{s}}^2 - R_{\mathrm{a}}^2|}\sin\left(n\frac{\theta_{\mathrm{c}}}{2}\right)\frac{\sin\left(n\frac{\lambda_{\mathrm{c}}}{2}\right)}{n\frac{\lambda_{\mathrm{c}}}{2}} i_j(t)\cos\left(n\frac{2\pi(j-1)}{3}\right), \\ J_{\mathrm{n}}^{\mathrm{c}} &= -\sum_{j=1}^{3}\frac{4pN_{\mathrm{s}}}{|R_{\mathrm{s}}^2 - R_{\mathrm{a}}^2|}\sin\left(n\frac{\theta_{\mathrm{c}}}{2}\right)\frac{\sin\left(n\frac{\lambda_{\mathrm{c}}}{2}\right)}{n\frac{\lambda_{\mathrm{c}}}{2}} i_j(t)\sin\left(n\frac{2\pi(j-1)}{3}\right). \end{aligned} \tag{A. 36}$$

The Fourier series coefficients $b_{\mathrm{n}}^{\mathrm{w}}$, d_n^{w} can be obtained by solving linear equation

$$\begin{bmatrix} \mathbf{\Lambda}^{11} & \mathbf{0} & \mathbf{\Lambda}^{13} & \mathbf{\Lambda}^{14} \\ \mathbf{0} & \mathbf{\Lambda}^{22} & \mathbf{\Lambda}^{23} & \mathbf{\Lambda}^{24} \\ \mathbf{\Lambda}^{31} & \mathbf{\Lambda}^{32} & \mathbf{\Lambda}^{33} & \mathbf{0} \\ \mathbf{\Lambda}^{41} & \mathbf{\Lambda}^{42} & \mathbf{0} & \mathbf{\Lambda}^{44} \end{bmatrix} \begin{bmatrix} \mathbf{b}^{\mathrm{w}} \\ \mathbf{d}^{\mathrm{w}} \\ \mathbf{a}^{\mathrm{m,0}} \\ \mathbf{a}^{\mathrm{m,l}} \end{bmatrix} = \begin{bmatrix} \mathbf{\Gamma}^1 \\ \mathbf{\Gamma}^2 \\ \mathbf{\Gamma}^3 \\ \mathbf{\Gamma}^4 \end{bmatrix}, \tag{A. 37}$$

the matrices $\mathbf{\Lambda}^{xy} \in \mathrm{Re}^{N_{\mathrm{h}}\times N_{\mathrm{h}}}$, $\mathbf{b}^{w} \in \mathrm{Re}^{N_{\mathrm{h}}\times 1}$ $\mathbf{d}^{\mathrm{w}} \in \mathrm{Re}^{N_{\mathrm{h}}\times 1}$, $\mathbf{a}^{\mathrm{m,0}} \in \mathrm{Re}^{N_{\mathrm{h}}\times 1}$, $\mathbf{a}^{\mathrm{m,l}} \in \mathrm{Re}^{N_{\mathrm{h}}\times 1}$ and $\mathbf{\Gamma}^{x} \in \mathrm{Re}^{N_{\mathrm{h}}\times 1}$.

Each matrix can be obtained by

$$\mathbf{\Gamma}_n^1 = 2n\left[\zeta_{n1}^{s}\left(\frac{R_{\mathrm{m}}}{R_{\mathrm{s}}}\right)^{np-1} - \frac{\zeta_{n2}^{s}+\zeta_{n3}^{s}}{2}\left(\frac{R_{\mathrm{m}}}{R_{\mathrm{a}}}\right)^{np-1} + \frac{\zeta_{n2}^{s}-\zeta_{n3}^{s}}{2}\left(\frac{R_{\mathrm{a}}}{R_{\mathrm{m}}}\right)^{np+1}\right], \tag{A. 38}$$

$$\mathbf{\Gamma}_n^2 = 2n\left[\zeta_{n1}^{c}\left(\frac{R_{\mathrm{m}}}{R_{\mathrm{s}}}\right)^{np-1} - \frac{\zeta_{n2}^{c}+\zeta_{n3}^{c}}{2}\left(\frac{R_{\mathrm{m}}}{R_{\mathrm{a}}}\right)^{np-1} + \frac{\zeta_{n2}^{c}-\zeta_{n3}^{c}}{2}\left(\frac{R_{\mathrm{a}}}{R_{\mathrm{m}}}\right)^{np+1}\right], \tag{A. 39}$$

$$\begin{aligned} \mathbf{\Gamma}_n^3 = \sum_{n=1}^{N_{\mathrm{h}}}\Bigg\{ n\Bigg[\zeta_{n1}^{s}\left(\frac{R_{\mathrm{m}}}{R_{\mathrm{s}}}\right)^{np-1} - \frac{\zeta_{n2}^{s}+\zeta_{n3}^{s}}{2}\left(\frac{R_{\mathrm{m}}}{R_{\mathrm{a}}}\right)^{np-1} - \frac{\zeta_{n2}^{s}-\zeta_{n3}^{s}}{2}\cdot \\ \cdot\left(\frac{R_{\mathrm{a}}}{R_{\mathrm{m}}}\right)^{np+1}\Bigg]\gamma_{\mathrm{c}}(n,v) - \Bigg[\zeta_{n1}^{c}\left(\frac{R_{\mathrm{m}}}{R_{\mathrm{s}}}\right)^{np-1} - \frac{\zeta_{n2}^{c}+\zeta_{n3}^{c}}{2}\left(\frac{R_{\mathrm{m}}}{R_{\mathrm{a}}}\right)^{np-1} - \\ -\frac{\zeta_{n2}^{c}-\zeta_{n3}^{c}}{2}\left(\frac{R_{\mathrm{a}}}{R_{\mathrm{m}}}\right)^{np+1}\Bigg]\gamma_{\mathrm{s}}(n,v)\Bigg\}, \end{aligned} \tag{A. 40}$$

$$\mathbf{\Gamma}_n^4 = \sum_{n=1}^{N_\mathrm{h}} \left\{ (-1)^n n \left[\zeta_{n1}^s \left(\frac{R_\mathrm{m}}{R_\mathrm{s}} \right)^{np-1} - \frac{\zeta_{n2}^s + \zeta_{n3}^s}{2} \left(\frac{R_\mathrm{m}}{R_\mathrm{a}} \right)^{np-1} - \frac{\zeta_{n2}^s - \zeta_{n3}^s}{2} \cdot \right.\right.$$
$$\left.\left. \cdot \left(\frac{R_\mathrm{a}}{R_\mathrm{m}} \right)^{np+1} \right] \gamma_\mathrm{c}(n,v) - \left[\zeta_{n1}^c \left(\frac{R_\mathrm{m}}{R_\mathrm{s}} \right)^{np-1} - \frac{\zeta_{n2}^c + \zeta_{n3}^c}{2} \left(\frac{R_\mathrm{m}}{R_\mathrm{a}} \right)^{np-1} - \right.$$
$$\left. - \frac{\zeta_{n2}^c - \zeta_{n3}^c}{2} \left(\frac{R_\mathrm{a}}{R_\mathrm{m}} \right)^{np+1} \right] \gamma_\mathrm{s}(n,v) \right\}, \tag{A. 41}$$

$$\mathbf{\Lambda}_{n,n}^{11} = \mathbf{\Lambda}_{n,n}^{22} = 2n \left[\left(\frac{R_\mathrm{m}}{R_\mathrm{s}} \right)^{2np} - 1 \right], \tag{A. 42}$$

$$\mathbf{\Lambda}_{n,v}^{13} = \frac{v}{\mu_\mathrm{r}\alpha_\mathrm{r}} \left[\left(\frac{R_\mathrm{r}}{R_\mathrm{m}} \right)^{\frac{2vp}{\alpha_\mathrm{r}}} - 1 \right] \varepsilon_\mathrm{s}(n,v), \tag{A. 43}$$

$$\mathbf{\Lambda}_{n,v}^{14} = (-1)^n \frac{v}{\mu_\mathrm{r}\alpha_\mathrm{r}} \left[\left(\frac{R_\mathrm{r}}{R_\mathrm{m}} \right)^{\frac{2vp}{\alpha_\mathrm{r}}} - 1 \right] \varepsilon_\mathrm{s}(n,v), \tag{A. 44}$$

$$\mathbf{\Lambda}_{n,v}^{23} = \frac{v}{\mu_\mathrm{r}\alpha_\mathrm{r}} \left[\left(\frac{R_\mathrm{r}}{R_\mathrm{m}} \right)^{\frac{2vp}{\alpha_\mathrm{r}}} - 1 \right] \varepsilon_c(n,v), \tag{A. 45}$$

$$\mathbf{\Lambda}_{n,v}^{24} = (-1)^n \frac{v}{\mu_\mathrm{r}\alpha_\mathrm{r}} \left[\left(\frac{R_\mathrm{r}}{R_\mathrm{m}} \right)^{\frac{2vp}{\alpha_\mathrm{r}}} - 1 \right] \varepsilon_c(n,v), \tag{A. 46}$$

$$\mathbf{\Lambda}_{v,n}^{31} = n \left[\left(\frac{R_\mathrm{m}}{R_\mathrm{s}} \right)^{2np} + 1 \right] \gamma_\mathrm{c}(n,v), \tag{A. 47}$$

$$\mathbf{\Lambda}_{v,n}^{32} = -n \left[\left(\frac{R_\mathrm{m}}{R_\mathrm{s}} \right)^{2np} + 1 \right] \gamma_\mathrm{s}(n,v), \tag{A. 48}$$

$$\mathbf{\Lambda}_{v,v}^{33} = \mathbf{\Lambda}_{v,v}^{44} = \frac{v}{\alpha_\mathrm{r}} \left[\left(\frac{R_\mathrm{r}}{R_\mathrm{m}} \right)^{\frac{2vp}{\alpha_\mathrm{r}}} + 1 \right], \tag{A. 49}$$

$$\mathbf{\Lambda}_{v,n}^{41} = (-1)^n n \left[\left(\frac{R_\mathrm{m}}{R_\mathrm{s}} \right)^{2np} + 1 \right] \gamma_\mathrm{s}(n,v), \tag{A. 50}$$

$$\mathbf{\Lambda}_{v,n}^{42} = (-1)^{n+1} n \left[\left(\frac{R_\mathrm{m}}{R_\mathrm{s}} \right)^{2np} + 1 \right] \gamma_\mathrm{c}(n,v), \tag{A. 51}$$

where unknown factors can be found by

$$\begin{aligned}
\varepsilon_{\mathrm{s}}(n,v) &= \frac{\alpha_{\mathrm{r}}}{\pi}\left\{\frac{-\cos\left(v\pi+n\frac{\pi\alpha_{\mathrm{r}}}{2}+np\alpha\right)+\cos\left(n\frac{\pi\alpha_{\mathrm{r}}}{2}-np\alpha\right)}{\alpha_{\mathrm{r}}n+v}-\right.\\
&\left.-\frac{\cos\left(v\pi-n\frac{\pi\alpha_{\mathrm{r}}}{2}-np\alpha\right)-\cos\left(n\frac{\pi\alpha_{\mathrm{r}}}{2}-np\alpha\right)}{\alpha_{\mathrm{r}}n-v}\right\},\\
\varepsilon_{c}(n,v) &= \frac{\alpha_{\mathrm{r}}}{\pi}\left\{\frac{\sin\left(v\pi+n\frac{\pi\alpha_{\mathrm{r}}}{2}+np\alpha\right)+\sin\left(n\frac{\pi\alpha_{\mathrm{r}}}{2}-np\alpha\right)}{\alpha_{\mathrm{r}}n+v}-\right.\\
&\left.-\frac{\sin\left(v\pi-n\frac{\pi\alpha_{\mathrm{r}}}{2}-np\alpha\right)-\sin\left(n\frac{\pi\alpha_{\mathrm{r}}}{2}-np\alpha\right)}{\alpha_{\mathrm{r}}n-v}\right\},
\end{aligned} \tag{A. 52}$$

and

$$\begin{aligned}
\gamma_{\mathrm{s}}(n,v) &= \frac{1}{\pi}\left\{\frac{-\sin\left(v\pi+n\frac{\pi\alpha_{\mathrm{r}}}{2}+np\alpha\right)-\sin\left(n\frac{\pi\alpha_{\mathrm{r}}}{2}-np\alpha\right)}{\alpha_{\mathrm{r}}n+v}-\right.\\
&\left.-\frac{\sin\left(v\pi-n\frac{\pi\alpha_{\mathrm{r}}}{2}-np\alpha\right)-\sin\left(n\frac{\pi\alpha_{\mathrm{r}}}{2}-np\alpha\right)}{\alpha_{\mathrm{r}}n-v}\right\},\\
\gamma_{\mathrm{c}}(n,v) &= \frac{1}{\pi}\left\{\frac{-\cos\left(v\pi+n\frac{\pi\alpha_{\mathrm{r}}}{2}+np\alpha\right)+\cos\left(n\frac{\pi\alpha_{\mathrm{r}}}{2}-np\alpha\right)}{\alpha_{\mathrm{r}}n+v}+\right.\\
&\left.+\frac{\cos\left(v\pi-n\frac{\pi\alpha_{\mathrm{r}}}{2}-np\alpha\right)-\cos\left(n\frac{\pi\alpha_{\mathrm{r}}}{2}-np\alpha\right)}{\alpha_{\mathrm{r}}n-v}\right\}.
\end{aligned} \tag{A. 53}$$

Justas DILYS

RESEARCH INTO VARIABILITY OF PERMANENT MAGNET SYNCHRONOUS MOTOR PARAMETERS BY MAGNETIC FIELD MODELLING

Doctoral Dissertation

Technological Sciences,
Electrical and Electronic Engineering (T 001)

SINCHRONINIO VARIKLIO SU NUOLATINIAIS MAGNETAIS PARAMETRŲ KITIMO TYRIMAS MODELIUOJANT MAGNETINĮ LAUKĄ

Daktaro disertacija

Technologijos mokslai,
elektros ir elektronikos inžinerija (T 001)

Lietuvių kalbos redaktorė Dalia Markevičiūtė
Anglų kalbos redaktorė Jūratė Griškėnaitė

2023 05 12. 12,5 sp. l. Tiražas 20 egz.
Leidinio el. versija *https://doi.org/10.20334/2023-023-M*
Vilniaus Gedimino technikos universitetas
Saulėtekio al. 11, 10223 Vilnius,
Spausdino UAB „Ciklonas“,
Žirmūnų g. 68, 09124 Vilnius